Computational Studies on Novel Atomic Force Microscopy Techniques and Plasmonic-Enhanced Organic Photovoltaics

Durmus Ugur Karatay

A dissertation

submitted in partial fulfillment of the

requirements for the degree of

Doctor of Philosophy

University of Washington

2015

Reading Committee:

David S. Ginger, Chair

Marcel den Nijs

Andreas Karch

Program Authorized to Offer Degree:

Physics

University of Washington

Abstract

Computational Studies on Novel Atomic Force Microscopy Techniques and Plasmon-Enhanced Organic Photovoltaics

Durmus Ugur Karatay

Chair of the Supervisory Committee:
David S. Ginger
Department of Chemistry

In physical and life sciences, employing computational approaches to understand the nature of studied materials and subjects and to analyze immense amount of data is increasingly becoming more popular. Using existing methods and techniques is surprisingly easy, however these are not always well-suited for the problem at hand. Developing new methods specific to a problem requires a deep understanding of the problem, the underlying physics and relevant computational methods.

Atomic Force Microscopy (AFM) is a unique tool for studying different properties of materials, such as conductivity, surface topography and forces. It also is a flexible tool for developing novel techniques that enable new studies in many fields of science. Although AFM is versatile, it can still be challenging to implement novel methods. Here, we describe in detail the

hardware and the software implementation of simultaneous data acquisition and analysis in fast time-resolved electrostatic force microscopy (trEFM). Fast trEFM can measure nanosecond-scale local dynamics using widely available AFM hardware. We computationally and experimentally investigate the limits of trEFM and show that we can discriminate signal rise times with time constants as fast as 10 ns.

Dynamic Force Spectroscopy is another method that is based on AFM and widely used in life sciences to measure mechanical properties of tissues, cells and DNA. We investigate computational methods to analyze force curves resulting from DNA pulling experiments in order to understand the unbinding kinetics of DNA under mechanical loading. We demonstrate that we can automate analysis of force curves using modern machine learning algorithms with an accuracy rate of 94%, which is approximately equal to human experimenters' scores.

Another area to which one can apply computational methods is modeling organic photovoltaic devices. Organic photovoltaics (OPVs) are one potential solution to growing demand for clean and inexpensive energy. Fabricating organic solar cells is a relatively easy process; the challenge is to make them as efficient as their inorganic counterparts. To increase the performance of an OPV device, one can use many different approaches, such as changing the device architecture or incorporating metal nanoparticles. Here, we study performance limits of plasmon-enhanced organic photovoltaics using a combination of computational modeling and experiment. We model modern low-bandgap donor polymer-fullerene blends with variety of colloidal silver nanoparticles to understand how sensitive the device performance is to nanoparticles. We show that it is possible to achieve an enhancement of 31% in short-circuit current density.

TABLE OF CONTENTS

LIST OF FIGURES

LIST OF TABLES

ACKNOWLEDGEMENTS

I would like to thank many people from my family to my friends, colleagues and professors. This dissertation could not have been done without their support and inspiration.

I thank my research advisor, David S. Ginger, for his advisement throughout this process. I appreciate his eagerness for discussion, scientific challenges and bets.

Many people contributed to this work. Dr. Micah Glaz and Dr. Raj Giridharagopal provided critical views on Chapter 2. Jeff Harrison helped me build the software for data acquisition. Special thanks to Jim Gladden and Bill Beaty for discussions on electronics and building trigger circuitry. In Chapter 3, Dr. Jie Zhang collected data and gave me insight about DNA pulling measurements. I am most grateful to Dr. Michael Salvador for sharing his wisdoms and experiences with me as well as preparing samples and acquiring experimental data for Chapter 4.

I would like to personally thank my friends: Isaac Backus, John Lee and Matthias Smith for fruitful discussions that took place late at night.

I also owe very much to Catherine Provost and Marcel den Nijs for being great advisors all along the way.

Part of the work done here is supported by the National Science Foundation (NSF MRI DMR-1337173), the Office of Naval Research (N00014-14-1-0170 and N00014-11-1-0300), the State of Washington through the University of Washington Clean Energy Institute, the Asian Office of Aerospace R&D (FA2386-11-1-4072), and the Air Force Office of Scientific Research (AFOSR FA9550-14-1-0250).

Chapter 1. Introduction

1.1 Motivation and Background

In the late 20th century, computational methods became an integral part of natural sciences; the use of novel algorithms and techniques for developing novel instruments and for analyzing and understanding experimental data has become increasingly ubiquitous. The application of computational techniques in physical and life sciences requires both a knowledge of available methods and an understanding of the nature of the problem. Then, one can choose an appropriate method to apply. Generally, these problems either require a specialized application of a well-known technique or development of novel techniques. There are many examples of well-known algorithms that were developed to solve a specific scientific problem which have since become staples of computer science, such as the Fast-Fourier Transform[1] or the Metropolis-Hastings algorithm for Monte Carlo methods.[2,3]

With increasing computing power, computational modeling and data analysis have undergone a substantial transformation in the last few decades and have become more accessible.[4,5] Increased use of computational modeling lets researchers model and evaluate their experiments, which results in less effort being spent on realizing their experiments, and more time understanding the results.

Nonetheless, the modeling of basic principles is not enough to understand the nature of processes happening inside materials. We do need experimental data to verify our theoretical and computational methods. Thus, we use instruments that give us a chance to look into the underlying physics. Most of the time, these instruments are developed because of a pressing need to access length and time scales that are currently inaccessible. For instance, nanometer scale materials could not be probed easily using optical microscopy tools, thereby pushing the development of scanning probe microscopy techniques, such as scanning probe microscopy in 1980s.[6,7]

Atomic force microscopy is an invaluable tool in material science for getting insight into different properties of materials, such as the electronic properties of semiconductors[8–18] and the unbinding behavior of double-stranded DNA.[19–22] There is a pressing need for the development of novel AFM methods, since conventional AFM methods do not capture information at length and time scales relevant to modern materials. Therefore, we can benefit from computational methods to develop new techniques by understanding the nature of interactions through modeling. Furthermore, many of these conventional and novel AFM techniques are slow to acquire data and the analysis of acquired data can be slow when done by hand. In order to mitigate these issues, we can use modern data analysis methods and machine learning algorithms. In this dissertation, I will focus on the use of computational modeling and data analysis of trEFM, which is an AFM technique that can measure fast local dynamics, as fast as 10 ns, in electrically active devices. Here, we focus on probing optoelectronic properties of nanostructured materials dynamically. Additionally, I will explore supervised and unsupervised machine learning algorithms to speed up the analysis of dynamic force spectroscopy of photoswitch-modified DNA.

Another area that we can apply computational modeling is in the analysis of organic electronic devices. Some benefits of using an organic material as the active layer in a device are the easiness chemical modification, inexpensive wet-bench processing and printing methods. Many organic electronic devices are currently in the market, such as active-matrix organic light emitting diodes (AMOLED)[23–25] and organic thin film transistors.[26–28] Organic photovoltaics (OPV) are another material, but have not achieved commercial viability yet, due to poorer efficiency and stability in comparison to their inorganic counterparts.[29] The state-of-the-art organic solar cells have power conversion efficiencies at the order of 7-8%[30] with the record devices achieving 11.5%,[31] whereas multicrystalline silicon solar cells have record efficiencies of 20.8%

Different optical engineering methods can be applied to increase device efficiencies without changing the chemistry of the device, such as incorporating plasmonic particles. In order to understand how the performance is affected after inclusion of metal nanoparticles, one has to fabricate and measure many devices. Nevertheless, we can leverage computational modeling to understand the different parameters and their effect on the device performance. Here, we will examine a model OPV device with metal nanoparticles to explore the limits of enhancement and lay down a set of guidelines for improving efficiencies of OPVs with metal nanoparticles. Now, let us examine basics of AFM operation, OPVs and plasmonics.

1.2 Brief History and Basics of AFM Operation

The groundwork for the invention of the AFM was laid by Binnig and Rohrer in 1982 at IBM Research – Zurich with the invention of scanning tunneling microscope (STM),[6] which earned them the Nobel Prize for Physics in 1986. STM uses tunneling electrons through a conducting material to a sharp tip, which creates a current that can be measured. This sharp tip hovers over the surface, thus enabling imaging of material surfaces at atomic scales. However, one of the main drawbacks of STM is that it can only image electrically conductive materials.

The AFM, invented in 1986 by Binnig, Quate and Gerber,[7] consists of a cantilever that holds a tip at its end. AFM overcomes the issue of only imaging conductive materials by bringing cantilever closer to the surface and measuring the forces between the surface and the tip, where these forces are generally from 1 pN to 1 nN and can have ranges of few angstroms to few microns. These forces are measured by measuring the deflection of the cantilever.

The cantilever deflection can be measured using a few different methods, such as using optical levers, capacitive detection, or piezoelectric detection. Among these, the most widely used and the most commercially available one is optical lever, where a solid state laser is positioned to the reflective back of the cantilever; and the reflected laser beam is collected by a four quadrant photodiode detector as shown in Figure 1.1. Output signals from the split photodiodes are collected by a differential amplifier, which takes the difference between signals and normalizes them by their sum. The resulting signal is proportional to the deflection of the cantilever and can be converted to the force using Hooke's law.

AFMs can be operated in few different modes: contact mode, non-contact mode, and tapping mode.

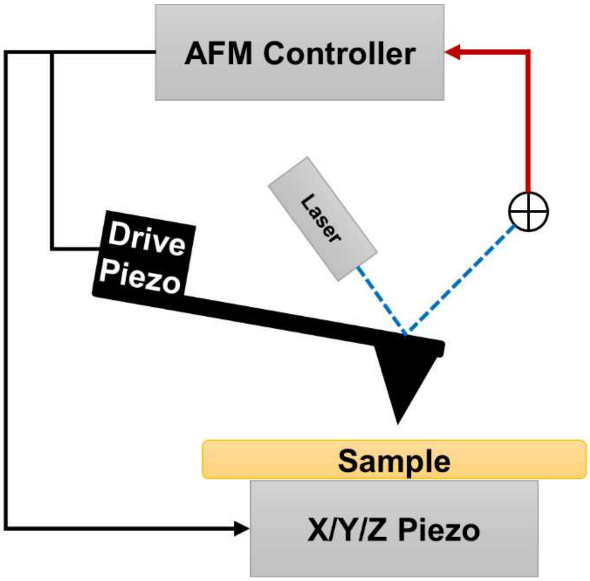

Figure 1.1. An illustration of an AFM setup.

1.2.1 *Contact Mode*

Contact mode, as the name suggests, is a mode where the tip is touching the surface (~0.5 nm plowing depth) and dragged across while scanning. The measurement is done either using the feedback signal that keeps the cantilever at a constant position or using the cantilever deflection directly. Contact mode suffers from noise and drift significantly, since it uses a static signal. To overcome this issue, soft cantilevers are generally employed to amplify the deflection signal. Another disadvantage of contact mode is that soft substrates get damaged by the tip. Nonetheless, contact mode is essential to some spectroscopic modes, i.e. dynamic force spectroscopy, based on measurements of deflection, phase and amplitude changes as the tip approaches a substrate and retracts from it. These approach-retraction curves are also called force curves, which is the measurement mode that we use for our machine learning algorithms in Chapter 3.

1.2.2 *Dynamic Modes*

Dynamic modes of AFM are non-contact mode and tapping mode. It can be said that the tip "feels" the surface rather than "touching" it. In both of these modes, the tip is not in contact with the sample constantly. The cantilever oscillates at a frequency close its resonance frequency; and either the tip hovers above the sample or intermittently touches the surface at the perigee of its motion. Nonetheless, both of these modes can be described by a classical damped driven harmonic oscillator for small angle deflections given by the equation:

$$\frac{d^2z}{dt^2} + \frac{\omega_0}{Q}\frac{dz}{dt} + {\omega_0}^2 z = \frac{F_0}{m}\sin(\omega t)\,, \tag{1.1}$$

where z is displacement of the tip, ω_0 is the resonance frequency of the cantilever, Q is the quality factor, F_0 is the driving force and m is the effective cantilever mass. Now, we describe these modes briefly.

1.2.2.1 Non-contact Mode

In non-contact mode, the tip hovers above the sample, oscillating at or near its resonance frequency. The amplitude of oscillation is adjusted in a way that the tip gets close to the surface (< 10 nm) at the end of its oscillation. When the tip is near the surface, it interacts with long-range forces, mostly van der Waals forces. This interaction causes a decrease in the resonance frequency of the tip. Coupled with a feedback loop, the system tries to keep oscillation amplitude or frequency constant by changing the distance between the base of the cantilever and the sample.

Non-contact mode does not experience tip or sample degradation that contact mode does. It is the preferred method for measuring soft samples, such as organic films or biological substrates. Many advanced AFM techniques, such as electrostatic force microscopy, are based on non-contact mode.

1.2.2.2 Tapping Mode

Contact mode suffers from tip-induced damage in biological surfaces and soft materials; and non-contact mode cannot reveal the real surface when the microscope is operated in air, due to a large meniscus force formed by the capillary condensation. These reasons pushed the development of tapping mode (intermittent contact mode).[32] In tapping mode, the cantilever is driven to oscillate at or near its resonance frequency and it strikes the surface on each oscillation. The oscillation amplitude is adjusted in a way that the tip can overcome the stickiness of the surface after every intermittent contact. Thus, it results in higher amplitude than non-contact mode operation. The feedback system measures the oscillation amplitude and the average tip-sample separation is adjusted to keep the oscillation amplitude constant.

1.3 Electrostatic Force Microscopy (EFM)

1.3.1 *Operating Principle*

Electrostatic Force Microscopy (EFM) maps electric properties of a sample by measuring the electrostatic forces between the tip and the sample. This is achieved by applying a potential bias between the cantilever and the sample while the cantilever is hovering above the surface and oscillating at or near its resonance frequency. In EFM, the topography of the surface is scanned initially, then the cantilever is raised to a constant distance from the surface and a bias applied. It works on two main principles. First, van der Waals forces are short range forces ($1/r^6$) and Coulombic forces are long range forces ($1/r^2$). Thus, when the cantilever is lifted away from the surface, it only interacts through Coulombic forces. Second, the topography line is the line of constant van der Waals forces, thereby keeping the cantilever at a constant distance from the surface during EFM pass allows measurement of Coulombic forces by measuring capacitance.

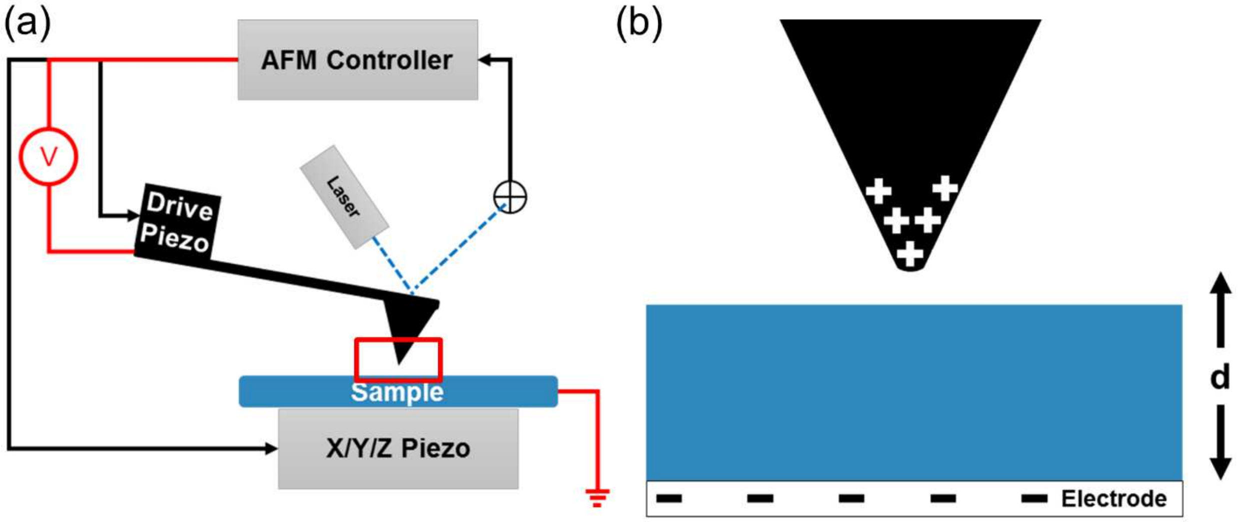

Figure 1.2. Schematics of EFM operation showing differences from normal AFM mode operation in **(a)**, denoted with red color; and **(b)** shows the illustration of the tip sample interaction (red box in **(a)**).

In Figure 1.2(a), we show an illustration of EFM mode. Compared to dynamic non-contact AFM mode, it has the cantilever connected to a voltage source and the sample is grounded. In this manner, the tip and the sample forms a capacitor with capacitance *C* as shown in Figure 1.2(b), which changes as the tip scans over the surface. We can write the total energy stored in this capacitor as follows:

$$U = \frac{1}{2}C\left(V_{tip} - V_{sample}\right)^2, \tag{1.2}$$

where V_{tip} is the potential on the tip and V_{sample} is the potential on the sample. The electrostatic force between the tip and sample then will be:

$$\boldsymbol{F_e} = -\nabla \mathrm{U} = -\frac{1}{2}\frac{\partial C}{\partial z}\left(V_{tip} - V_{sample}\right)^2 \boldsymbol{z}. \tag{1.3}$$

Using Hooke's law, assuming that the deflections on the cantilever is small, we can balance the equation:

$$z = \frac{1}{2k_0}\frac{\partial C}{\partial z}\Delta V^2, \tag{1.4}$$

where k_0 is the spring constant of the cantilever. Now, we see that the equilibrium deflection is a quadratic function of voltage difference. Moreover, the applied voltage will also change the cantilever's resonance frequency by changing the spring constant. In order to see how this happens, we start with expanding the derivative of capacitance around $z = 0$:

$$C'(z) = C'(0) + zC''(0) + \mathcal{O}(z^2), \tag{1.5}$$

which is valid when z is much smaller than the tip radius. To the first order, F_e can be approximated as:

$$F_e \cong \frac{1}{2}C'\Delta V^2 + \frac{1}{2}C''\Delta V^2 z. \tag{1.6}$$

This let us describe the net restoring force linear in z, which in turn lets us define an effective spring constant:

$$k = k_0 - \frac{1}{2}C''\Delta V^2. \tag{1.7}$$

Using this spring constant, we can redefine the resonance frequency of the cantilever:

$$\omega \rightarrow \omega_0 - \frac{\omega_0}{4k_0}C''\Delta V^2. \tag{1.8}$$

As a result, we expect the resonance frequency of the cantilever to shift in a quadratic way with respect to the voltage bias and the capacitance between the tip and the sample. We show an experimental result for this in Figure 1.3. Note that the apex of the curve is not at zero, since the surface voltage is different than zero.

In EFM experiments, the shift in the cantilever drive frequency required to keep the cantilever on resonance is measured as a voltage is applied between the tip and the sample. By measuring the change in the drive frequency at a constant voltage, we can measure how much the electrostatic force gradient is changing. However, EFM is not sensitive to the dynamic processes and cannot measure how fast these processes happening, thus pushing the development of time-resolved EFM.

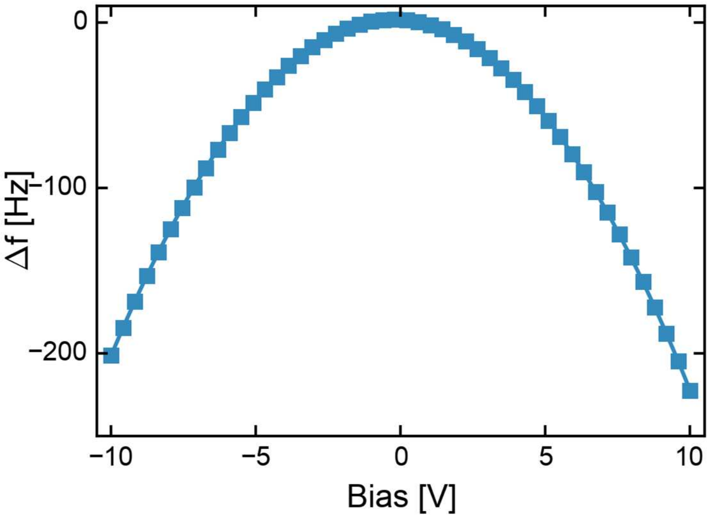

Figure 1.3. Quadratic behavior of the resonance frequency with respect to bias on the tip.

1.3.2 *Time-Resolved EFM*

The electrostatic forces we measure by EFM can be increased or decreased by applying a perturbation to the sample under investigation. The goal of time-resolved EFM (trEFM) is to measure the time evolution of this perturbative change. It was first invented by Coffey et al in 2006.[17] It is done by measuring the shift in the cantilever drive frequency required to keep the cantilever on resonance is measured in temporal domain in addition to spatial domain.

In Figure 1.4(a), we show an illustration of trEFM, where a laser is used as the perturbation on a photoactive sample. The charge distribution in the sample changes after the perturbation, thus changing the electrostatic force gradient between the tip and the sample as shown in Figure 1.4(b). By measuring the required shift in the drive frequency in time, we can determine the time dependency of the electrostatic force gradient. Figure 1.5 shows how the quadratic behavior of the frequency shift changes when the photoactive sample is under constant illumination as the capacitance increases due to charges getting closer to the tip (see Figure 1.4(b)).

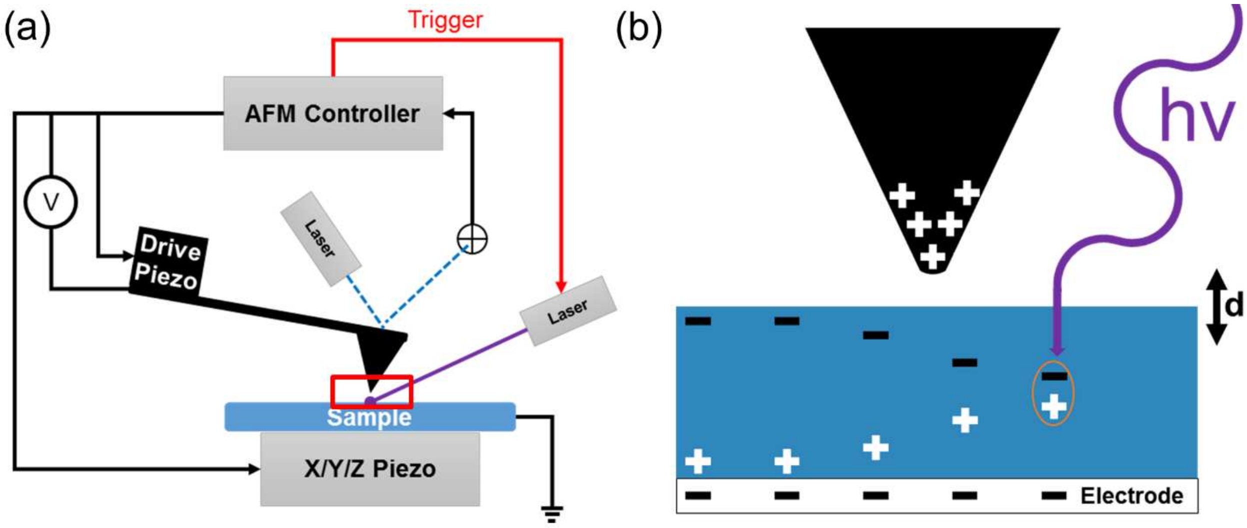

Figure 1.4. Schematics of trEFM operation showing differences from normal AFM mode operation in **(a)**, denoted with red color; and **(b)** shows the illustration of the tip-sample interaction (red box in **(a)**) when a perturbation happens, here a photoactive sample is illuminated.

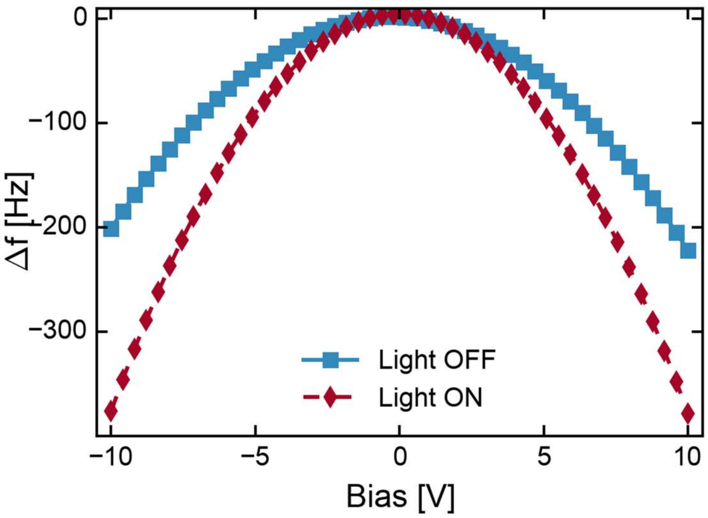

Figure 1.5. Quadratic behavior of the resonance frequency under perturbation with respect to bias on the tip for a photoactive material when the light is turned on (red) and off (blue).

The operation of trEFM method is very similar to EFM: (i) it acquires the surface topography, (ii) lifts up the cantilever to a predefined height from the surface, and (iii) applies a perturbation to sample and measures the change in the drive frequency as the sample is perturbed externally. However, the time resolution of trEFM is limited by the response of its feedback loop's response time (~10 µs), thereby pushing the development of time-resolved techniques without a feedback loop. In Chapter 2, we describe such a method using trEFM as a basis without a feedback loop.

1.4 Organic Photovoltaics (OPVs)

Photovoltaic devices create electricity through photogeneration of charge carriers, where a photon hits a semiconducting material (the active layer) and gets absorbed; this generates an electron-hole pair (exciton). For current to be generated, this electron-hole pair needs to be separated and collected at electrodes. There are two types of electron-hole pairs, namely Wannier-Mott and Frenkel excitons. Wannier-Mott excitons are generally found in elemental or inorganic compound semiconductors, where the dielectric constant of material is large. Due to large dielectric constant, electric field screening reduces the Coulombic interaction between electron and holes, thereby resulting in an exciton with small binding energy (~ 0.01 eV) and larger radius than the lattice spacing. Frenkel excitons are typically found in organic molecular and alkali-halide semiconductors. Frenkel excitons have much shorter radii (~10 Å) and larger binding energies on the order of 0.1 to 1 eV. This is caused by the smaller dielectric constants in these type of materials.

Many different semiconducting materials have been successfully used in photovoltaic devices, such as silicon, germanium, GaAs, and various organic materials. Use of organic materials as active layers in photovoltaic devices dates back to mid-20th century.[33,34] Due to organic materials' small dielectric constants, they form Frenkel excitons. Frenkel excitons cannot be easily separated in conventional single layer architecture due to their smaller radii and large binding energies, where the active layer is sandwiched between two electrodes. This causes low efficiencies in the

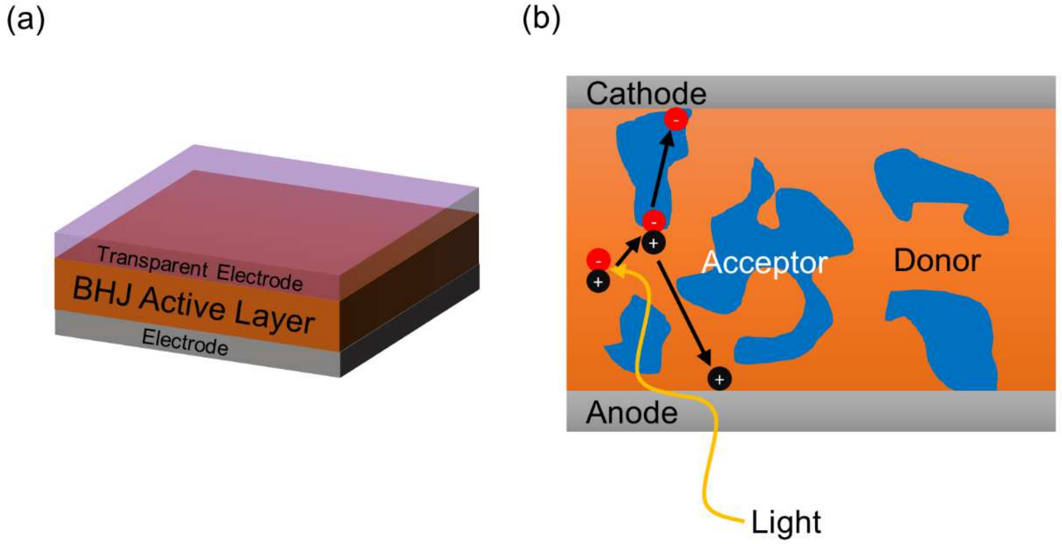

Figure 1.6. Schematics of bulk heterojunction OPV device stack and cross-section. **(a)** Device stack for bulk heterojunction (BHJ) OPV architecture, and **(b)** cross-section of the device. A photon gets absorbed by the donor material, and creates an exciton. The exciton moves to the acceptor-donor interface and disassociates. Then, the electron and hole get collected at their respective electrodes.

single-layer homo-junction OPVs. The first advance in device architecture to try to overcome fast recombination of electron-hole pairs came from Tang in 1986, by separating active layer into two layers, electron-donating (donor) and electron-accepting (acceptor) layer, he was able to greatly improve exciton separation and thereby the device performance.[35]

After that, the next logical step was to increase the donor-acceptor interfacial surface area, which in turn would increase the exciton dissociation and thus the performance. Yu et al, in 1995, showed first bulk heterojunction devices with increased performances.[36,37] The bulk heterojunction device architecture (see Figure 1.6) has enabled significant enhancements in OPV efficiencies. Nonetheless, after two decades, OPVs are still lagging behind their inorganic counterparts. There are a few different strategies one can follow to increase the device efficiency of OPVs: bandgap tuning,[38–40] stacking multiple cells,[31,41,42] nanostructuring,[43,44] increasing the charge mobility, and using plasmonic nanoparticles as means of optical engineering.[45–53] Among these, the use of plasmonic nanoparticles comes forward as a method that does not require modification of the materials composing the cell and can be incorporated easily to wet-bench processing of OPVs.

1.5 Plasmonics

The origins of the field of plasmonics can be traced back to the early 20th century. One example is Gustav Mie's solution to scattering of electromagnetic waves from particles that have sizes comparable to the wavelength of the wave.[54] In 1952, Pines and Bohm proposed a quasiparticle, the plasmon, arising from the quantization of classical plasma oscillations.[55] In the classical picture, plasmons can be described as an oscillation of free electrons with respect to fixed charges in a metal. Since plasmonics is not the main topic of this dissertation, we are not going to describe their properties for the sake of brevity.

Surface plasmons are plasmons that exist at the metal-dielectric interface; their existence was first predicted in 1957.[56] The motion of the charges at the interface creates an electromagnetic wave outside of the metal. Thus giving rise to a coupled surface plasmon and photon quasiparticle, which is called a surface plasmon polariton at a planar interface, or localized surface plasmon at a closed surface of a nanoparticle. Localized surface plasmons have two main effects: (i) electric fields near the nanoparticle are enhanced significantly, and (ii) the incident light is strongly scattered. Both these effects can be controlled by means of size, composition, and placement of nanoparticles. In this manner, using metal nanoparticles inside OPVs to engineer optical effects can improve the performance of OPVs considerably.[45]

1.6 Structure of the Dissertation

In Chapter 2, we describe the hardware and software implementations of fast trEFM in detail, which can measure fast local dynamics following a perturbation to an electronically active device by means of an oscillating cantilevers. We show computationally and experimentally that the time-resolution of trEFM is affected by when the perturbation is turned on with respect to the cantilever motion. We investigate how one can increase the time resolution and show that we can distinguish time constants as short as 10 ns for an exponentially decaying signal.

In Chapter 3, we develop machine learning models to classify force curves acquired by dynamic force spectroscopy of double-stranded DNA. In order to extract useful information from acquired force curves, one should label all the curves as either successful or unsuccessful, which is a time consuming process. We show that with random forest models we can reach an accuracy of 94%. We also show that it is possible to reach 80% accuracy using an unsupervised model.

In Chapter 4, we use computational modeling and experiment to investigate the performance limits of a modern bulk heterojunction thin-film device with embedded silver nanoparticles. We explore the parameter space of position, density and thickness using computational modeling; and we propose a guideline for designing such devices. Using this guideline, we design a device with the power conversion efficiency increasing from 5.95% to 7.83%.

Every chapter has an accompanying appendix. Respectively, Chapters 2, 3, and 4 are accompanied by Appendices A, B, and C.

1.7 References

[1] J.W. Cooley and J.W. Tukey, Math. Comput. **19**, 297 (1965).

[2] N. Metropolis, A.W. Rosenbluth, M.N. Rosenbluth, A.H. Teller, and E. Teller, J. Chem. Phys. **21**, 1087 (1953).

[3] W.K. Hastings, Biometrika **57**, 97 (1970).

[4] P. Larranaga, Brief. Bioinform. **7**, 86 (2006).

[5] A. Varnek and I. Baskin, J. Chem. Inf. Model. **52**, 1413 (2012).

[6] G. Binnig and H. Rohrer, Helv. Phys. Acta **55**, 726 (1982).

[7] G. Binnig, C.F. Quate, and C. Gerber, Phys. Rev. Lett. **56**, 930 (1986).

[8] J.L. Luria, N. Hoepker, R. Bruce, A.R. Jacobs, C. Groves, and J.A. Marohn, ACS Nano **6**, 9392 (2012).

[9] M.J. Jaquith, J.E. Anthony, and J. a. Marohn, J. Mater. Chem. **19**, 6116 (2009).

[10] N. Hoepker, S. Lekkala, R.F. Loring, and J.A. Marohn, J. Phys. Chem. B **115**, 14493 (2011).

[11] S. Lekkala, N. Hoepker, J.A. Marohn, and R.F. Loring, J. Chem. Phys. **137**, 124701 (2012).

[12] J.R. O'Dea, L.M. Brown, N. Hoepker, J.A. Marohn, and S. Sadewasser, MRS Bull. **37**, 642 (2012).

[13] W.R. Silveira, E.M. Muller, T.N. Ng, D. Dunlap, and J.A. Marohn, in *Scanning Probe Microscopy* (Springer New York, New York, NY, 2007), pp. 788–830.

[14] M.J. Jaquith, E.M. Muller, and J.A. Marohn, J. Phys. Chem. B **111**, 7711 (2007).

[15] D.C. Coffey, O.G. Reid, D.B. Rodovsky, G.P. Bartholomew, and D.S. Ginger, Nano Lett. **7**, 738 (2007).

[16] P.A. Cox, M.S. Glaz, J.S. Harrison, S.R. Peurifoy, D.C. Coffey, and D.S. Ginger, J. Phys. Chem. Lett. **6**, 2852 (2015).

[17] D.C. Coffey and D.S. Ginger, Nat. Mater. **5**, 735 (2006).

[18] R. Giridharagopal, G.E. Rayermann, G. Shao, D.T. Moore, O.G. Reid, A.F. Tillack, D.J. Masiello, and D.S. Ginger, Nano Lett. **12**, 893 (2012).

[19] L.H. Pope, M.C. Davies, C. a Laughton, C.J. Roberts, S.J.B. Tendler, and P.M. Williams, Eur. Biophys. J. **30**, 53 (2001).

[20] T. Strunz, K. Oroszlan, R. Schafer, and H.-J. Guntherodt, Proc. Natl. Acad. Sci. **96**, 11277 (1999).

[21] E. Sengupta, Y. Yan, X. Wang, K. Munechika, and D.S. Ginger, ACS Nano **8**, 2625 (2014).

[22] A.R. Bizzarri and S. Cannistraro, Chem. Soc. Rev. **39**, 734 (2010).

[23] J.Y. Kwon, K.S. Son, J.S. Jung, T.S. Kim, M.K. Ryu, K.B. Park, B.W. Yoo, J.W. Kim, Y.G. Lee, K.C. Park, S.Y. Lee, and J.M. Kim, IEEE Electron Device Lett. **29**, 1309 (2008).

[24] I. Yagi, N. Hirai, Y. Miyamoto, M. Noda, A. Imaoka, N. Yoneya, K. Nomoto, J. Kasahara, A. Yumoto, and T. Urabe, J. Soc. Inf. Disp. **16**, 15 (2008).
[25] G.S. Ryu, J.S. Kim, S.H. Jeong, and C.K. Song, Org. Electron. **14**, 1218 (2013).
[26] E. Cantatore, T.C.T. Geuns, G.H. Gelinck, E. van Veenendaal, A.F. a Gruijthuijsen, L. Schrijnemakers, S. Drews, and D.M. de Leeuw, IEEE J. Solid-State Circuits **42**, 84 (2007).
[27] C.D. Dimitrakopoulos and P.R. Malenfant, Adv. Mater. **14**, 99 (2002).
[28] H. Ma, H.-L. Yip, F. Huang, and A.K.-Y. Jen, Adv. Funct. Mater. **20**, 1371 (2010).
[29] M.O. Reese, S.A. Gevorgyan, M. Jørgensen, E. Bundgaard, S.R. Kurtz, D.S. Ginley, D.C. Olson, M.T. Lloyd, P. Morvillo, E.A. Katz, A. Elschner, O. Haillant, T.R. Currier, V. Shrotriya, M. Hermenau, M. Riede, K. R. Kirov, G. Trimmel, T. Rath, O. Inganäs, F. Zhang, M. Andersson, K. Tvingstedt, M. Lira-Cantu, D. Laird, C. McGuiness, S. (Jimmy) Gowrisanker, M. Pannone, M. Xiao, J. Hauch, R. Steim, D.M. DeLongchamp, R. Rösch, H. Hoppe, N. Espinosa, A. Urbina, G. Yaman-Uzunoglu, J.-B. Bonekamp, A.J.J.M. van Breemen, C. Girotto, E. Voroshazi, and F.C. Krebs, Sol. Energy Mater. Sol. Cells **95**, 1253 (2011).
[30] G. Li, R. Zhu, and Y. Yang, Nat. Photonics **6**, 153 (2012).
[31] C.-C. Chen, W.-H. Chang, K. Yoshimura, K. Ohya, J. You, J. Gao, Z. Hong, and Y. Yang, Adv. Mater. **26**, 5670 (2014).
[32] Q. Zhong, D. Inniss, K. Kjoller, and V.B. Elings, Surf. Sci. Lett. **290**, L688 (1993).
[33] C. Brabec, U. Scherf, and V. Dyakonov, editors , *Organic Photovoltaics* (Wiley-VCH Verlag GmbH & Co. KGaA, Weinheim, Germany, 2014).
[34] G.A. Chamberlain, Sol. Cells **8**, 47 (1983).
[35] C.W. Tang, Appl. Phys. Lett. **48**, 183 (1986).
[36] G. Yu and A.J. Heeger, J. Appl. Phys. **78**, 4510 (1995).
[37] G. Yu, J. Gao, J.C. Hummelen, F. Wudl, and A.J. Heeger, Science **270**, 1789 (1995).
[38] D. Mühlbacher, M. Scharber, M. Morana, Z. Zhu, D. Waller, R. Gaudiana, and C.J. Brabec, Adv. Mater. **18**, 2884 (2006).
[39] M.M. Wienk, M.G.R. Turbiez, M.P. Struijk, M. Fonrodona, and R.A.J. Janssen, Appl. Phys. Lett. **88**, 153511 (2006).
[40] J. Peet, J.Y. Kim, N.E. Coates, W.L. Ma, D. Moses, A.J. Heeger, and G.C. Bazan, Nat. Mater. **6**, 497 (2007).
[41] W. Li, A. Furlan, K.H. Hendriks, M.M. Wienk, and R. a J. Janssen, J. Am. Chem. Soc. **135**, 5529 (2013).
[42] S. Esiner, H. van Eersel, M.M. Wienk, and R.A.J. Janssen, Adv. Mater. **25**, 2932 (2013).
[43] K.M. Coakley and M.D. McGehee, Chem. Mater. **16**, 4533 (2004).
[44] C. Goh, K.M. Coakley, and M.D. McGehee, Nano Lett. **5**, 1545 (2005).
[45] H.A. Atwater and A. Polman, Nat. Mater. **9**, 865 (2010).
[46] E. Stratakis and E. Kymakis, Mater. Today **16**, 133 (2013).
[47] X. Yang, C.-C. Chueh, C.-Z. Li, H.-L. Yip, P. Yin, H. Chen, W.-C. Chen, and A.K.-Y. Jen, Adv. Energy Mater. **3**, 666 (2013).
[48] Q. Gan, F.J. Bartoli, and Z.H. Kafafi, Adv. Mater. **25**, 2385 (2013).
[49] S.-W. Baek, G. Park, J. Noh, C. Cho, C.-H. Lee, M.-K. Seo, H. Song, and J.-Y. Lee, ACS Nano **8**, 3302 (2014).
[50] G.D. Spyropoulos, M.M. Stylianakis, E. Stratakis, and E. Kymakis, Appl. Phys. Lett. **100**, 213904 (2012).
[51] D.H. Wang, J.K. Kim, G.-H. Lim, K.H. Park, O.O. Park, B. Lim, and J.H. Park, RSC Adv. **2**, 7268 (2012).

[52] C.-H. Kim, S.-H. Cha, S.C. Kim, M. Song, J. Lee, W.S. Shin, S.-J. Moon, J.H. Bahng, N. a. Kotov, and S.-H. Jin, ACS Nano **5**, 3319 (2011).
[53] R.B. Dunbar, T. Pfadler, and L. Schmidt-Mende, Opt. Express **20**, A177 (2012).
[54] G. Mie, Ann. Phys. **330**, 377 (1908).
[55] D. Pines and D. Bohm, Phys. Rev. **85**, 338 (1952).
[56] R.H. Ritchie, Phys. Rev. **106**, 874 (1957).

Chapter 2. Fast Time-Resolved EFM

2.1 Introduction[a]

Electrostatic force microscopy (EFM) is a non-contact atomic force microscopy technique, commonly utilized to study electronic properties of materials, with nanoscale spatial resolution. Researchers have used EFM methods to investigate different phenomena such as characterizing local defects,[1–4] measuring local dielectric constants[5–7] and probing ionic conduction.[8] Despite these many applications, conventional EFM methods do not capture dynamic information at time scales relevant to many physical properties of interest. Time-resolved EFM has been used to measure events on timescales ranging from the order of seconds[1,2,8,9] to milliseconds.[3] A variety of methods have also been employed to measure local dynamics in a sub-diffraction limited volume with scanning probes; these include methods such as near-field scanning optical microscopy[10,11] and scanning tunneling microscopy with pulsed laser optics.[12,13] However, these methods typically require complex optics and expensive hardware beyond the scanning probe microscope.

Motivated by the need for new methods to understand sub-diffraction-limited processes in emerging thin-film materials,[14–17] our research group reported a trEFM method to capture information on time scales as fast as 100 μs using frequency-shift feedback.[18] With a focus on probing optoelectronic processes in nanostructured materials, we showed that trEFM measurements can be used to make local photovoltaic quantum efficiency maps as a function of many parameters, such as materials composition and processing,[18–20] photodegradation,[21,22] and

---

[a] This chapter is adapted from: D. U. Karatay, J. S. Harrison, M. Glaz, R. Giridharagopal, D. S. Ginger, Fast Time-Resolved Electrostatic Force Microscopy: Achieving Sub-Cycle Time Resolution. Submitted to Review of Scientific Instruments.

excitation wavelength.[20,22] We recently used trEFM to demonstrate non-contact imaging of local currents with the equivalent of attoampere sensitivity.[20]

However, many interesting processes occur on timescales faster than it can be resolved with feedback-mode trEFM. For example, monomolecular carrier lifetimes in hybrid perovskites[23,24] can be on the order of 10 ns – 1 μs in thin films used for solar cell applications, while carrier lifetimes in state-of-the-art polymer bulk heterojunctions are typically on the order of 1 μs or less under AM1.5G illumination.[25,26] Some biological processes, such as ion channel gating,[27] synaptic transmission[28] and electron transport in photosynthesis,[29] happen at time scales on the order of 1 ns - 1 μs.

In our initial implementation of trEFM,[18] the time resolution was primarily limited by the bandwidth of the frequency-shift feedback loop. By combining a feedback-free approach with signal averaging and analyzing the cantilever motion, we later demonstrated sub-microsecond time resolution in trEFM.[19] Here, we describe in detail a robust implementation of feedback-free trEFM. We place particular emphasis on the importance of phase-locking the excitation signal, the opportunities for reducing system noise via methods such as photothermal drive,[30–34] and the selection of cantilever parameters. Finally, we show that with improved software implementation it is possible to process the gigabyte-scale datasets required to render trEFM images concurrently with data acquisition, realizing approximately 10-fold improvement in image display speed.

2.2 Experimental Setup

The experimental apparatus consists of a commercially available atomic force microscope (AFM) (Asylum Research Cypher-ES), an off-the-shelf digitizer (Gage CSE1622), trigger circuitry (built in-house, see Appendix A for details)[35] and a pulsed excitation source: either light or voltage (here a function generator, Agilent 33500B). Figure 2.1(a) depicts the experimental

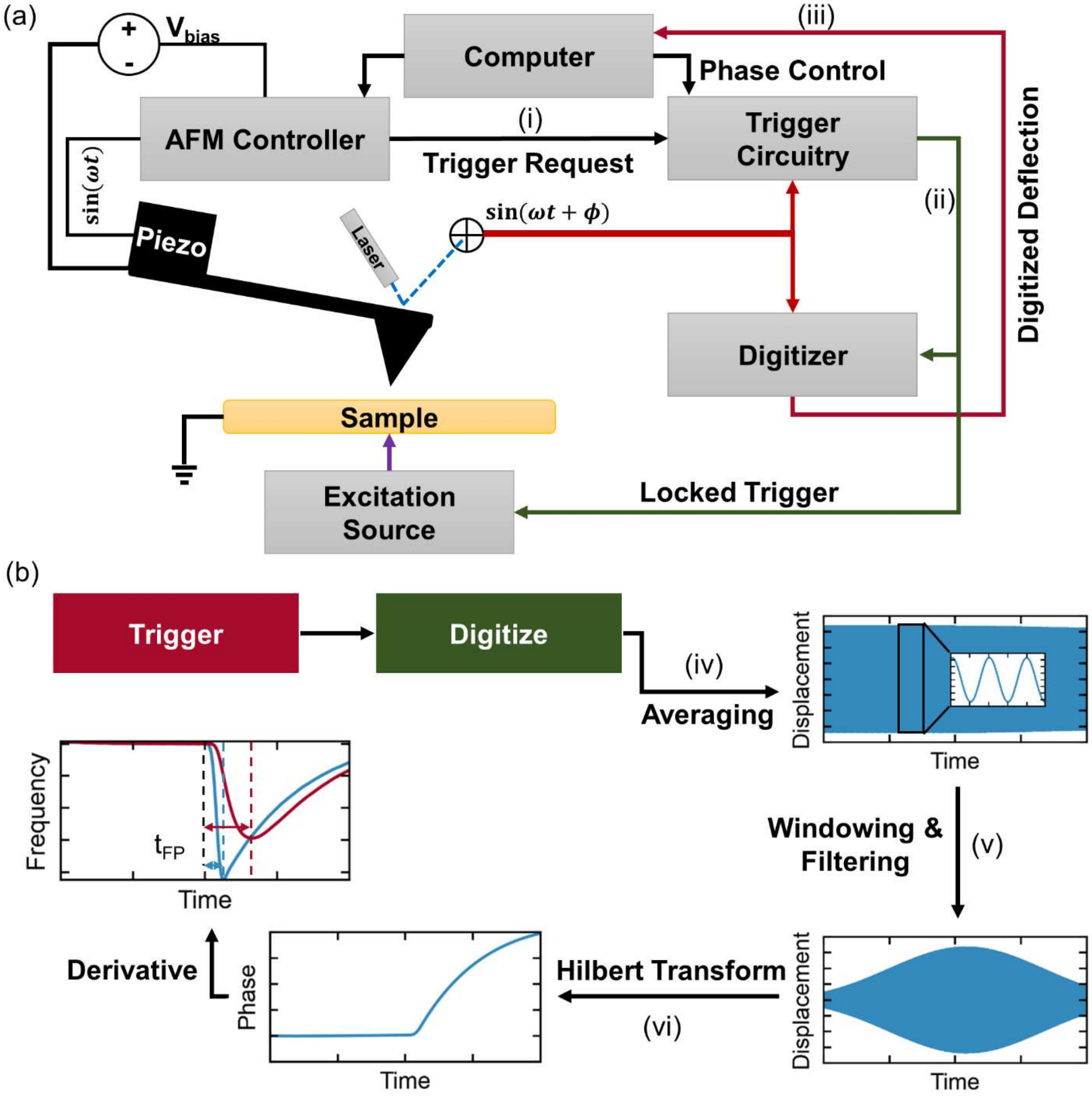

Figure 2.1. Schematics of fast trEFM setup. **(a)** Schematic of the experimental setup: (i) Computer requests a trigger at a defined phase of the oscillation, (ii) trigger circuitry triggers the digitizer and the excitation source accordingly, and (iii) the digitizer transfers the acquired signals to computer. **(b)** Flow diagram of the data analysis procedure after the acquisition: (iv) signals are averaged together, (v) windowed and filtered, (vi) demodulated via Hilbert transform to find the instantaneous frequency of the cantilever (Instantaneous frequency curves for excitations with time constants of 25 ns and 100 µs are shown).

scheme. The goal of the trEFM method is to measure how quickly the electrostatic interaction between the cantilever and the sample is changing in response to the excitation. We use a scan-lift-rescan approach[36–38] to track the topography while minimizing short-range interactions. The instrument first acquires a topography scan in AC mode. The cantilever is then raised to a user-defined height from the surface (typically 10-100 nm) and then performs the time-resolved EFM (trEFM) pass during a second scan with the cantilever retracing the recorded topography line at a fixed height chosen to minimize short range interactions, such as van der Waals forces, while remaining sensitive to longer range electrostatic forces.

During the trEFM pass, we first apply a voltage bias between the cantilever and the sample (typical $V_{bias} \sim$ 5-10 V). After the cantilever reaches equilibrium (2-4 ms) we apply a user-defined perturbation, such as a light pulse or voltage between the cantilever and the sample, at a user chosen point in the cantilever oscillation cycle. This perturbation induces transient deviations from the sinusoidal motion of the cantilever, which we record by digitizing the cantilever displacement signal with a fast acquisition card. We record the cantilever motion at a sampling rate of 10 MHz with 16-bit precision over a user-defined window (typically 0.8-3.2 ms) before and after the sample perturbation. The entire process is typically 16 ms per data point. In a line scan, we bin collected signals to pixels and average them before processing; in a point scan, we collect signals at a single spot and average them before processing. A line scan is typically 1920 signals over 64 pixels (30 averages per pixel) or 128 pixels (15 averages per pixel), though higher averages-per-pixel can be acquired at the expense of time-per-scan. We then process the data to extract the frequency information as described below.

We introduced the data analysis process in previous work.[19,39] In brief, we use the Hilbert transform to convert the cantilever motion into time-dependent frequency information.[40,41]

Importantly, we first average the deflection vs. time traces for a number of trigger signals acquired at the same spot and at the same phase to improve our signal-to-noise ratio. We then multiply the average signal by a windowing function to reduce edge effects and spectral leakage, which is the temporal effect of a finite sampling window becoming apparent in the Fourier transform. We chose a Blackman window because it is designed to minimize spectral leakage and optimize its peak's concentration around the center frequency.[42,43] We filter the signal with a finite-impulse-response (FIR) filter, since FIR filters can be built to have linear phase response and are stable.[43] The FIR filter we use is a causal filter to preserve the time-ordering of the data series. However, as all filters, the FIR filter delays the signal by $(N - 1) / (2f_s)$, where N is the number of taps and f_s is the sampling frequency. As a result, we correct the delay in the location of trigger. We then apply a Hilbert transform on the windowed and filtered signal to obtain the analytical signal from which we extract the instantaneous phase of the cantilever.[19,40] We take the derivative of the instantaneous phase with respect to time to yield the instantaneous frequency of the AFM cantilever. From the instantaneous frequency curve, we find when the minimum frequency occurred and the duration between the event and the minimum, which we use as a metric "time to first peak" (t_{FP}) as shown in Figure 2.1(b) for two different excitations of varying time constants. The procedure for finding the minimum of the curve is described in Appendix A.[35]

Here, we focus on characterizing the system's response to single-exponential signals, because many systems of interest exhibit either first-order, or pseudo-first-order dynamics,[18,44,45] and indeed we have observed such behavior in trEFM data on real systems.[18,20,21] To create the perturbation, we apply an exponentially rising voltage to a gold electrode of the form:

$$V_{pp}\left(1 - e^{-\frac{t}{\tau}}\right), \tag{2.1}$$

where V_{pp} is peak-to-peak voltage, t is time and τ is the characteristic time, ranging from 10 ns to 1 ms. For AFM cantilevers, we use commercially available Bruker DDESP-V2, BudgetSensors ElectriTap300-G, ElectriTap190-G and ElectriMulti75-G with manufacturer-specified resonance frequencies of 450, 300, 190, and 75 kHz and spring constants of 80, 40, 48, and 3 N/m. All BudgetSensors tips are expected to have less than a 25 nm radius, and Bruker DDESP-V2 tips to have less than a 150 nm radius.

2.3 Numerical Description of trEFM Experiments

To thoroughly understand the underlying physics of the fast-time dynamics of the cantilever, we compare our experimental data with numerical simulations of the cantilever motion. We assume the cantilever behaves as a damped driven harmonic oscillator (DDHO):

$$\frac{d^2z}{dt^2} + \frac{\omega_0}{Q}\frac{dz}{dt} + {\omega_0}^2 z = \frac{F_0}{m}\sin(\omega t)\,, \tag{2.2}$$

where z is displacement of the tip, ω_0 is the resonance frequency of the cantilever, Q is the quality factor, F_0 is the driving force and m is the effective cantilever mass.

The voltage pulse applied to the cantilever will affect its motion in two primary ways.[46] First, the time-varying voltage will induce a time varying electrostatic force ($F_e(t)$) acting on the cantilever. Second, the change in $dF_e(t)/dz$, due to the height-dependence of the tip-sample capacitance, affects the cantilever motion.[47] In our experiments with time-dependent tip-sample potentials, we model this term as a time-dependent resonant frequency, $\omega_0(t)$, that changes to a value of $\omega_0(t)+\Delta\omega_0$ with the same time constant, τ, as the electrostatic perturbation:

$$\omega_0(t \geq 0) \cong \omega_0(t=0) + \Delta\omega_0(1 - e^{-t/\tau}), \tag{2.3}$$

$$\Delta\omega_0 = -\frac{\omega_0(0)}{2k}\frac{\partial F_e(t \to \infty)}{\partial z}, \tag{2.4}$$

where $\Delta\omega_0$ is the maximum frequency shift due to the electrostatic force gradient and k is the spring constant of the cantilever.

The electrostatic force F_e and the electrostatic force gradient dF_e/dz are both proportional to square of the total potential difference between the tip and sample:

$$\Delta V^2 = \left(V_{bias} + V_{pp}\right)^2. \tag{2.5}$$

We can write the voltage pulse as a time-dependent force and time-dependent force gradient modeling the system as a capacitor (C) of a conducting sphere floating above a conducting plane:[47]

$$F_e(t \geq 0) = \frac{1}{2}\frac{\partial C}{\partial z}V_{bias}^2\left(1 - e^{-t/\tau}\right) \cong -\varepsilon_0 \frac{\pi R^2}{\bar{z}^2}\Delta V^2\left(1 - e^{-t/\tau}\right), \tag{2.6}$$

$$\frac{\partial F_e(t \geq 0)}{\partial z} = \frac{1}{2}\frac{\partial^2 C}{\partial z^2}V_{bias}^2\left(1 - e^{-t/\tau}\right) \cong \varepsilon_0 \frac{2\pi R^2}{\bar{z}^3}\Delta V^2\left(1 - e^{-t/\tau}\right), \tag{2.7}$$

where we obtain the parameters R (radius of the tip) and $\bar{z}$ (the average distance between the tip and the sample) from experiment. Although Eqs. 6 and 7 are an approximation to the tip-sample capacitance, we emphasize that here we are interested primarily in the functional relationship, such as $F_e \sim \Delta V^2$ and $dF_e/dz \sim \Delta V^2$ rather than the exact prefactors. Combining Eqs. 2, 3 and 6, we can rewrite Eq. 2.2. as follows:[19]

$$\frac{d^2 z}{dt^2} + \frac{\omega_0(t)}{Q}\frac{dz}{dt} + \omega_0(t)^2 z = \frac{F_0}{m}\sin(\omega t + \theta) + \frac{F_e(t)}{m}, \tag{2.8}$$

In all simulations below, we have solved Eq. 2.8 using an ordinary differential equation solver with input parameters such as cantilever parameters (ω_0, k, m, Q) and force parameters (F_e, dF_e/dz) determined from experiment. We note that it is also possible for Q to exhibit a time dependence,[48,49] an effect we ignore here as it is not necessary to model our voltage pulse data.[19,46]

2.4 Results and Discussion

In our experiments, we used a gold electrode deposited on a silicon wafer in order to characterize the response of our system to known transient signals. We utilized a waveform generator as our excitation source to create exponential voltage transients (Eq. 2.1) with programmed rise times in order to simulate transient charge buildups or decays that might occur in systems of interest such as an optoelectronic device under optical excitation.

Using this model system to compare simulations and experimental data, we now explore the parameter space that defines the operation of trEFM in detail. **Figure 2.2** shows typical experimental displacement (*z*), phase (*θ*), frequency shift (*Δf*) vs. time following voltage pulses with 10 ns and 10 μs rise times applied to the cantilever with a resonance frequency of 503.327 kHz (and thus cantilever period of 1.98678 μs). We obtain phase and frequency shift via Hilbert

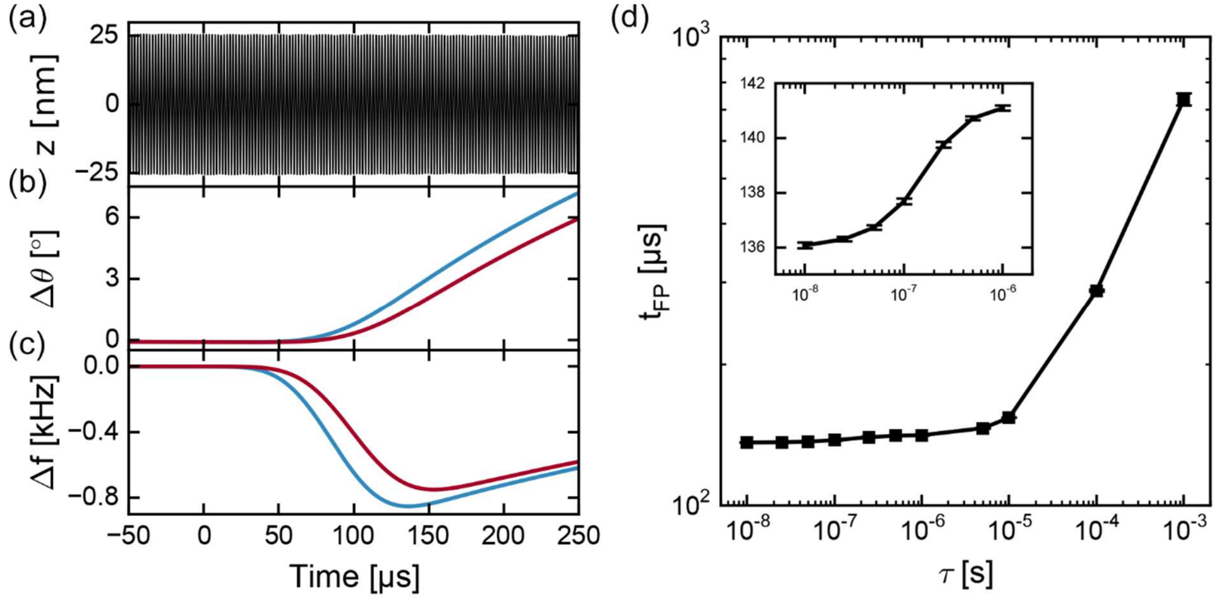

Figure 2.2. Processing flow of a calibration curve. **(a)** Deflection of a cantilever, **(b)** cantilever phase, **(c)** instantaneous frequency shift of the cantilever and **(d)** calibration curve for a range of characteristic times of exponential decay (τ) (inset shows a zoom-in for shorter times). Blue curves and red curves denote τ of 10 ns and 10 μs, respectively, where t = 0 is when excitation happens. The cantilever parameters are f_0 = 503.327 kHz, k = 72.7 N/m and Q = 499.

transform of the deflection data as explained in Section II. **Figure 2.2**(c) shows that there is no change in the frequency of the cantilever until excitation time ($t = 0$), and then the instantaneous frequency starts decreasing due to the transient motion of the cantilever being induced by the time-dependent electrostatic force and force gradient (**Figure 2.2**(c) also shows the effect of the causal filtering causing a lag in the frequency shift). After reaching a minimum in the frequency shift ($t = t_{FP}$), the transient change in the cantilever frequency diminishes as the cantilever returns to a sinusoidal oscillation at the drive frequency with a new amplitude and relaxation time constant given by $\tau_R = 2Q / \omega_0$. The exact value of t_{FP} depends on time constants of the excitation and the relaxation, as well as the processing parameters, such as the filter bandwidth and the number of FIR filter coefficients (throughout this paper, we keep the filter parameters the same for all experiments and simulations). Since the relaxation time constant is dominated by Q of the cantilever (rather than the electrostatic change in the sample), the transient behavior prior to the relaxation is key to recovering information about fast perturbations, which forms the center of our attention here. We focus on the time for the cantilever to reach the maximum instantaneous frequency deviation from the drive frequency, t_{FP} as a simplifying metric to parameterize the data.[19] We are able to extract information about the fast perturbations that are much shorter than a single oscillation period because cantilever oscillations start developing a phase lag after the excitation that propagates over timescales longer than the excitation's characteristic time constant. For example, in **Figure 2.2**(c), t_{FP} values of 136.41 μs and 153.7 μs are longer than the excitation with exponential time constants of 10 ns and 10 μs, respectively.

Figure 2.2(d) shows a plot of measured t_{FP} as a function of the input signal rise time, τ, which we call a calibration curve. The calibration curve serves as an experimental map to understand how t_{FP} is related to the excitation time and characteristics of the instrument, because there is one-to-one correspondence between t_{FP} and τ, down to a minimum distinguishable rise time. We consider "distinguishable rise time" to be where the change in t_{FP}'s for two consecutive τ's is greater than the sum of standard deviations of t_{FP}'s for those τ values:

$$\mu_{t_{FP}}(\tau_{i+1}) - \mu_{t_{FP}}(\tau_i) \geq \sigma_{t_{FP}}(\tau_{i+1}) + \sigma_{t_{FP}}(\tau_i). \tag{2.9}$$

In the inset of **Figure 2.2**(d), we show that the minimum distinguishable rise time is 10 ns with our current implementation, representing a 10-fold improvement over our previous efforts.[19] We next examine the factors required to obtain this monotonic calibration curve and reach a time-resolution of 10 ns, such as the dependence on the cantilever phase[39] during excitation, as well as other factors.

2.4.1 *Effect of Electrostatic Force*

As discussed in Section III and our earlier work[19], a time-varying tip-sample voltage will affect the instantaneous cantilever motion through two terms: the electrostatic force and the force gradient. In previous studies, the figure of merit for a frequency-modulation (FM) system has been the minimum detectable force gradient.[46,50,51]. The minimum detectable force gradient for an FM system in the absence of the electrostatic force term is[46,50,51]:

$$\delta F_{min} = \sqrt{\frac{4k_bTkB}{\omega_0 Q < z_{osc}^2 >}}, \tag{2.10}$$

where $<z_{osc}^2>$ is mean square displacement, ω_0 is the resonance frequency of the cantilever, Q is the quality factor, k_bT is the thermal energy at ambient temperature, k is the spring constant and B is the measurement bandwidth.

We model our experiments in two ways. First, the experiment is modeled using only the force gradient, then it is modeled using both the electrostatic force and the force gradient, unlike in previous studies. **Figure 2.3**(a) demonstrates that simulations including both the force and its

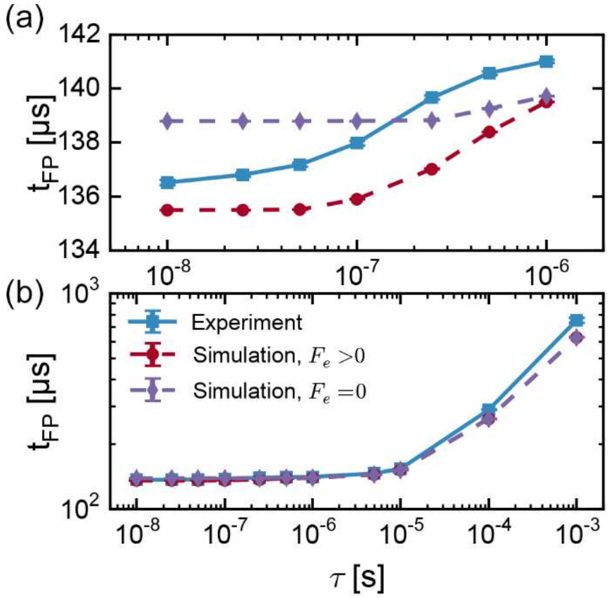

Figure 2.3. Comparison of experimental calibration curve with simulations showing that the inclusion of force in numerical description of the method is fundamental to replication of experimental results for shorter time scales as seen in **(a)**. For longer times, both simulations give the same results as in **(b)**. Solid curve and dashed curves denote experiment and simulations, respectively. The cantilever parameters are f_0 = 503.327 kHz, k = 72.7 N/m and Q = 499. Excitation is applied at the cantilever phase of 180°.

gradient capture the experimental trend for faster rise times, whereas the calibration curve of simulations including only the force gradient but not the force is flat for time scales faster than 100 ns. For rise times slower than 1 µs, simulations with and without the force term show the same trend and follow the experimental curve (for simulations and experiment, excitation is applied at the cantilever phase of 180°). Based on these models, we propose that the electrostatic force is an important component of trEFM method in the sub-cycle regime. This assumption is in contrast to previous literature that only included the force gradient instead of both the electrostatic force and the force gradient.[46] As discussed below, we conclude that, for rise times shorter than a cantilever period, the trEFM method is more sensitive to the force than the force gradient, and the electrostatic force is a significant component of the detection.

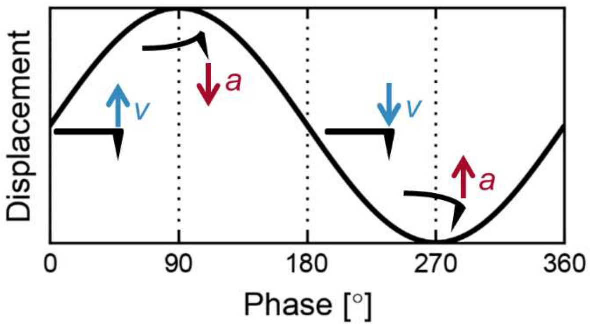

Figure 2.4. Illustration of cantilever displacement vs phase. Blue and red arrows denote velocity and acceleration on the cantilever, respectively. At phases 0° and 180°, there is no acceleration. At phases 90° and 270°, there is no velocity.

2.4.2 *Cantilever Phase at Excitation*

As discussed in the section above, the electrostatic force and force gradient components affect the minimum distinguishable rise time and the curvature of the calibration curve. We also expect the direction of the electrostatic force relative to the cantilever motion to have an effect on our measurements. In **Figure 2.4**, we illustrate the cantilever motion at different points in time and show velocity and acceleration vectors at four key phases. We hypothesized that the relative alignment of the electrostatic force vector with the damping force ($\boldsymbol{F}_{damping} = -2\beta\dot{z}\hat{z}$, where $\beta = \omega_0/2Q$) should affect the results. Following this qualitative analysis, we simulated the cantilever motion when it is perturbed by a time-varying electrical potential beginning during different relative phases of the oscillation cycle (**Figure 2.5**(a)).

In accordance with the qualitative discussion above, our numerical simulations show that for rise times longer than 1 μs, calibration curves behave monotonically at all phases (inset of **Figure 2.5**(a)). However, for shorter rise times, we can see that only calibration curves where the excitation was turned on at 180° and 270° behave monotonically, whereas other phases behave non-monotonically. This is a key observation; since we desire a one-to-one mapping between t_{FP} and τ values, we need t_{FP} to shift monotonically with τ.

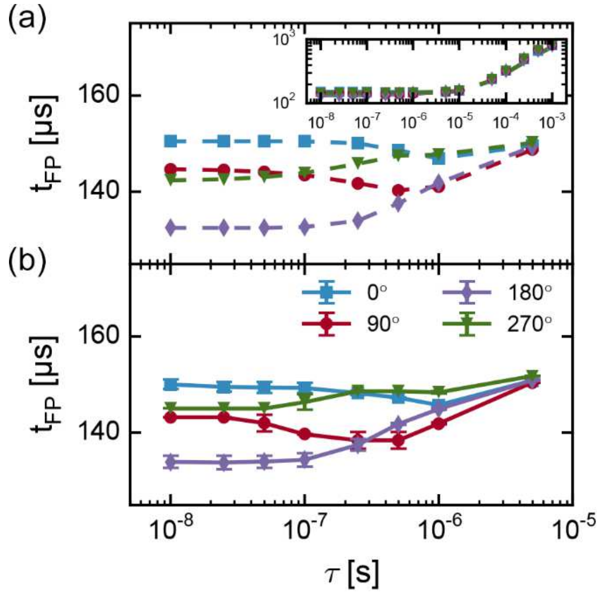

Figure 2.5. Effect of phase on the calibration curve. Comparison of **(a)** DDHO simulations and **(b)** experimental results for an AFM cantilever excited at different phases of deflection signal demonstrating that the phase of cantilever at the excitation time is important for detection of fast rise times. The cantilever parameters are f_0 = 272.218 kHz, k = 26.2 N/m and Q = 432. Inset shows the whole range of τ's for experiments and simulations (dashed lines are simulations; markers denote experiments).

To investigate further, we built a computer-controlled trigger circuit that takes the deflection signal, trigger request, and desired phase as inputs, and then triggers the digitizer and the excitation source at the given phase as described in Chapter 2.2 and Appendix A.[35] In our experiments, we varied the trigger phase from 0° to 360° and measured t_{FP} for different rise times. **Figure 2.5**(b) shows measured t_{FP}'s of a cantilever with f_0 = 272.218 kHz, k = 26.2 N/m, and Q = 432 at V_{bias} = 5V, for voltage pulses with V_{pp} = 5V at different values of τ at different phases. The data in **Figure 2.5**(b) support our argument that the phase of the cantilever oscillation at the excitation time has a significant effect on the results. Indeed, the chosen phase-delay can change the minimum detectable rise time by more than 10 folds. Both experiment and simulation suggest that a phase of 180° is the best phase for maximum slope in calibration curves, which corresponds to the ability to differentiate rise times with minimum error.

To understand the cause of the phase effect, we simulated our experiment with and without the electrostatic force term because we hypothesize that the t_{FP} encodes time-dependent information from both F_e and dF_e/dz.[19] In **Figure 2.6**, we show the results of these simulations. We simulated the same cantilever described above, with a voltage pulse that has a rise time of 100 ns, over all phases for two different cases: using only the force gradient and using both the electrostatic force and the force gradient. One can easily see that there is significant variation in t_{FP} and Δf when both terms are present (solid blue lines). However, when we remove the electrostatic force term and run the simulations again with only the force gradient term present, the effect of excitation phase on t_{FP} and Δf vanishes (dashed red lines in **Figure 2.6**). This result implies that the electrostatic force is responsible for the phase effects.

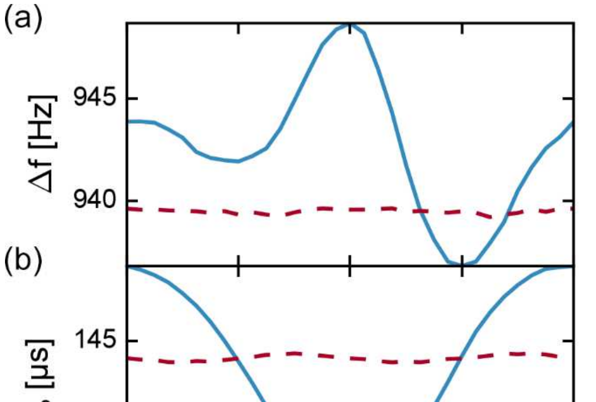

Figure 2.6. t_{FP} and frequency shift vs phase. Comparison of simulated **(a)** frequency shift at t_{FP} and **(b)** t_{FP}'s for different phases of cantilever deflection at excitation time, at τ=100 ns, showing that the electrostatic force is essential in explaining the observed cantilever behavior. Dashed red lines denote no force but force gradient; solid blue lines denote both force and force gradient being present.

The t_{FP} is at its minimum and Δf is maximum at 180° with respect to cantilever deflection only when the electrostatic force is included in our simulations. We speculate that this result is because, at a cantilever phase of 180°, the electrostatic force is in the same direction as the cantilever velocity (towards the surface) and opposite to the damping force. At 90° and 270°, the cantilever is at the maximum of its motion range and has no velocity. At 0°, the cantilever is moving away from the surface and at the center of its motion. Since t_{FP} is at its minimum and the frequency shift is maximum at 180°, it is also easier to detect the minimum of the instantaneous frequency because the convexity of the instantaneous frequency curve increases. Experimental and simulated instantaneous frequency curves can be found in Figure A.3 and Figure A.4.[35]

2.4.3 *Noise Considerations*

In an FM detection system, there are several noise sources such as detector noise, shot noise, *1/f* noise and thermal noise. In our system, acoustic noise and mechanical noise due to coupling of cantilever to the piezoacoustic drive element are also seen in the frequency spectra (see Figure A.5).[35]

While piezoacoustic excitation is the most commonly available drive mechanism, it relies on the physical connection between the drive piezo and the cantilever. The mechanical coupling of the cantilever to a larger mechanical system, such as the piezoacoustic element itself, can give rise to a complex resonance spectrum. In an FM detection scheme, this complex resonance spectrum can be problematic, since the resulting drive response is not flat with frequency,[34] and the region of interest is generally a small bandwidth around the resonance frequency. However, the cantilever now has a response function that is dependent on the insufficiently flat drive spectrum, in addition to sample properties. This effect results in frequency tracking instabilities.[52] In order to access a cleaner cantilever response, one can use an actuation method that does not mechanically couple to the cantilever, such as photothermal excitation.

Photothermal excitation is a new method for driving cantilevers, most often used in liquid environments for AC atomic force microscopy.[30–34] In photothermal excitation mode, a power-modulated laser is focused on the cantilever base to drive the cantilever oscillation, achieving a cleaner response function that is largely uncontaminated by spurious resonances. Furthermore, photothermal excitation can be used with frequency modulated AFM, where it has proven to be more accurate and stable.[33,34,53] The recovery of the cantilever's frequency shift and damping are easier due to the stability, accuracy and linearity of the transfer functions of the excitation and detection systems.[33] We thus anticipated that using photothermal excitation instead of

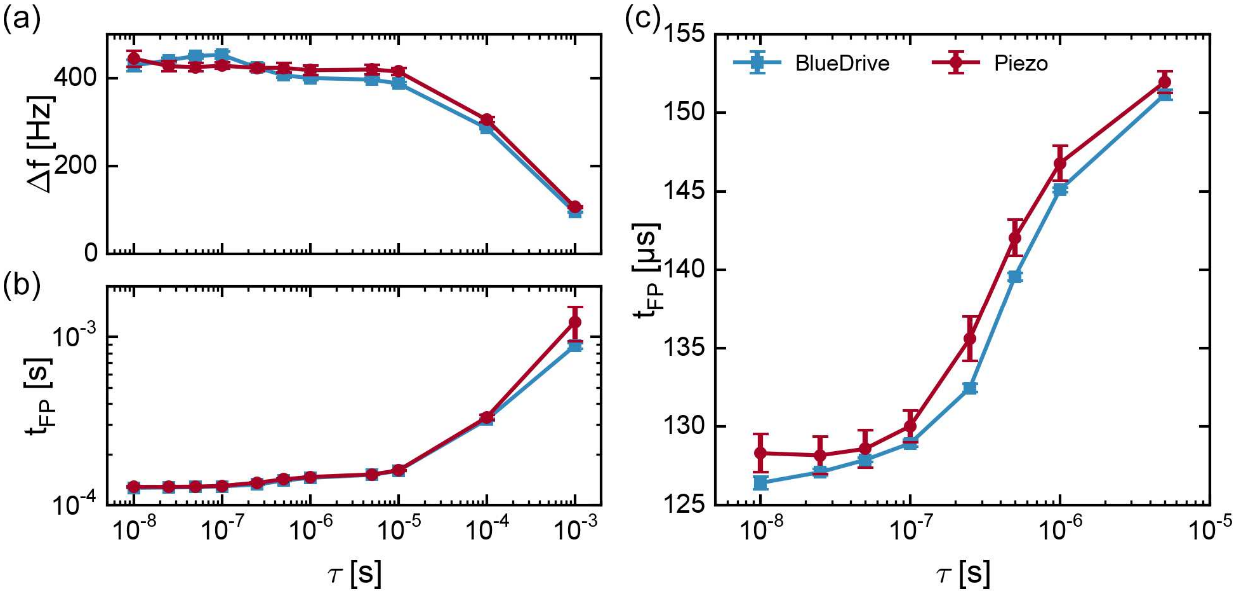

Figure 2.7. Comparison of piezo-driven versus photothermally-driven cantilevers showing experimental **(a)** frequency shifts and **(b)** t_{FP}'s for an AFM cantilever excited at 180°. While the cantilever response is nearly identical, the uncertainty induced by frequency noise is notably smaller for the same number of averaged pulses, as seen in **(c)** which shows a zoomed in region of the fastest decays. The cantilever parameters are $f_0 = 255.920$ kHz, $k = 17.9$ N/m and $Q = 428$. The μ_{tFP} and σ_{tFP} values are compiled from 30 different runs of the same experiment. Every run consists of 2000 averages of raw cantilever deflection signal.

piezoacoustic excitation should increase the stability of cantilever oscillation by providing a drive response that is flat with frequency.

In order to test the noise-reducing effect of photothermal excitation, we employed a commercially available system (Asylum Research's BlueDrive) in our experiments.[34] **Figure 2.7** shows experimental Δf vs. τ and t_{FP} vs. τ (calibration curve) data taken with BlueDrive and conventional piezoacoustic drive for comparison. In **Figure 2.7**(a), we see that frequency shifts for both drive types follow the same trend and lie in close proximity. The calibration curves are also quite similar in shape for both drive modes, as shown in **Figure 2.7**(b) and (c) (**Figure 2.7**(c) shows a zoomed in view at faster rise times). As we have predicted, the error bars, which are caused by the instability of the drive response, for the BlueDrive data are ~5X smaller at the fastest rise times. Having smaller error bars means that we get closer to having one-to-one mapping between t_{FP} and τ. Practically, this result means that for a given number of averages, when the cantilever is driven by piezoacoustic excitation, rise times faster than 100 ns are not distinguishable from each other due to the frequency noise. With BlueDrive, the lower frequency noise floor permits us to distinguish rise times down to 25 ns with a cantilever of f_0 = 255.920 kHz, k = 17.9 N/m and Q = 428; and we can distinguish rise times down to 10 ns with a cantilever of f_0 = 503.327 kHz, k = 72.7 N/m and Q = 499. We discuss the noise around the cantilever resonance frequency in more detail in Figure A.5.[35]

In any system operating at ambient temperatures, thermal noise (Brownian motion of the cantilever) is always the fundamental limiting factor of the achievable noise floor, while other noise resources can be mitigated by changes to hardware. Due to its Brownian nature, thermal noise can be modeled as additive white Gaussian noise (AWGN) and one of the easiest and well-known methods to remove it (at the expense of acquisition time) is to signal average. In the present case, we average the raw cantilever deflection signals for multiple excitation pulses before analysis. In **Figure 2.8**, we show different numbers of averages (offset upwards by 5 μs for clarity), where deflection signals were acquired at the same point and at cantilever phase of 180° driven by BlueDrive. As expected, increasing the number of averages reduces the uncertainty in t_{FP} without altering the trend of the calibration curves. When driven by BlueDrive and with 2000 averages per point, we are able to distinguish rise times down to 10 ns, which can be seen in the inset of **Figure 2.8.** Comparison of different numbers of averages showing that the increasing number of averages decrease the uncertainty of t_{FP} vs. τ curves (taken using photothermal excitation). The curves are offset upwards 5 μs for clarity. Inset shows the zoom in for 2000 averages (same experimental parameters as in Figure 2.7).. In this case, 10 ns corresponds to 0.5% of a cycle.

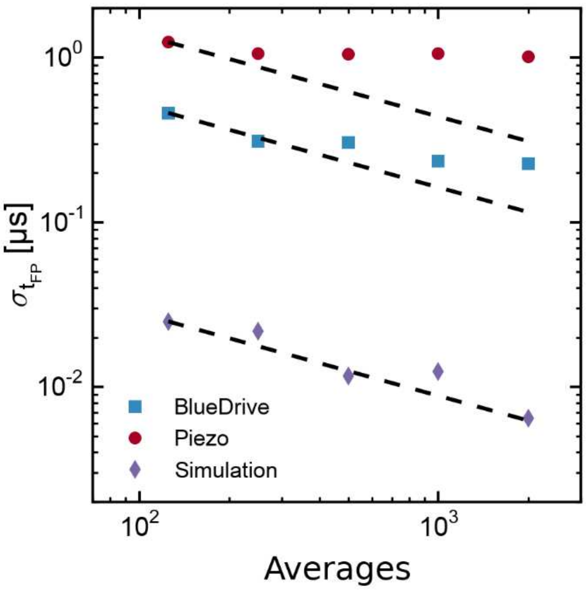

Figure 2.8. Comparison of standard deviations for different number of averages for BlueDrive, piezoacoustic excitation and simulations, where noise is calculated using fluctuation-dissipation theorem and added as AWGN, at τ=100 ns, showing that the main contribution to noise is not thermal. Dashed lines indicate $\sigma \sim n^{-1/2}$. The cantilever parameters are f_0 = 255.920 kHz, k = 17.9 N/m and Q = 428.

In **Figure 2.9**, we present standard deviations for experimental t_{FP}'s from 30 different runs of the same cantilever for BlueDrive and piezoacoustic excitation at 100 ns rise time, as well as simulated thermal noise, where dashed lines denote $1/\sqrt{n}$ law for averaging. The standard deviations for experiments acquired with piezoacoustic excitation and BlueDrive start decreasing at first with averaging, however the gains begin to level off rapidly. We take this deviation from the expected $1/\sqrt{n}$ trend as indicating other noise sources related to the instrument, since the variation due to thermal noise is expected to follow $1/\sqrt{n}$.[46] The BlueDrive data benefit more from signal averaging, only to a certain extent. We conclude that with increasing number of averages both BlueDrive and piezoacoustic excitation modes become limited by non-thermal noise sources such as detector noise. On the other hand, our simulated results, where we added AWGN calculated by the fluctuation-dissipation theorem to the simulated cantilever deflection, clearly follow the expected $1/\sqrt{n}$ behavior, and show a lower overall noise floor. For any given number of averages, photothermal excitation has approximately 5 times less variation in t_{FP} compared to piezoacoustic excitation, and simulated thermal noise has approximately 10 times less variation in t_{FP} compared to photothermal excitation. This result indicates that, while the work presented here represents a greater than five-fold improvement over previous results, there is still significant room to improve the performance of the trEFM method in the future.

2.4.4 *Cantilever Parameters*

We investigated how different approaches work for removing different types of noise, namely frequency and thermal noise, and what we can achieve in terms of time resolution using these methods. Additionally, selection of other experimental parameters, such as the cantilever, affects how the system performs. Unfortunately, it is impossible to scan such an immense parameter space experimentally. Therefore, we combine experimental data with modeled data to understand better how the selection of cantilever parameters affects our results. Here, we consider the effects of resonance frequency (f_0), spring constant (k) and the quality factor (Q). The resonance frequency and the spring constant of a cantilever depend on the cantilever geometry and materials that are used. The quality factor of the cantilever is determined in part by the environment; for example, moving from a liquid environment to ultra-high vacuum would increase the quality factor by 4-5 orders of magnitude.[33,46,54] Here, we look into effects of these parameters on time resolution in fast trEFM.

In order to test the frequency dependence of calibration curves, we performed experiments and simulations with four different types of commercial cantilevers, with resonance frequencies 60.219 kHz, 154.806 kHz, 255.920 kHz, and 503.327 kHz. In **Figure 2.10**, we can clearly see that the slowest cantilever (60 kHz) has the shallowest slope, where the calibration curve is almost completely flat for time scales shorter than 1 μs. Cantilevers with resonance frequencies 154 kHz and 255 kHz have similar behavior; however, the calibration curve for 154 kHz flattens after 100 ns. The fastest cantilever (503 kHz) has the minimum distinguishable rise time of 10 ns, whereas the cantilever with resonance frequency of 255 kHz can resolve down to 25 ns. Although the calibration curve of the 255 kHz cantilever looks similar to the fastest cantilever's, the standard deviations for the 255 kHz cantilever are larger than the 503 kHz cantilever's (see Figure A.6).[35] Thereby, the 255 kHz cantilever has a higher minimum distinguishable rise time. Cantilevers with resonance frequencies of 60 kHz and 155 kHz have minimum distinguishable rise times of 1 μs

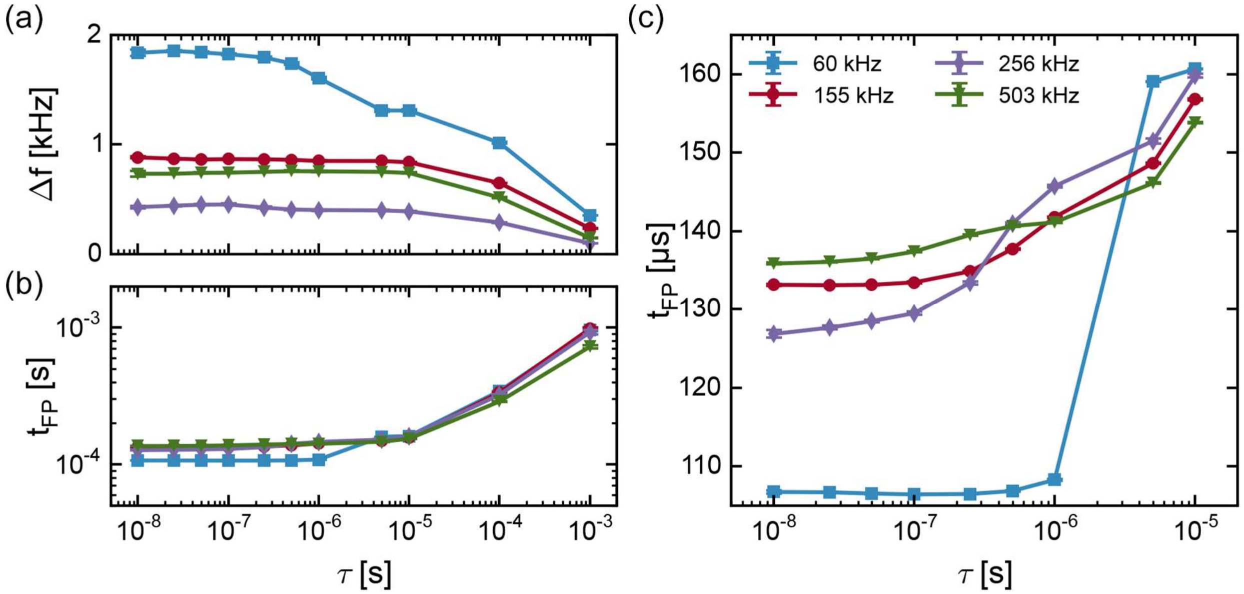

Figure 2.9. Effect of different resonance frequencies on **(a)** frequency shifts, **(b)** t_{FP} measurements. While the cantilevers' responses are similar for longer rise times, faster cantilevers have higher curvatures for short times as seen in **(c)**, which shows a zoomed in region for faster decays. The cantilever parameters are $f_0 = 60.219$ kHz, $k = 1.37$ N/m, $Q = 150$; $f_0 = 154.806$ kHz, $k = 15.8$ N/m and $Q = 352$; $f_0 = 255.920$ kHz, $k = 17.9$ N/m and $Q = 428$; and $f_0 = 503.327$ kHz, k = 72.7 N/m and Q = 499. AFM cantilevers were excited at 180° using BlueDrive. The μ_{tFP} and σ_{tFP} values are compiled from 30 different runs of the same experiment. Every run consists of 2000 averages of raw cantilever deflection signal.

and 100 ns, respectively. These results and Eq. 2.10 imply that all things being equal, higher frequency cantilevers are more sensitive to the force and the force gradient.

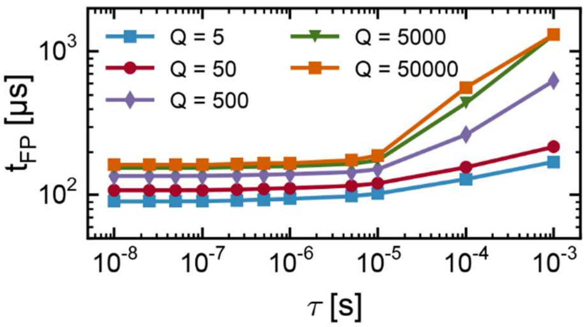

Figure 2.10. Effect of varying Q on simulated calibration curves showing the beneficial effect of higher Q for longer time constants, and the lesser effect of Q at fast times. Simulation parameters: f_0 = 503.327 kHz, k = 72.7 N/m and Q varies.

We also consider the effects of Q, as we expect Q to have an effect on calibration curves: looking at Eq. 2.10 (which considers only the effects of a force gradient) one would expect the minimum detectable force gradient to decrease (increasing sensitivity) with increasing Q.[46] We simulate this effect in **Figure 2.11**, where one can clearly see the effect of *Q* on the calibration curve with relaxation times (τ_R) ranging from 20 µs to 0.2 seconds. Having a high Q cantilever increases the slope of the calibration curve for rise times longer than 10 µs, where it becomes comparable to τ_R; *however, it does not affect the calibration curve for shorter rise times as much, where it is much less than* τ_R. This result is consistent with Eq. 2.10 at long times, but not at short times. We propose that this discrepancy, which we have confirmed by both simulation and experiment, arises from the fact that the electrostatic force and its gradient both contribute to the t_{FP} signal at shorter rise times. In summary, having higher Q has a favorable effect on the detection of slower events (τ > cantilever period), while the effect of Q is more complicated and less important at faster times.

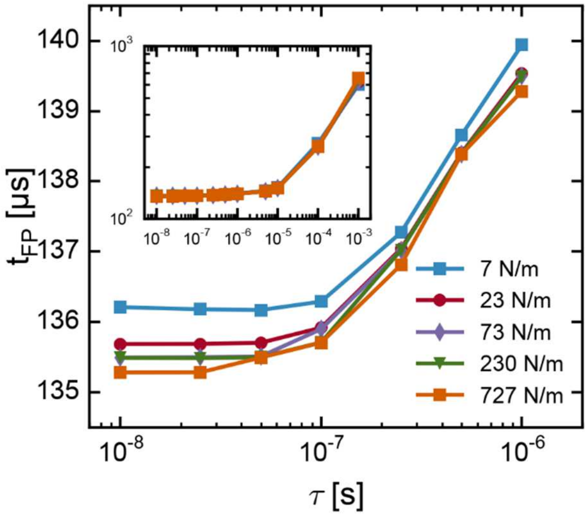

Figure 2.11. Effect of varying k on simulated calibration curves showing a small positive effect of higher k for shorter time constants, and no effect of k at slow times. Simulation parameters: f_0 = 503.327 kHz, Q = 499 and k varies.

We next examine the effect of spring constant. Based on the force gradient alone, one would expect that increasing the spring constant should increase the minimum detectable force gradient (Eq. 2.10).[46] On the other hand, we find this expectation only holds for a model where there are no external forces other than the driving force, or where the effects of external forces are small compared to the frequency shift due to the force gradient. Thus, the effect of spring constant on the detection of rise times is not as clear as the effect of Q. When we include the electrostatic force term in our simulations, we do not observe a substantial change in the slope of the calibration curve for slower rise times while the spring constant is changing as seen in inset of **Figure 2.12**. However, contrary to the previous literature, **Figure 2.12** shows that as the cantilever gets stiffer, the curvature of the calibration curve slightly increases for faster rise times (<1 µs) with the inclusion of the force term; and higher curvature makes distinguishing adjacent τ's easier to some extent. Furthermore, stiffer cantilevers have lower levels of thermal noise.[55] As a result, we expect stiffer cantilevers to perform slightly better in detection of rise times that are shorter than a cantilever period, and to have negligible effects on detection of longer rise times.

In summary, Figures 2.10, 2.11 and 2.12 show that a combination of faster cantilever resonance frequency, larger spring constant, and higher Q will tend to improve the time resolution in fast trEFM. There is a large range of spring constants that is commercially available, and Q is contingent upon the environment. In addition, we tested the effects of other experimental parameters, such as lift height and voltage bias between the tip and the sample, and found that the frequency shift follows Eq. 2.4. as expected (Figure A.7 and Figure A.8),[35] while there is no substantial change in calibration curves. In other words, cantilever parameters are the primary experimental parameters, other than the number of averages and the cantilever excitation method, that affect the time-resolution in fast trEFM.

2.5 Imaging

We have implemented trEFM as an imaging technique that can acquire and analyze data concurrently. The trEFM software suite consists of two parts: measurement and analysis. The measurement part is coded in Igor Pro (Wavemetrics, Inc.) using Asylum Research's software and uses the GaGe Software Development Kit to interface with the digitizer hardware in C++; the analysis is coded in Python using NumPy/SciPy.[56,57] Using application-programming interfaces, we are able to transfer the digitized deflection signal to the analysis program and send the results back to be interpreted by the user. During imaging, the digitized deflection signals for each line of pixels are processed upon acquisition. Signals for each line are passed along to the analysis software with the number of pixels contained in a line, where the instantaneous frequency is extracted and returned to the user. The duration of this operation is dependent upon the number of averages and the number of pixels specified for binning, as well as the duration of each signal acquisition. To expedite acquisition at the expense of concurrent imaging, it is possible to acquire

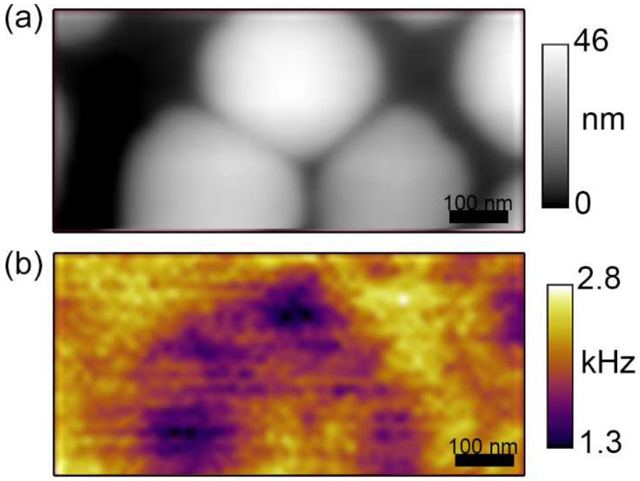

Figure 2.12. A fast trEFM image: **(a)** Topography and **(b)** inverse t_{FP} (t_{FP}^{-1}) images of a 1:4 ratio MDMO-PPV:PCBM thin film photovoltaic device cast from toluene. Excitation wavelength is 488 nm and intensity at the tip is ~100-500 W/cm^2. Data are acquired at 10 nm lift height, 10 V bias between the cantilever and the sample, with 60 averages per pixel.

image data and post-process that into an image on a separate machine. We have made the software suite freely available online.[58]

Currently, we are able to take a 64x32 image in approximately an hour with 60 averages per pixel. **Figure 2.13** shows a fast trEFM image of a model organic photovoltaic blend, (poly[2-methoxy-5-(3′,7′-dimethyloctyloxy)-1,4-phenylenevinylene]:[6,6]-phenyl-C61-butyric acid methyl ester) (MDMO-PPV:PCBM). Here, we used a modulated laser (488 nm) to photoexcite the material, similarly to what we have done in previous reports, where we used modulated LEDs.[18–22] This blend's film morphology can be easily adjusted by changing the solvent,[59] and it has large domains that can be easily distinguished and thus makes it a useful testbed for trEFM. The structure of MDMO-PPV:PCBM is well-known and the data here qualitatively agree with previous trEFM work.[20] Areas of low (high) $1/t_{FP}$ values correspond to low (high) external quantum efficiency regions in the film.[19] This image clearly shows that variation in t_{FP} on the nanoscale can be directly measured using the trEFM technique.

2.6 Conclusions

trEFM offers high time resolution with high spatial resolution as a supplement to bulk measurements of electronic and photonic properties of materials. In our experiments and simulations, we investigated the effect of the electrostatic force in detection of fast time transients. We found that the electrostatic force and the phase of cantilever motion during which the force is applied both have an effect on the ability to resolve rise times shorter than a period of the cantilever. Importantly, by controlling the cantilever phase at the perturbation time in order to align the electrostatic force with the cantilever while it is at the midpoint of its motion moving downward, we can increase the time resolution of fast trEFM as well as making measurements more reliable.

Using photothermal excitation instead of piezoacoustic excitation, which reduces the measurement noise by increasing the stability of the drive, and increasing the number of averaged signals to decrease the thermal noise, we are able to differentiate rise times down to 10 ns. We anticipate these results will lead to continued improvements in the future by using stiffer and faster cantilevers with high quality factors. We expect that trEFM will find applications beyond the development and characterization of organic photovoltaics with its improved time resolution, such as perovskite solar cell development, battery electrode characterization, and biological measurements.

2.7 References

[1] M.J. Jaquith, E.M. Muller, and J.A. Marohn, J. Phys. Chem. B **111**, 7711 (2007).
[2] M.J. Jaquith, J.E. Anthony, and J.A. Marohn, J. Mater. Chem. **19**, 6116 (2009).
[3] J.L. Luria, K.A. Schwarz, M.J. Jaquith, R.G. Hennig, and J.A. Marohn, Adv. Mater. **23**, 624 (2011).
[4] L.M. Smieska, V.A. Pozdin, J.L. Luria, R.G. Hennig, M.A. Hines, C.A. Lewis, and J.A. Marohn, Adv. Funct. Mater. **22**, 5096 (2012).
[5] T. Burnett, R. Yakimova, and O. Kazakova, Nano Lett. **11**, 2324 (2011).
[6] N. Hoepker, S. Lekkala, R.F. Loring, and J.A. Marohn, J. Phys. Chem. B **115**, 14493 (2011).

[7] E. Castellano-Hernández, J. Moreno-Llorena, J.J. Sáenz, and G.M. Sacha, J. Phys. Condens. Matter **24**, 155303 (2012).
[8] A. Schirmeisen, A. Taskiran, H. Fuchs, H. Bracht, S. Murugavel, and B. Roling, Phys. Rev. Lett. **98**, 225901 (2007).
[9] A. Taskiran, A. Schirmeisen, H. Fuchs, H. Bracht, and B. Roling, Phys. Chem. Chem. Phys. **11**, 5499 (2009).
[10] W. Schade, J. Preusser, D.L. Osborn, Y.Y. Lee, J. DeGouw, and S.R. Leone, Opt. Commun. **162**, 200 (1999).
[11] B.A. Nechay, U. Siegner, M. Achermann, H. Bielefeldt, and U. Keller, Rev. Sci. Instrum. **70**, 2758 (1999).
[12] S. Weiss, D.F. Ogletree, D. Botkin, M. Salmeron, and D.S. Chemla, Appl. Phys. Lett. **63**, 2567 (1993).
[13] Y. Terada, S. Yoshida, O. Takeuchi, and H. Shigekawa, Nat. Photonics **4**, 869 (2010).
[14] J.R. O'Dea, L.M. Brown, N. Hoepker, J.A. Marohn, and S. Sadewasser, MRS Bull. **37**, 642 (2012).
[15] M. Pfannmöller, W. Kowalsky, and R.R. Schröder, Energy Environ. Sci. **6**, 2871 (2013).
[16] N. Balke, D. Bonnell, D.S. Ginger, and M. Kemerink, MRS Bull. **37**, 633 (2012).
[17] D. a. Bonnell, D.N. Basov, M. Bode, U. Diebold, S. V. Kalinin, V. Madhavan, L. Novotny, M. Salmeron, U.D. Schwarz, and P.S. Weiss, Rev. Mod. Phys. **84**, 1343 (2012).
[18] D.C. Coffey and D.S. Ginger, Nat. Mater. **5**, 735 (2006).
[19] R. Giridharagopal, G.E. Rayermann, G. Shao, D.T. Moore, O.G. Reid, A.F. Tillack, D.J. Masiello, and D.S. Ginger, Nano Lett. **12**, 893 (2012).
[20] P.A. Cox, M.S. Glaz, J.S. Harrison, S.R. Peurifoy, D.C. Coffey, and D.S. Ginger, J. Phys. Chem. Lett. **6**, 2852 (2015).
[21] O.G. Reid, G.E. Rayermann, D.C. Coffey, and D.S. Ginger, J. Phys. Chem. C **114**, 20672 (2010).
[22] G. Shao, G.E. Rayermann, E.M. Smith, and D.S. Ginger, J. Phys. Chem. B **117**, 4654 (2013).
[23] S.D. Stranks, G.E. Eperon, G. Grancini, C. Menelaou, M.J.P. Alcocer, T. Leijtens, L.M. Herz, A. Petrozza, and H.J. Snaith, Science **342**, 341 (2013).
[24] D.W. de Quilettes, S.M. Vorpahl, S.D. Stranks, H. Nagaoka, G.E. Eperon, M.E. Ziffer, H.J. Snaith, and D.S. Ginger, Science **348**, 683 (2015).
[25] B.R. Lee, E.D. Jung, J.S. Park, Y.S. Nam, S.H. Min, B.-S. Kim, K.-M. Lee, J.-R. Jeong, R.H. Friend, J.-S. Kim, S.O. Kim, and M.H. Song, Nat. Commun. **5**, 4840 (2014).
[26] Y. Tamai, H. Ohkita, H. Benten, and S. Ito, J. Phys. Chem. Lett. **6**, 3417 (2015).
[27] R.B. Gennis, *Biomembranes* (Springer New York, New York, NY, 1989).
[28] P. Greengard, Science **294**, 1024 (2001).
[29] R.E. Blankenship, Govindjee, G.A. Berkowitz, A.R. Portis, Jr., and R.J. Shopes, McGraw-Hill Educ. (2014).
[30] N. Umeda, S. Ishizaki, and H. Uwai, J. Vac. Sci. Technol. B Microelectron. Nanom. Struct. **9**, 1318 (1991).
[31] G.C. Ratcliff, D.A. Erie, and R. Superfine, Appl. Phys. Lett. **72**, 1911 (1998).
[32] H. Yamashita, N. Kodera, A. Miyagi, T. Uchihashi, D. Yamamoto, and T. Ando, Rev. Sci. Instrum. **78**, 083702 (2007).
[33] A. Labuda, K. Kobayashi, D. Kiracofe, K. Suzuki, P.H. Grütter, and H. Yamada, AIP Adv. **1**, 022136 (2011).

[34] A. Labuda, J. Cleveland, N. Geisse, M. Kocun, B. Ohler, R. Proksch, M. Viani, and D. Walters, Microsc. Anal. **28**, 23 (2014).
[35] See Appendix A.
[36] P. Girard, M. Ramonda, and D. Saluel, J. Vac. Sci. Technol. B Microelectron. Nanom. Struct. **20**, 1348 (2002).
[37] L. Portes, P. Girard, R. Arinero, and M. Ramonda, Rev. Sci. Instrum. **77**, 096101 (2006).
[38] L. Portes, M. Ramonda, R. Arinero, and P. Girard, Ultramicroscopy **107**, 1027 (2007).
[39] D.S. Ginger, R. Giridharagopal, D.T. Moore, G.E. Rayermann, and O.G. Reid, U.S. patent 8,686,358 (2014).
[40] S.M. Yazdanian, J.A. Marohn, and R.F. Loring, J. Chem. Phys. **128**, 224706 (2008).
[41] B. Boashash, Proc. IEEE **80**, 520 (1992).
[42] R.B. Blackman and J.W. Tukey, Bell Syst. Tech. J. **37**, 185 (1958).
[43] A. V Oppenheim and R.W. Schafer, *Discrete-Time Signal Processing*, 3rd ed. (Prentice Hall, Upper Saddle River, NJ, 2010).
[44] B.C. O'Regan, K. Bakker, J. Kroeze, H. Smit, P. Sommeling, and J.R. Durrant, J. Phys. Chem. B **110**, 17155 (2006).
[45] C.G. Shuttle, B.C. O'Regan, A.M. Ballantyne, J. Nelson, D.D.C. Bradley, J. de Mello, and J.R. Durrant, Appl. Phys. Lett. **92**, 093311 (2008).
[46] T.R. Albrecht, P.H. Grütter, D. Horne, and D. Rugar, J. Appl. Phys. **69**, 668 (1991).
[47] W.R. Silveira, E.M. Muller, T.N. Ng, D. Dunlap, and J.A. Marohn, in *Scanning Probe Microscopy*, edited by S. Kalinin and A. Gruverman (Springer New York, New York, NY, 2007), pp. 788–830.
[48] W. Denk and D.W. Pohl, Appl. Phys. Lett. **59**, 2171 (1991).
[49] P.A. Cox, D.A. Waldow, T.J. Dupper, S. Jesse, and D.S. Ginger, ACS Nano **7**, 10405 (2013).
[50] G.M. McClelland, R. Erlandsson, and S. Chiang, in *Review of Progress in Quantitative Nondestructive Evaluation* (Springer US, Boston, MA, 1987), pp. 1307–1314.
[51] Y. Martin, C.C. Williams, and H.K. Wickramasinghe, J. Appl. Phys. **61**, 4723 (1987).
[52] A. Labuda, Y. Miyahara, L. Cockins, and P.H. Grütter, Phys. Rev. B **84**, 125433 (2011).
[53] L. Collins, S. Jesse, N. Balke, B.J. Rodriguez, S. Kalinin, and Q. Li, Appl. Phys. Lett. **106**, 104102 (2015).
[54] E. Inami and Y. Sugimoto, Phys. Rev. Lett. **114**, 246102 (2015).
[55] D. Platz, D. Forchheimer, E.A. Tholén, and D.B. Haviland, Nat. Commun. **4**, 1360 (2013).
[56] T.E. Oliphant, Comput. Sci. Eng. **9**, 10 (2007).
[57] S. van der Walt, S.C. Colbert, and G. Varoquaux, Comput. Sci. Eng. **13**, 22 (2011).
[58] D.U. Karatay, J.S. Harrison, and R. Giridharagopal, http://bitbucket.org/gingerlab/ffta
[59] H. Hoppe and N.S. Sariciftci, J. Mater. Chem. **16**, 45 (2006).

Chapter 3. Classifying Force Spectroscopy of DNA Pulling Measurements

3.1 Introduction[b]

Dynamic force spectroscopy (DFS) is an important method for understanding the kinetics and thermodynamics of bond rupture at the level of individual molecules that involves single-molecule pulling measurements using an atomic force microscope[1–5] or optical tweezers.[6–8] These methods are capable of measuring unbinding events occurring at the piconewton scale, but such experiments typically involve the acquisition and analysis of thousands of force-distance curves to produce reliable statistics.[9–14] Because non-specific binding events and other unsuccessful pulls can also occur, the force spectra of the specific bond-ruptures that represent the desired signal are often contaminated with unwanted data that must be sorted and filtered prior to analysis.[12] Sometimes, specific "force tags" with easily recognized force-distance spectra are included to help the experimenter isolate successful pulls, but these methods are often chemically tedious. Additionally, they still impose the requirement that experimenter manually identifies and classifies each curve as being a successful pull or not, or else construct specific software filters which may impose selection bias on the experiment.[12,13,15]

Over the last few decades, machine learning has changed substantially and become accessible to many scientists outside of the area of computer science. The penetration of new statistical analysis and data mining approaches into physical sciences[16,17] and life sciences[18,19] has been revolutionary in terms of the amount of data analyzed and the information extracted. These

---

[b] This chapter is adapted from: D. U. Karatay, J. Zhang, J. S. Harrison, D. S. Ginger, Classifying Force Spectroscopy of DNA Pulling Measurements Using Supervised and Unsupervised Machine Learning Methods. Submitted to Journal of Chemical Information and Modeling.

approaches can also be employed in automating data analysis tasks in research,[20–22], predicting novel features,[23–25] and optimization of experiments.[26,27] Recently, ensemble learning methods, such as bagging,[28] AdaBoost[29] and random forests[30], have become ubiquitous in supervised pattern recognition problems as they can obtain a high prediction accuracy. In particular, the random forest algorithm can provide information on the importance of different variables for classification. It is also straightforward to implement and understand, since the underlying mechanism is the well-known decision tree algorithm.

Here, we develop supervised and unsupervised models for classification of DFS experiments involving the shearing of double-stranded DNA. We take the unique approach of utilizing azobenzene-modified DNA sequences which show different binding properties before and after exposure to UV light. This property is beneficial for benchmarking classification algorithms, as it allows us to compare the changes in the classification of the force spectra before and after illumination with UV light. We show that machine-learning algorithms are capable of achieving the same level of accuracy as a trained human researcher and are thus a promising means to facilitate analysis of DFS experiments.

3.2 Materials and Methods

3.2.1 *Preparation of DNA Solution*

Di-thiol protected azobenzene-modified DNA and unmodified complementary DNA were purchased from Integrated DNA Technology (IDT Inc., IA). The sequences of azobenzene-modified DNA and complementary DNA are 5'SH(T)$_{30}$GACTGCAATCAAGTCTACC3' and 5'CGTTAGTTCAGXATXGGTCAG(T)$_{30}$SH3’, respectively. X denotes azobenzene molecule. 10 μM azobenzene-modified/unmodified DNAs were deprotected with 10 mM DTT in phosphate buffer for 18 min. The free thiol-terminated DNAs were extracted from the phosphate buffer via a de-salting step with micro-chromatography columns (Micro Bio-Spin® 6 Columns, Bio-Rad), and 2 μM DNA was immediately dissolved into aqueous solution containing 1 mM phosphate buffer saline (PBS), 0.3 M sodium chloride and 3 mM sodium azide. All solutions were filtered before preparing DNA solution.

3.2.2 *Tip and Substrate Modification*

Au-coated Biolever cantilevers (BL-RC-150VB Olympus) with spring constant of ~0.006 N/m were used in the force-pulling experiments. The tips were rinsed with acetone and ethanol, sequentially, and gently blown dry with nitrogen. Then, the tips were cleaned with oxygen plasma for 1 min. The fresh Au films on glass (Cr/Au = 2/6 nm) were prepared with thermal evaporator at a deposition rate of ~ 0.05 nm/s. After these steps the tip and substrate modification were processed in parallel. 40 μL unmodified/azobenzene-modified DNA solution (2 μM) was dropped onto the tip/substrate. This step was kept for 2 hours to functionalize tip/substrate with DNAs. After carefully rinsing tip/substrate with 1 mM PBS (0.05% SDS) and DI water, 40 μL sodium 3-mercapto-1-propanesulfonate solution (10 μM), containing 1 mM phosphate buffer saline (PBS), 0.3 M sodium chloride and 3 mM sodium azide, was backfilled onto tip/substrate and kept for 2 hours to passivate the unfunctionalized gold surface of the tip/substrate. The tip/substrate was rinsed with 1 mM PBS (0.05% SDS) and DI water again and then kept in 40 μL buffer solution (1 mM PBS, 0.3 M NaCl and 3 mM NaN3) before use.

3.2.3 *Dynamic Force Spectroscopy*

Force spectroscopy measurements were performed with an MFP-3D AFM (Asylum Research) in a liquid cell filled with buffer solution at room temperature. The force-distance curves were recorded at an approach/retract velocity of 20, 50, 200, 500, 1000 and 2000 nm/s, respectively. A

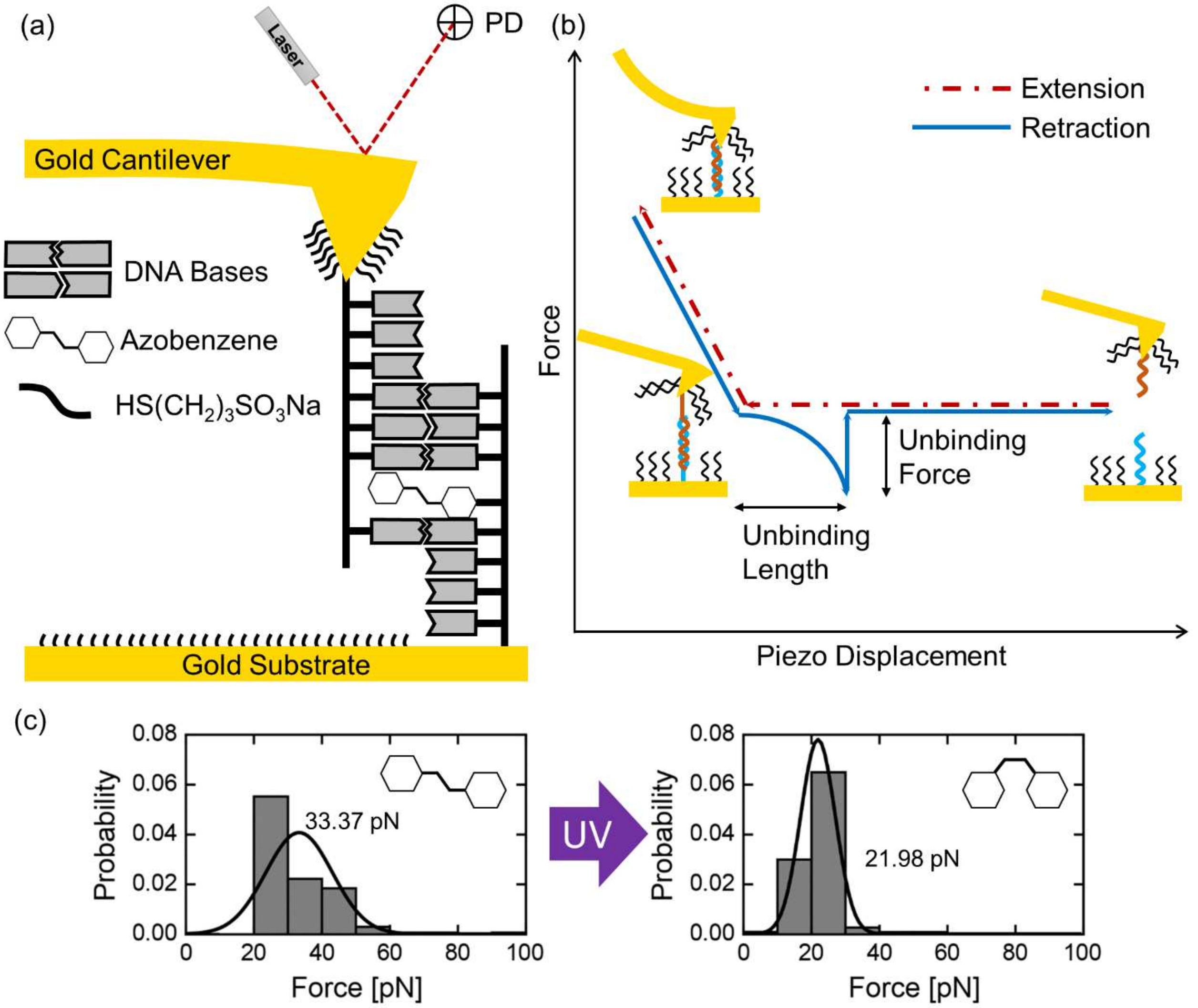

Figure 3.1. Schematics of force spectroscopy of DNA pulling experiments: **(a)** Schematic of DNA pulling experiments: the gold coated Si_3N_4 tip, functionalized with complementary DNA, pulls the double-strand azobenzene-modified DNA. **(b)** Schematic diagram of a typical force-distance curve for a successful pull. The cantilever approaches surface and two DNA strands bind together. The cantilever retracts from the gold film when force reaches the force trigger and then applies force to unbind the double-strand, resulting in unbinding. **(c)** After exposure to UV light the *cis* form azobenzene destabilizes the DNA binding, leading to a significant reduction in binding strength providing a control signal for testing classification algorithms.

one-second dwell time was kept in high velocity (> 50 nm/s) to ensure the bonding between DNAs on tip and substrate. The force distance and force trigger were set to 200 nm and 200 pN, respectively. At least 200 force curves were collected at each loading rate. The trans-azobenzene DNA was isomerized to cis-azobenzene DNA by irradiating the sample with UV light with wavelength of 365 nm (Thorlab M36L2-C3 UV collimated LED, 700 mA). The force curve collection started with trans-azobenzene DNA. After 2 hours of UV illumination to ensure the steady state was reached and the force curve collection was repeated. A schematic for the experiment can be seen in Figure 3.1(a); and Figure 3.1(b) describes a successful pull with a single event. In all of our dataset, we use the retraction curve and refer to it as force curve.

3.2.4 *Dataset*

All of the acquired force curves were labeled as belonging to one of 5 classes based on previous literature.[12] Typical force curves for the classes are shown in Figure 3.2. The first three of these classes, which are labeled as Class 0 – 3, represent unsuccessful pulling events and are labeled as such for binary classification. Class 0 is a pulling curve where there is no interaction recorded. Class 1 exhibits a single non-specific interaction between the tip and the sample. Class 2 has an unusual non-specific event(s) that we cannot label as Class 1. The last two classes are successful classes which are grouped together for binary classification. Class 3 is a single specific unbinding event, and Class 4 exhibits more than one event, at least one of them being successful. In addition to class labels, every acquired force curve is described by two experimental properties: loading speed and illumination condition. A distribution of all these labels is given in Table B.1 and Table B.2.

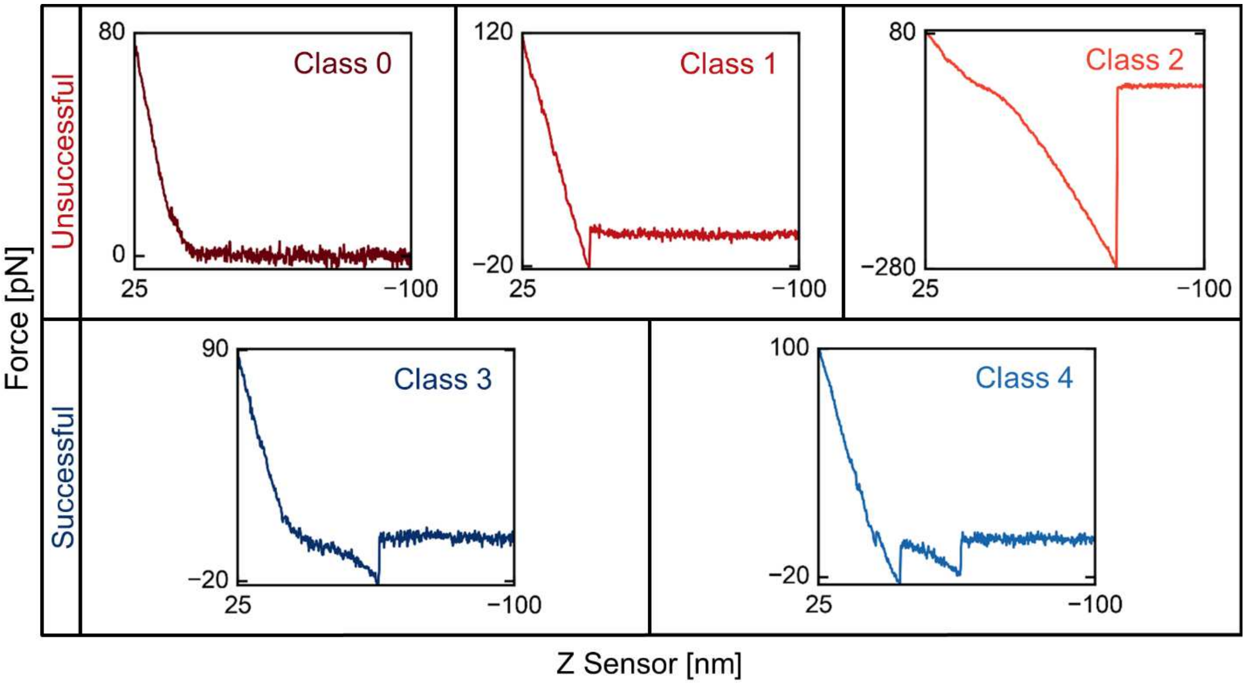

Figure 3.2. Typical force-distance curves of 5 classes for DNA pulling measurements. Class 0 has no event; class 1 is a non-specific interaction between the AFM tip and the substrate; and class 2 has an unusually non-specific event. Thus, they are unsuccessful pulls. Class 3 and 4 are successful pulls, where class 4 has multiple events. Note that x-axis does not denote the tip-surface separation, but the position of Z-sensor.

The experimentally acquired force curves are classified by researchers into one of the five classes. Since there can be ambiguity between some classes, experimenters may disagree on labels. Thus, we collected labels from three different human researchers to construct a ground truth for the dataset which we used for subsequent training and testing. These 2400 force curves were randomly split into a training set (50%) and a test set (50%) while maintaining a balance of successful and unsuccessful pulls as well as loading speeds and the illumination condition in each subset in order to reduce the variance between these two datasets. Following the described procedure, changing the way the data was split did not change the results we obtained.

3.2.5 *Force Curve Features*

In order to model our feature set, we relied on the experience of researchers who have worked to classify these curves in the past. This experience predicted that the most important variables would be the maximum force and the peak count in a pulling curve. Based on our own experience, we selected six different features: maximum force, peak count, energy (the area underneath the baseline), standard deviation under baseline, slope and what we will refer to as detrended standard deviation. Maximum force and peak count are self-explanatory features. The energy is the total area underneath the baseline which we calculate by using the mean of the last 40 points of a force curve. We calculate the standard deviation of the force-distance curve under the baseline. The slope is the basic slope of the line that connects the starting point ($z = 25\ nm$) to the last peak of the pulling curve. We calculated the detrended standard deviation by subtracting off the slope in the region between the starting point and the last peak using the basic slope; this is essentially the variation around the sloping region of the force curve.

3.2.6 *Model Selection*

For model and parameter selection, we used a 10-fold stratified cross-validation procedure to randomly split the training dataset 10 times into a training set (90%) and a validation set (10%). We employed this procedure for model selection and parameter selection of both binary and multiclass classifiers.[31]

We assess the predictive power of cross-validated models using the following statistical parameters:[32,33]

$$Accuracy = \frac{tp + tn}{tp + fp + tn + fn} \tag{3.1}$$

$$Precision = \frac{tp}{tp + fp} \tag{3.2}$$

$$Recall = \frac{tp}{tp + fn} \tag{3.3}$$

$$F_1\ score = 2\ \frac{Precision\ \cdot Recall}{Precision + Recall} \tag{3.4}$$

where *tp* are true positives (successful pulls predicted successful), *fp* are false positives (unsuccessful pulls predicted successful), *tn* are true negatives (unsuccessful pulls predicted unsuccessful), and *fn* are false negatives (successful pulls predicted unsuccessful). Precision measures the class agreement of the true labels with predicted successful labels, and recall measures the effectiveness of classifiers to identify successful labels. The F_1 score is the harmonic mean of precision and recall. We report the accuracy and F_1 score for all models that we evaluated. We use logarithmic loss (log-loss) as the figure of merit to evaluate our model and parameter selections, as it takes model bias and variance into account at the same time. The log-loss is calculated as the cross-entropy between the predictions and the distribution of the true labels which is a soft measurement of accuracy defined as follows for binary classification:[33]

$$Log\ loss = -\frac{1}{N}\sum_{i=0}^{N}(y_i \log(p_i) + (1 - y_i)\log(1 - p_i)), \tag{3.5}$$

where N is the number of samples, y_i is the true label (0 or 1) and p_i is the predicted probability that $y_i = 1$. The measures described above are also extended to multiclass classification tasks.[32] For multiclass classification we report the macro F_1 score[32] which calculates the F_1 score of each label separately and finds their unweighted mean. It does not take label imbalance into account.[32]

3.2.7 *Decision Tree Model*

We trained decision tree[34] models using all the features described above on the training set while varying these three parameters:

1. the maximum number of features to consider when looking for the best split (2 to 6 features),
2. the minimum number of samples required to split an internal node (1 to 2 samples),
3. the criterion for splitting (information gain[33] or Gini impurity[34]).

For each parameter combination, we applied the cross-validation and assessed the performance with given metrics. We selected the parameter combination that resulted in a minimum log-loss value as the best model. Then, we used the best parameter combination to create 50 decision tree models with different random initializations that were trained on the full training dataset. We used these decision tree models on the test dataset to get a statistical distribution of the accuracy. We used Scikit-learn package[35] to build decision tree models.

3.2.8 *Random Forest Model*

Random forest[30] models were trained similarly to decision tree models. Additionally, we varied the number of trees in the random forest models among 10, 100, and 1000 for parameter selection. We evaluated the performance of the random forest models the same way we evaluated the performance of the decision tree models. We used the Scikit-learn implementation of the random forest algorithm,[35] which differs from the literature by averaging the trees' probabilistic predictions instead of taking a vote from each tree.

3.2.9 *Unsupervised Classification Model*

Our unsupervised classification model is composed of Principal Component Analysis (PCA) for dimensionality reduction (generating feature set) and a Gaussian Mixture Model (GMM) for clustering. For this model we did not split our dataset, however, we only use force curves for each pair of loading speeds and the illumination condition which corresponds to 200 force curves. We let our model classify each curve into two clusters. First, our model finds the peak count in every pull curve and assigns the label unsuccessful to ones that have no peaks. Then, we apply PCA on the rest of the curves. We select the number of components that explains 90% of variance in that particular dataset (7 to 9 components) and initialize a GMM with 2 mixture components while allowing correlations between components. We used Scikit-learn package implementations of PCA and GMM.[35]

3.3 Results and Discussion

3.3.1 *Unsupervised Classification*

The main objective of this study is to provide a robust and accurate method for classification of pulling measurements using force-distance curves into two classes: successful and unsuccessful. First, we consider unsupervised classification in order to solve this problem. Since force-distance curves have both linear and non-linear components with noise, we need to extract these linear and non-linear variation patterns to identify separate classes of force-distance curves. However, to extract such a delicate information, we need to understand and utilize that the patterns in successful pull curves are caused by a single source, unbinding of DNA strands. PCA could provide such a tool to decompose force-distance curves into a series of principal component modes that can be later used to cluster them. Thus, we tried PCA as a means to reduce dimensionality in our dataset and recover the patterns in successful pulls. After PCA, we needed to cluster the dimensionality-reduced dataset, so that we could extract scientific information from successful curves. There are many different clustering methods, such as k-means, spectral clustering and GMM. However, most of these algorithms either assume even cluster size or use distance metrics that are not suitable for the task in hand. GMM, on the other hand, can be used for many cases where the different classes have varying number of samples and the dimensions have variances different than unity. Therefore, we chose GMM for clustering.

Using PCA for dimensionality reduction and GMM for clustering, we built an unsupervised classifier model. The procedure is given in detail in the methods section of this paper. In this model, we have two assumptions: (i) there are two separate classes and (ii) for any curve to be classified as successful, it needs to have at least one peak. Using these assumptions, we were able to achieve an accuracy of 0.800 ± 0.108 and an F_1 score of 0.858 ± 0.090.

While these scores are reasonably high for an unsupervised model, they are significantly lower than the human experimenters in our lab which scored an accuracy of 0.948 ± 0.028 and an F_1 score of 0.963 ± 0.022. In order to achieve our original goal of providing a robust and accurate method, we therefore decided to look into supervised classification models.

3.3.2 *Supervised Classification*

In supervised classification, classifier models need to be adapted to suit the particular application. Classifier performance depends immensely on the nature of data, and there is no well-established method for finding an appropriate classifier for a given problem. Nonetheless, there are methods that are highly versatile and almost ready off-the-shelf, such as decision tree[34] and random forest approaches.[30] Random forest is a procedure in which classification depends on the average of many independent decision trees.[30] Decision tree models tend to over-fit their training set and may learn highly irregular patterns.[33,34] Random forests, being an ensemble method, train a set of decision trees using a random subset of dataset and features. Hence, it has low variance and slightly increased bias when compared to single decision tree models. Furthermore, they can be employed to understand what features are more important than others.[19,30]

Both decision tree and random forest methods have very few parameters to tune (3-4), and one can easily produce an accurate and reasonable model using these methods.[19] In our case, we started with decision tree and random forest models without any optimization. We reached more than 90% accuracy for binary classification (successful-unsuccessful) and 85% accuracy for multiclass classification (Class 0-4) using the 10-fold cross-validation described above. We do binary classification to extract scientific information from DFS measurements, and we expect that the multiclass classification will find use in looking at ratios of different type of events. We also evaluated 4 more classification algorithms:[33,36] Nearest Neighbor, Support Vector Machine, AdaBoost, and Naïve Bayes. The performance comparison for these algorithms is given in Table B.3 with the random forest method performing the best. For the sake of brevity, we will not discuss these other methods in this study.

In order to optimize the decision tree and random forest models, we used a 10-fold stratified cross-validation on a list of parameters as described in the methods section. For both binary and multiclass classification, we found the parameters that minimize log-loss while maximizing accuracy of decision tree model:

1. maximum 4 features to split at each node,
2. minimum 1 sample is required to split,
3. using information entropy as splitting criterion.

Since the random forest model is composed of many different decision trees that are generated from randomly selected subsets of the training dataset and the feature set, one of the main parameters of the random forest model that we expect to affect optimization is the number of trees in the model. Thus, we achieved a similar result for both random forest binary and multiclass classifiers with 1000 trees:

1. maximum 2 features to split,
2. minimum 1 sample is required to split,
3. using information entropy as splitting criterion,

We show the results for parameter selection in Table B.4 where we also compare it to classification metrics obtained for 3 different human classifiers.

Table 3.1. Classification metrics for different classifiers on the test dataset.

		Human[c]	**Decision Tree**[d]	**Random Forest**[e]
Binary	Accuracy	0.948 ± 0.028	0.918 ± 0.005	0.944 ± 0.001
	F1 score	0.963 ± 0.022	0.947 ± 0.003	0.964 ± 0.001
	Log-loss	-	2.844 ± 0.169	0.167 ± 0.006
Multiclass	Accuracy	0.911 ± 0.043	0.862 ± 0.006	0.905 ± 0.001
	$F_{1,M}$ score	0.696 ± 0.101	0.726 ± 0.011	0.785 ± 0.003
	Log-loss	-	4.774 ± 0.193	0.336 ± 0.008

Since random forest models leverage many weak learners (single decision trees) to create a strong learner, we expected the random forest models to have higher accuracy than the decision tree models. Using the best parameters that we found by cross-validation, we applied the optimized decision tree and random forest models to the test set that we split apart. As expected, the random forest model was moderately better than the decision tree model when doing binary classification having an accuracy of 0.944 ± 0.001 compared to 0.918 ± 0.005. Importantly, the random forest

---

[c] Human performance with respect to the ground truth calculated from 3 different experimenters.

[d] Mean and standard deviation of the best 10-fold cross-validated model repeated 50 times using different random states.

[e] Mean and standard deviation of the best 10-fold cross-validated model repeated 50 times using different random states.

model also has a higher accuracy compared to the decision tree model in multiclass classification where the random forest model scores 0.905 ± 0.001 and the decision tree model scores 0.862 ± 0.006. Looking at the log-loss metrics (see Table 3.1), we can say that random forest models are also significantly better in terms of assigning probabilities for our dataset. Comparing our models to human scores on the test set, the best random forest model performs as well for binary classification and less than 1% worse for multiclass classification. All the relevant metrics for these models are given in Table 3.1. From this point forward, all random forest and decision tree models that we mention are these best models unless stated otherwise.

We showed that our models can classify nearly as accurately as human experimenters on the test dataset; however, as every model, our models are prone to overfitting. Thus, we analyze their predicting abilities to check for overfitting. In the original study, Breiman et al showed that the generalization error for random forest models asymptotes as the number of trees increases.[30]

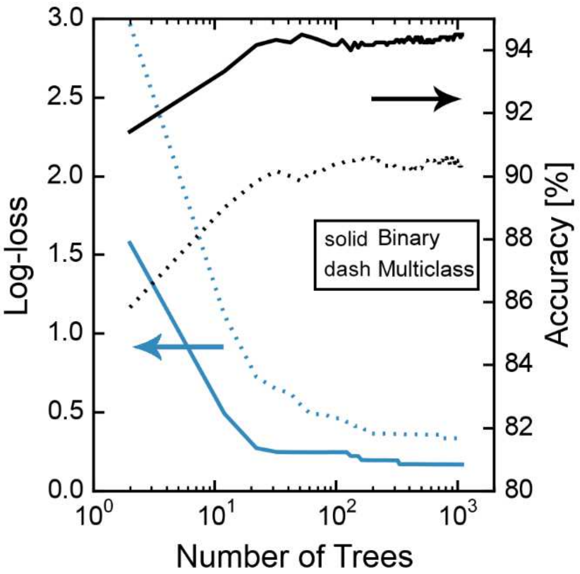

Figure 3.3. Accuracy and logarithmic loss of Random Forest classifier for binary and multiclass classifications with respect to number of trees used showing that both of them are approaching to asymptotes as the number of trees increase. Solid lines denote binary classification and dashed lines denote multiclass classification.

Similarly, we expect the accuracy and the log-loss for both random forest models to approach an asymptote, barring any random fluctuations. In order to make sure that our random forest models for both binary and multiclass classification follow this rule, we calculated the test accuracy and the log-loss of our models with increasing number of trees while keeping other parameters same. In Figure 3.3, we show these results where the change in accuracy and log-loss gets close to zero around 500 trees for both models as both of them approach to finite values asymptotically. This conforms to previous literature[30] and demonstrates that our models are not overfitting and have low variance as expected. Moreover, it points that 500 trees would be adequate for the models instead of 1000 which could decrease the computational load if that was a problem.

In physical and life sciences, one of the important metrics for experiments is the confidence levels of measurements. In classification tasks, the confidence level of the classifier for a given prediction can be obtained by predicting probabilities which may be interpreted as the confidence level of a given prediction in the case of a well-calibrated classifier.[37] To illustrate, consider a subset of the training dataset having predicted probabilities of being a successful pull of 0.3. If the classifier is well calibrated, 30% of this subset should be successful pulls. Similarly, the predicted probability of 0.7 would have 70% successful pulls implying a linear proportionality. Fortunately, random forest is one of the best learning methods for prediction confidence without any calibration.[37] We also anticipate our binary random forest model to be well-calibrated, since it incurs a low log-loss. Figure 3.4(a) shows this behavior for the binary random forest model where the calibration curve closely follows the perfect calibration. The model has a Brier score,[38] which measures the accuracy of probabilistic predictions, of 0.042, where the best and worst achievable scores are 0 and 1, respectively. This score and Figure 3.4 imply that the predicted probabilities

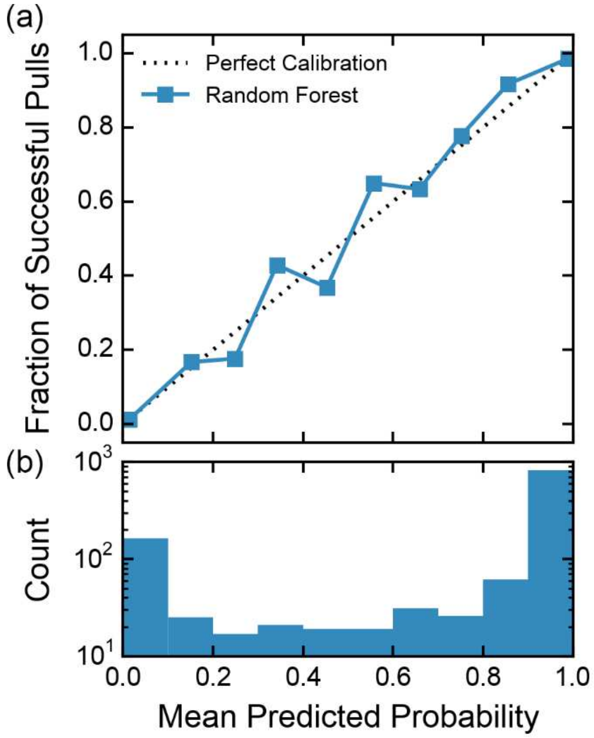

Figure 3.4. Calibration curve for the binary random forest model: **(a)** True fraction of successful pulls in bins of predicted probability showing that the model is well-calibrated, and **(b)** histogram of predicted probabilities of the test dataset.

for belonging to class by the binary random forest model can be used as confidence level of the prediction. Additionally, we supply a confusion matrix for the multiclass classifier in Figure B.1 which shows that the multiclass classifier is also well-calibrated.

Having established that our random forest models have low bias (since it has the same bias as a single decision tree) and low variance (due to the nature of averaging many decision trees), we next investigate the relevance of the variables in our feature set. Decision tree models can be used to calculate the importance of a feature by computing the total reduction of the information entropy when a split is made using that particular feature. This method of calculating feature importance can be extended to random forest models by averaging the importance of features in all trees in the forest that include those particular features.[19,30] Considering that we have modeled our feature set after our own human experience classifying pull curves, we anticipated seeing the force and the peak count among the most important features. We expect the peak count to be significantly more important than the other features for multiclass classification, as it already differentiates between Class 0, Class 4 and other classes.

In Figure 3.5, we show the measured importance of features from our random forest models. For multiclass classification we see that the peak count is the most important feature as expected, and the standard deviation is the second most important feature. For binary classification the standard deviation becomes the most important feature, being closely followed by the force. The curious reader may well ask about the relationships between these features, since one expects the standard deviation, the energy and the force to share some mutual information. For the training dataset, force-σF, force-energy and energy-σF pairs have Pearson's r-value of 0.850, 0.926 and 0.904, respectively. This points out to strong positive correlation between those variables.

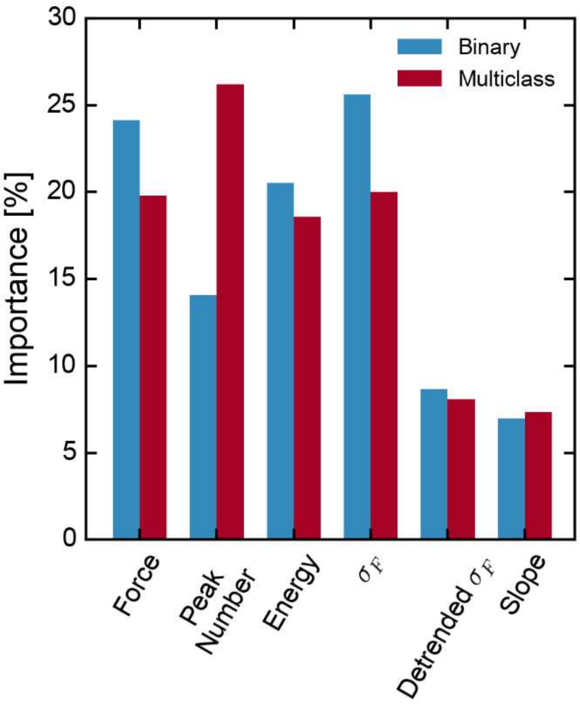

Figure 3.5. Feature importance calculated from trees in random forest classifiers. The top four features for both types of classification are the same: force, peak number, energy, and σ_F.

Although the peak count has positive r-values with respect to the other features, it does not exhibit strong correlations.

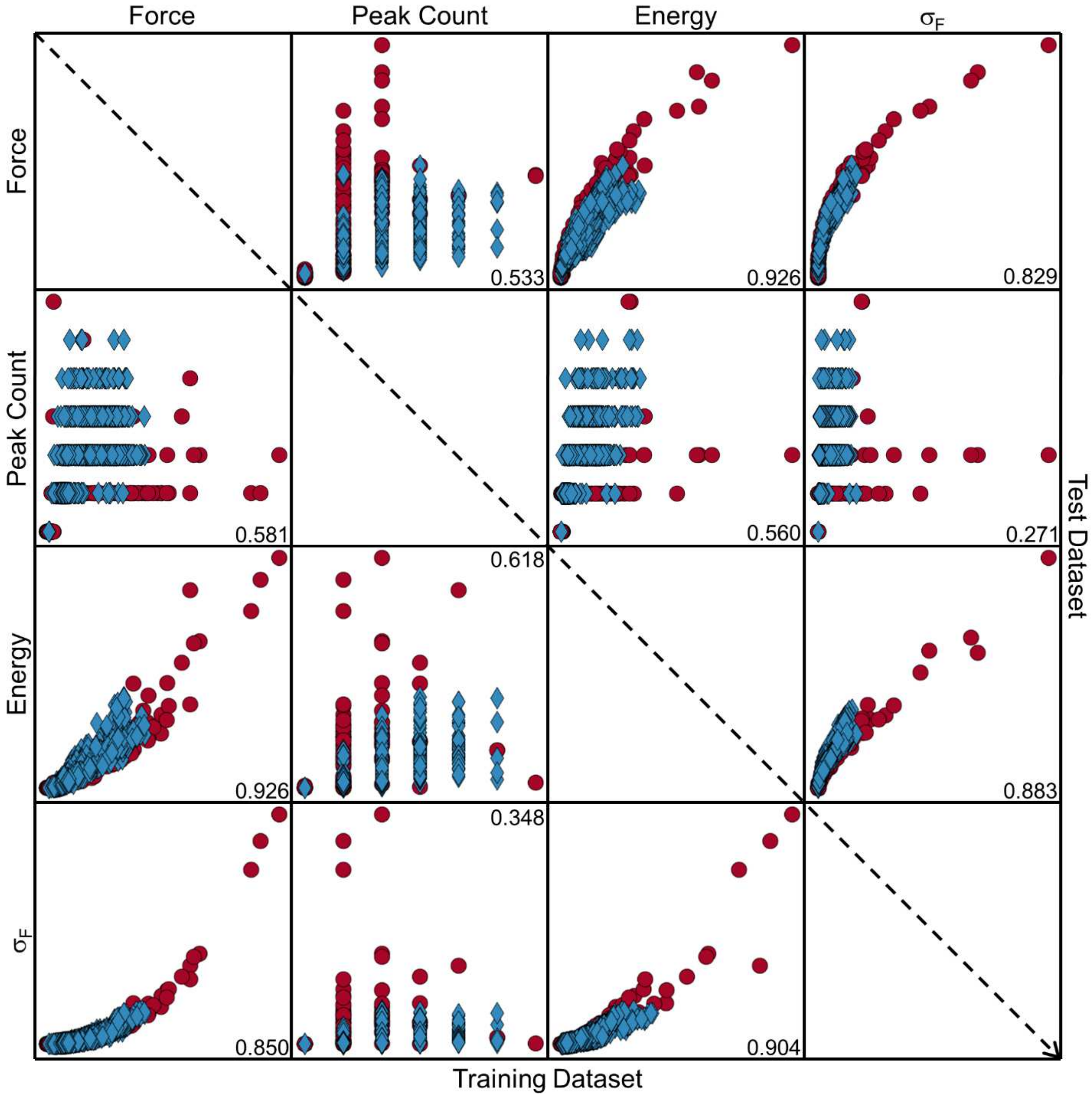

Figure 3.6. Scatter plots of the most important 4 features. The training dataset is in the lower triangle; and the test dataset is in the upper triangle. Circles (red) are unsuccessful pulls, and diamonds (blue) are successful pulls. The numbers given inside the boxes are Pearson's r values for those two features. Note that bottom and left axis increase to the right and upwards.

In Figure 3.6 we present scatter plots of the four most important features and their r-values for the training and the test datasets where these correlations can be seen clearly. To understand how these correlated variables affect our metrics, we replace them with each other and train our random forest models again using the same parameters. As a result, we see a decrease in accuracy scores on the order of 1% (see Table B.7). While it may seem counterintuitive, including several strongly correlated variables as separate classifiers does improve overall performance. We consider that the inclusion of correlated features a substitutes for the use of feature weighing, which RF models lack, as well as help to classify a few outliers.

In summary, we trained our models using a feature set that is built to replicate experimenters' experience with classification which in turn our models ranked our features similarly to human experience. This feature set includes variables that are not correlated as well as variables that are highly correlated. Thus, the highly correlated variables act as feature weighing. We tested our models for overfitting and reliability, and found that they are not creating overtrained trees to fit our dataset and are well-calibrated, thereby implying low variance and low bias. Lastly, we showed that it is possible to train random forest models to classify force-distance curves with an accuracy rate matching experimenters' accuracy rate.

3.3.3 *Loading Curves*

The goal of a DFS experiment is to extract the unbinding kinetics related to a specific force-loading curve. In previous studies, this procedure was accomplished by examining these curves by hand and/or computers using specific filters.[9,10,13] Here, we present a use case where we used azobenzene-modified photoswitch DNA in DFS experiments that is a testbed for classification models, as we expect different behavior before and after photoswitching.

Figure 3.1(c) shows the anticipated behavior of force-distance curves before and after UV illumination. Briefly, the azobenzene exists in *trans* form before illumination, and in *trans* form the amount of force to rupture double-strand DNA and the equilibrium number of stable double-strand DNAs are significantly higher.[13] After illumination with UV light, the azobenzene switches to *cis* form thereby destabilizing double-strand DNA.[13] Destabilized DNA requires a lower rupture force and has a smaller equilibrium number. Thus, we expect to observe lower rupture forces and the increase in the relative number of unsuccessful pulls to successful pulls after illumination.

As described in the methods section, we collected force-distance curves for azobenzene-modified photoswitch DNA before and after illumination with UV light using 6 different loading rates. After the experimental data is collected, we select successful curves using our models and measure the rupture force in each pull which we define as the last peak in each successful pull. Then, we fit the distribution of rupture forces to a normal distribution for every pair of illumination

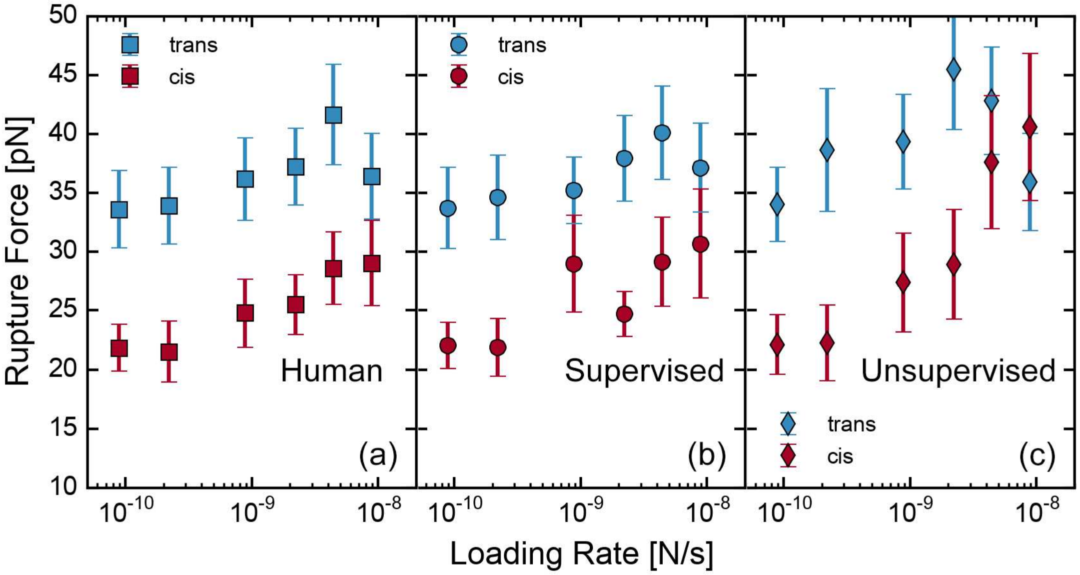

Figure 3.7. Loading curves calculated from identified successful pulls of before (*trans* form) and after (*cis* form) UV illumination showing that our random forest model is as good as the human selection in recovering the expected experimental behavior. **(a)** Ground truth (human selection), (b) supervised classifier, and (c) unsupervised classifier, respectively.

condition and loading rate in order to determine the most probable rupture force for each pair. Lastly, we plot the most probable rupture force against the loading rate. We show these plots in Figure 3.7(a), (b) and (c) for selections of successful force curves by experimenters.

Figure 3.7 shows that both of our models recovers the expected behavior and the supervised model (binary random forest model) almost as well as the human experimenters barring the outlier at 10^{-9} N/s caused by the low accuracy for those particular groups of force-distance curves. The unsupervised model (PCA + GMM), as expected with decreasing accuracy, starts differing from the human selection significantly. Nonetheless, the unsupervised model's selection still follows the same trend as other selections. We present analysis of accuracy rates for different loading speeds and illumination conditions in Table B.5 and Table B.6.

3.4 Conclusions

We explored various machine-learning methods to distinguish between successful and unsuccessful pulls, or among different classes of force-distance curves where classes are separated by other properties, i.e. number of events. By generating a feature set that spans the important properties of force curves, we were able to describe a force curve using six features. Our best performance was obtained using a supervised random forest model with which we were able to achieve robust accuracy rates of over 94% for binary classification and over 90% for multiclass classification, roughly comparable to that obtained across several human researchers in the same lab. Additionally, we described an unsupervised model composed of PCA and GMM that reaches an accuracy rate of 80%. Importantly, by using photoswitch-modified DNA, we are able to demonstrate that both the supervised and unsupervised classification schemes recover the key experimental behaviors expected for these photo-reconfigurable biomolecules – namely the decrease in binding affinity and increase in the ratio of unsuccessful to successful pulls following photo-isomerization. However, force plots constructed using the random forest supervised learning model exhibited much higher fidelity to the human-classified data in agreement with the accuracy scores for each model. We believe that there is room in the future for increasing accuracy rates of unsupervised classification by examining force-distance curves closely to understand which type of features can give rise to better clustering of the curves, possibly leveraging non-linear dimensionality reduction.

Finally, we made this available online as a software package (http://bitbucket.org/gingerlab/DNAML). We anticipate that these methods will speed up the analysis of DNA force spectroscopy experiments.

3.5 References

[1] E.W. Frey, A.A. Gooding, S. Wijeratne, and C.-H. Kiang, Front. Phys. **7**, 576 (2012).
[2] T.-H. Nguyen, L.J. Steinbock, H.-J. Butt, M. Helm, and R. Berger, J. Am. Chem. Soc. **133**, 2025 (2011).
[3] E.-S. Kim, J.S. Kim, Y. Lee, K.Y. Choi, and J.W. Park, ACS Nano **6**, 6108 (2012).
[4] C. Albrecht, K. Blank, M. Lalic-Mülthaler, S. Hirler, T. Mai, I. Gilbert, S. Schiffmann, T. Bayer, H. Clausen-Schaumann, and H.E. Gaub, Science **301**, 367 (2003).
[5] D. V Vezenov, A. Noy, and P. Ashby, J. Adhes. Sci. Technol. **19**, 313 (2005).
[6] U. Bockelmann, P. Thomen, B. Essevaz-Roulet, V. Viasnoff, and F. Heslot, Biophys. J. **82**, 1537 (2002).
[7] M.D. Wang, H. Yin, R. Landick, J. Gelles, and S.M. Block, Biophys. J. **72**, 1335 (1997).
[8] U. Bockelmann, B. Essevaz-Roulet, P. Thomen, and F. Heslot, Comptes Rendus Phys. **3**, 585 (2002).
[9] T. Strunz, K. Oroszlan, R. Schafer, and H.-J. Guntherodt, Proc. Natl. Acad. Sci. **96**, 11277 (1999).
[10] Y. Lo, Y. Zhu, and T.P. Beebe, Langmuir **17**, 3741 (2001).
[11] M. Vander Wal, S. Kamper, J. Headley, and K. Sinniah, Langmuir **22**, 882 (2006).
[12] A.R. Bizzarri and S. Cannistraro, Chem. Soc. Rev. **39**, 734 (2010).
[13] E. Sengupta, Y. Yan, X. Wang, K. Munechika, and D.S. Ginger, ACS Nano **8**, 2625 (2014).
[14] L.H. Pope, M.C. Davies, C. a Laughton, C.J. Roberts, S.J.B. Tendler, and P.M. Williams, Eur. Biophys. J. **30**, 53 (2001).
[15] R.W. Friddle, A. Noy, and J.J. De Yoreo, Proc. Natl. Acad. Sci. **109**, 13573 (2012).
[16] A. Varnek and I. Baskin, J. Chem. Inf. Model. **52**, 1413 (2012).
[17] A. Belianinov, R. Vasudevan, E. Strelcov, C. Steed, S.M. Yang, A. Tselev, S. Jesse, M. Biegalski, G. Shipman, C. Symons, A. Borisevich, R. Archibald, and S. Kalinin, Adv. Struct. Chem. Imaging **1**, 6 (2015).

[18] P. Larranaga, Brief. Bioinform. **7**, 86 (2006).
[19] W.G. Touw, J.R. Bayjanov, L. Overmars, L. Backus, J. Boekhorst, M. Wels, and S.A.F.T. van Hijum, Brief. Bioinform. **14**, 315 (2013).
[20] F. Da Silva, J. Desaphy, G. Bret, and D. Rognan, J. Chem. Inf. Model. **55**, 2005 (2015).
[21] E. Byvatov and G. Schneider, J. Chem. Inf. Model. **44**, 993 (2004).
[22] N. Schneider, D.M. Lowe, R.A. Sayle, and G.A. Landrum, J. Chem. Inf. Model. **55**, 39 (2015).
[23] J.D. Durrant, K.E. Carlson, T.A. Martin, T.L. Offutt, C.G. Mayne, J.A. Katzenellenbogen, and R.E. Amaro, J. Chem. Inf. Model. **55**, 1953 (2015).
[24] R. Kiss, M. Sándor, A. Gere, É. Schmidt, G.T. Balogh, B. Kiss, L. Molnár, C. Lemmen, and G.M. Keserű, J. Chem. Inf. Model. **52**, 233 (2012).
[25] Q. Wang, J. Park, A.K. Devkota, E.J. Cho, K.N. Dalby, and P. Ren, J. Chem. Inf. Model. **54**, 1467 (2014).
[26] R. Sznitman, A. Lucchi, P.I. Frazier, B. Jedynak, and P. Fua, Proc. 30th Int. Conf. Mach. Learn. **28**, (2013).
[27] Y. Wang, K.G. Reyes, K.A. Brown, C.A. Mirkin, and W.B. Powell, SIAM J. Sci. Comput. **37**, B361 (2015).
[28] L. Breiman, Mach. Learn. **24**, 123 (1996).
[29] Y. Freund and R.E. Schapire, J. Comput. Syst. Sci. **55**, 119 (1997).
[30] L. Breiman, Mach. Learn. 5 (2001).
[31] S. Arlot and A. Celisse, Stat. Surv. **4**, 40 (2010).
[32] M. Sokolova and G. Lapalme, Inf. Process. Manag. **45**, 427 (2009).
[33] K.P. Murphy, *Machine Learning: A Probabilistic Perspective* (MIT Press, Cambridge, MA, 2012).
[34] L. Breiman, J. Friedman, C.J. Stone, and R.A. Olshen, *Classification and Regression Trees* (Wadsworth International Group, Belmont, CA, 1984).
[35] F. Pedregosa, G. Varoquaux, A. Gramfort, V. Michel, B. Thirion, O. Grisel, M. Blondel, P. Prettenhofer, R. Weiss, V. Dubourg, J. Vanderplas, A. Passos, D. Cournapeau, M. Brucher, M. Perrot, and É. Duchesnay, J. Mach. Learn. Res. **12**, 2825 (2012).
[36] T. Hastie, R. Tibshirani, and J. Friedman, *The Elements of Statistical Learning* (Springer New York, New York, NY, 2009).
[37] A. Niculescu-Mizil and R. Caruana, in *Proceedings of the 22nd International Conference on Machine Learning - ICML '05* (ACM Press, New York, New York, USA, 2005), pp. 625–632.
[38] G.W. Brier, Mon. Weather Rev. **78**, 1 (1950).

Chapter 4. Performance Limits of Plasmon-Enhanced OPVs

4.1 Introduction[f]

Due to their strong scattering and large local-field enhancement properties, the use of plasmonic metal nanoparticles has been demonstrated as an efficient means for improving light management in organic photovoltaic devices (OPVs).[1–3] However, while a range of strategies have been presented for incorporating plasmonic particles into OPVs,[4–9] it remains an open question as to what represents the ideal placement of the nanoparticles within the device for optimum charge carrier enhancement and extraction.[10,11] Two main strategies have been pursued in the past, in which plasmonic particles have been either blended with the active layer or embedded inside charge-selecting interfacial layers. Embedding the particles in buffer layers adjacent to the active layer allows one to make use of far-field scattering while avoiding disruptions of the sensitive bulk heterojunction morphology.[5,12] At the same time, this approach may inhibit problems related to exciton quenching and charge recombination.[13,14] Furthermore, placing metal nanoparticles at the interface next to the active layer could be a potentially favorable route for enhanced forward and/or back scattering depending on whether nanoparticles are placed in the front or the back of the device, respectively.[7,15] Conversely, the close proximity of metal nanoparticles to the absorbing chromophores could ensure a more efficient use of the strong optical near-field enhancement effect.[3] The latter can achieve several orders of magnitude enhancement in local field intensity but decays quickly with increasing distance between the absorber.[16] As such, blending metal nanoparticles directly into the active layer, potentially using a thin tunnel barrier, can be

---

[f] This chapter is adapted from: D. U. Karatay, M. Salvador, K. Yao, A. K.-Y. Jen, D. S. Ginger, Performance limits of plasmon-enhanced organic photovoltaics. Appl. Phys. Lett. 105, 033304 (2014).

advantageous with regards to maximizing absorption enhancement and, consequently, the photocurrent in photovoltaic polymer blends.[17,18]

To date, most of the metal nanoparticles used to enhance OPV performance have been spherical nanoparticles of gold or silver. Those nanoparticles suffer from relatively high optical losses and rather low electric field (E-field) concentration effects,[19] when compared with more anisotropic structures. Thus, one might imagine that placing anisotropic metal nanoparticles with sharp tips, featuring high scattering to absorption ratios and strong E-field concentration properties around particle asperities,[20] in the bulk polymer blend of OPV devices could potentially allow for better exploitation of the near-field scattering mechanism.

Recently, we have shown that plasmon-resonant silver nanoprisms can act as efficient optical nanoantennas capable of significantly enhancing the yield of charge carriers in bulk heterojunction blends.[12,21–23] We therefore chose silver nanoprisms as a model system for studying the effect of the vertical position of metal nanoparticles inside the active layer of an OPV device consisting of Glass/Indium-Tin-Oxide (ITO)/poly(3, 4-ethylenedioxythiophene):poly(4-styrenesulfonate) (PEDOT:PSS)/PIDT-PhanQ:$PC_{71}BM$/Ag. PIDT-PhanQ is a phenanthroquinoxaline-based low-bandgap polymer (E_g = 1.67 eV) with reported power conversion efficiencies above 6%.[24] We show that controlling the nanoparticle position plays a critical role for engineering plasmonic OPV devices featuring both high internal quantum efficiencies and large absorption coefficients at sub-100 nm active layer thicknesses with these materials.

4.2 Methods

We first measured the external quantum efficiencies (EQE) and extracted the short-circuit photocurrents (Jsc) for OPV devices without metal nanoprisms (as reference) while varying the active layer thickness (Figure C.4(a)).[25] We then extracted the internal quantum efficiencies (IQE) as a function of the active layer thickness integrated over all wavelengths by comparing experimental J_{sc} values from EQE measurements with modeled J_{sc} values determined by computing absorption using finite-difference time-domain (FDTD) simulations (Figure 4.2(b)).[26,27] We further compared the experimental J_{sc} values of reference devices and the simulated J_{sc} values of devices containing metal nanoparticles at different relative positions inside the heterojunction blend using the FDTD formalism. Under these conditions, we find an optimum particle position close to the anode, based on which we are able to predict a maximum enhancement in J_{sc} of ~31% for comparable active layer thicknesses and ~13% compared to the overall best performing thickness without nanoparticles by additionally fine tuning the particle density.

Figure 4.1(a) schematically depicts the underlying device structure used in the experiment and simulations. In the simulations, silver nanoprisms (AgNPs) were incorporated into the active layer at different vertical positions. We extracted the size and shape of the AgNP from a transmission electron microscopy (TEM) image (Figure C.2(a))[25] of a batch of colloidal AgNPs prepared in our lab by the photo-induced conversion of nanoparticle seeds using methods described previously.[28] We chose the particle dimensions such that the particle plasmon resonance would enhance the near infrared region of the absorption spectrum once overcoated with the polymer (Figure C.3(a)).[25] The parameters extracted from the TEM micrograph are $r = 7.5$ nm, $a = 20.8$ nm and a thickness of 12 nm (r: radius of curvature, a: edge length). In particular, we positioned silver nanoprisms randomly in a horizontal plane of the active layer. This should result in a more realistic assessment of the plasmonic enhancement effect in an OPV device compared to simulations where the placement of metal nanoparticles is assumed to be periodic. All FDTD simulations were performed using Lumerical FDTD Solutions 8.7.4.[29] Importantly, we excluded the absorption within the metal nanoparticles from generating photocurrent using a refractive index filter. We take this conservative approach to allow us to better account for parasitic losses in the metal nanoparticles. The absorption of the metal is included in the simulation, but is assumed not to generate photocurrent. This procedure and other simulation details are described in detail in Appendix C.[25]

4.3 Results and Discussion

Based on the EQE measurements and the simulated absorption of the active layer (Figure 4.2(a), (b) and Figure C.4),[25] we extracted the integrated IQE as a function of the layer thickness (Figure 4.2(c)). Experimentally, the IQE decreases with increasing layer thickness. Because of the interpenetrating nature of the bulk heterojunction morphology, and the finite carrier mobility, the recombination losses tend to increase with increasing active layer thickness.[26,30] As a result the fill factor and J_{sc} tend to decrease with increasing film thickness in many OPVs. For simplicity, we focus primarily on J_{sc} here,[31] noting that the total power conversion enhancements (when

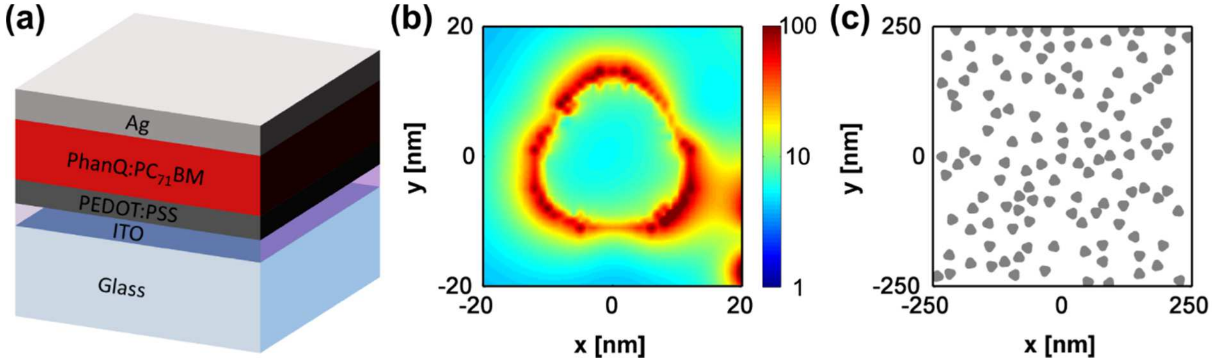

Figure 4.1. Schematics of structures used in simulations**.** (a) Device structure (Glass/ITO/PEDOT:PSS/PIDT-PhanQ:PC[71]BM/Ag). (b) The simulated E-field enhancement $|E|^2/|E_{inc}|^2$ (E_{inc} is the incident field) around a randomly selected particle, illuminated with unpolarized light when the particle density is 5 x 10^{10} cm^{-2}. The effect of neighboring nanoprisms can be seen in the bottom right. (c) 500x500 nm simulation area used for FDTD computation showing random placement of particles with a density of 5 x 10^{10} cm^{-2}.

comparing thin, plasmonically-enhanced devices relative to optically thick films) are thus more conservative estimates.

In order to overcome noise caused by sample-to-sample variation, we fit a linear curve to the integrated IQE vs. film thickness values as shown in Figure 4.2(c). We then used these wavelength-integrated IQE values to calculate J_{sc} for devices with AgNPs positioned in different locations. We note that using a single integrated IQE rather than a wavelength-dependent IQE is an approximation, but one that is justified by the relatively flat IQE vs. wavelength spectra that have been reported for many recent devices, including those using our model PIDT-PhanQ/fullerene blend.[32,33]

First, we computed J_{sc} for simulated devices with the nanoprisms positioned in 3 vertical planes: (1) directly on top of PEDOT:PSS, (2) at the vertical center of the active layer and (3) on

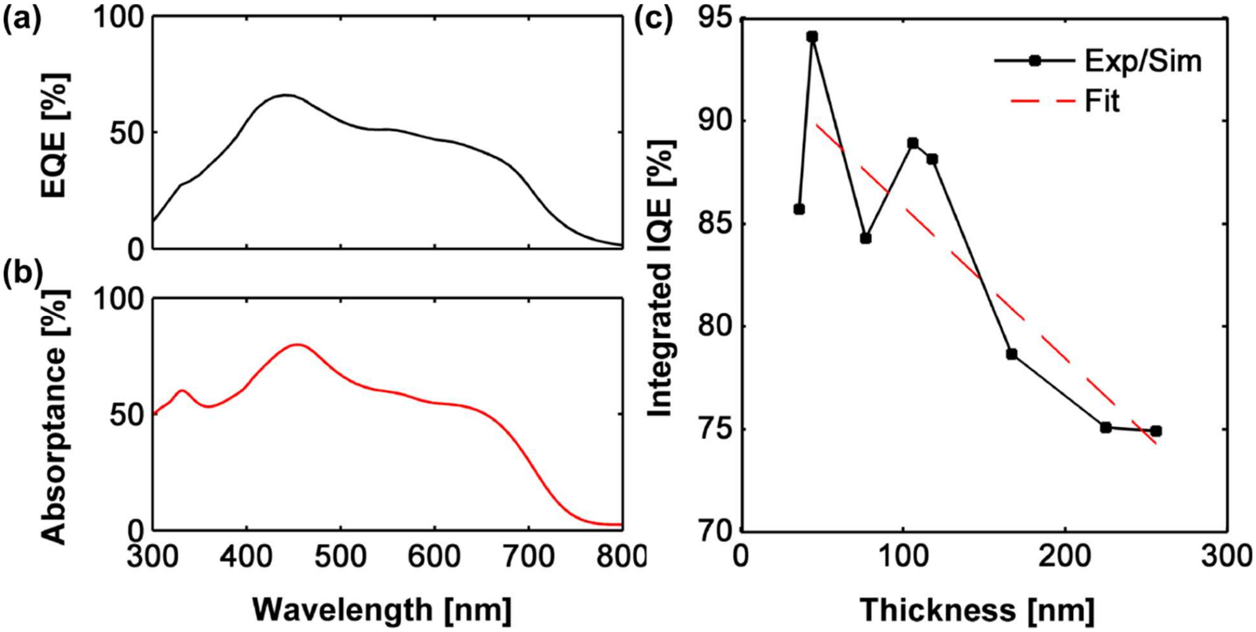

Figure 4.2. Measured EQE and simulated IQE with integrated IQE**.** (a) Measured EQE spectrum for a device with 77 nm active layer thickness along with (b) the absorption spectrum simulated using the experimentally determined materials optical constants. (c) Integrated IQE vs film thickness; the black line was extracted from experimental EQE data (a) and simulated absorption data (b), while the red line is a linear fit (IQE($\boldsymbol{t}$) $= \mathbf{0.932 - 0.0074}$ $\mathrm{nm}^{-1} \times \boldsymbol{t}$).

the silver back contact. Figure 4.3(a) shows J_{sc} for devices without AgNPs (experimental) and J_{sc} for devices with AgNPs (simulation) at the different vertical positions corrected by their respective integrated IQEs. To verify that the J_{sc} enhancement is not affected by our choice of fitting, we also carried out calculations of J_{sc} using a thickness independent IQE derived from an average of all the experimental device thicknesses (Figure C.5).[25] The initial particle density ($2x10^{10}$ cm^{-2}) for the simulated devices was set such that there would be no near-field coupling between the particles (average center-to-center particle distance is greater than $(2x10^{10}\ cm^{-2})^{-½}$ = 70 nm while the edge length of the AgNPs is ~21 nm).

Both experimental and simulated short-circuit currents shown in Figure 4.3(a) show a typical thin-film interference pattern as a function of thickness with two maxima below 250 nm. As is commonly reported for OPVs, the first interference maximum occurs at ~70 nm, whereas the second, broader maximum occurs at ~250 nm film thickness.[34–36]

Figure 4.3(a) shows that J_{sc} for the present device structure can indeed be significantly enhanced for thicknesses around the first interference maximum by placing the particles in the center of the active layer, while placing the particles on the front interface or the rear interface leads to less enhancement. As expected, around the second interference maximum the polymer film is thick enough that absorption is very efficient across all wavelengths, and nearly no enhancement can be achieved with the contribution of silver nanoprisms using the particle positions shown in Figure 4.3(a). Indeed, losses due to parasitic absorption in the plasmonic particles begin to decrease device performance for thick polymer films.

Since we observed the highest overall performance near the first interference maximum, we chose to study the device performance as a function of the z-position of AgNPs in the active layer with more detail at this thickness (77 nm). In Figure 4.3(b), we calculate J_{sc} as the AgNP layer is moved inside the active layer from the PEDOT interface towards the silver electrode. We found an optimum position of 13 nm from the PEDOT interface, which gives rise to an enhancement of 31% compared to the reference device with the same active layer thickness. We hypothesize that the shape of J_{sc} vs. AgNP position in Figure 4.3(b) is determined by complex optical interference of near-field enhancement as well as reflected and scattered light inside the device.

An additional advantage of using colloidal metal nanoparticles as optical antennas is that the absorption enhancement can be tuned by varying the particle density. In practice, the benefit of additional absorption enhancement needs to be carefully balanced against potential losses due to charge recombination, exciton quenching effects at the particle surface and reduced active material volume.

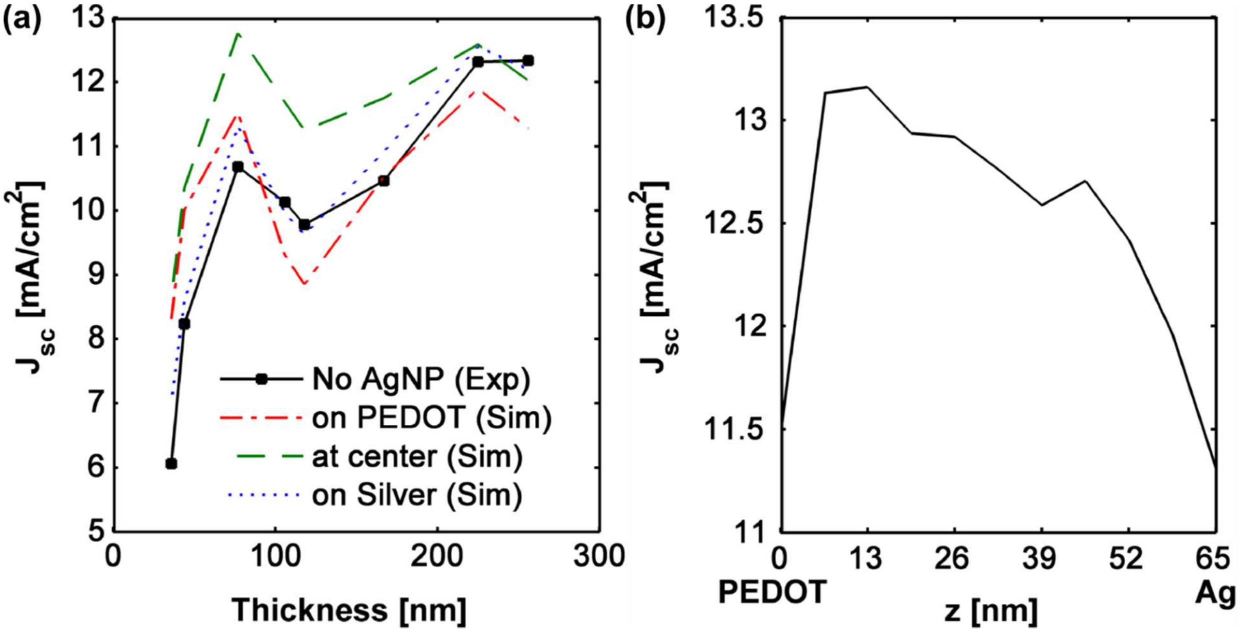

Figure 4.3. Experimental and simulated J_{sc} for z-positions**.** (a) Experimental (black) and simulated J_{sc} (including experimentally determined IQE) as a function of the active layer thickness for different positions of AgNPs in the active layer. (b) J_{sc} for different vertical positions of an AgNP film (2×10^{10} cm^{-2}) embedded in a 77 nm active layer; the positions 0 and 65 correspond to silver nanoprisms with 12 nm thickness on top of PEDOT and touching the silver contact (nanostructured back electrode), respectively.

In Figure 4.4(a), we explore the effect of the particle density on J_{sc} for the best performing plasmonic device with 77 nm thick active layer thickness. With increasing particle density J_{sc} increases, reaches a maximum and decreases again. We suspect that this result is achieved through a combination of effects. First, at low density, increasing the particle density provides for more absorption enhancement. However, as the particle density increases, interparticle interactions lead to a red-shift in the plasmon resonance peak, shifting some of the field enhancement below the band edge of the polymer (Figure 4.4(b)). In addition, as the metal particle density increases, there is a decrease in the amount of active semiconductor material and the ratio of backward scattering (reflection out of the device) to forward scattering (into the device) become less favorable (Figure C.3(b)).[25] At the maximum of the plot in Figure 4.4(a), J_{sc} reaches a value of 14.06 mA/cm^2 for a

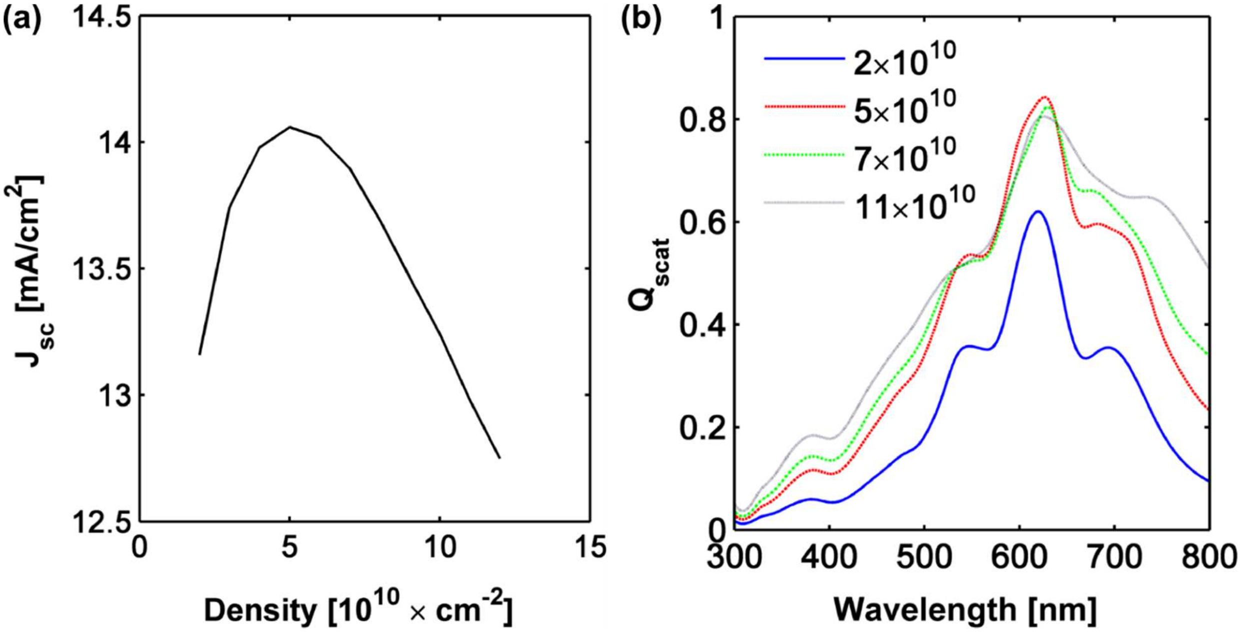

Figure 4.4. Simulated J_{sc} and Q_{scat} of various densities of nanoparticles. (a) Jsc vs particle density for a 77 nm active layer film with AgNPs localized 13 nm away from the PEDOT interface. (b) Scattering cross section normalized to the cross-sectional area of the layers of silver triangular prisms with different densities. The legend denotes the particle densities in cm^{-2}. The range of particle densities was limited to a maximum of 1.2x10^{11} cm^{-2}, since particles start to overlap at this density.

density of $5x10^{10}$ cm^{-2} (2.95% v/v), which represents an enhancement of 31% relative to the 77-nm-thick device with no nanoparticles, and still 13% compared to the overall best "optically thick" reference device with a 225 nm active layer thickness. Interestingly, this optimum density is consistent with previous reports,[12] though based on our discussion we would expect the exact optimum density to depend on particle size, shape, and the optical properties of the host matrix.

Based on the conditions we examined, we calculated the best plasmon-enhanced device performance for sub-100 nm bulk heterojunction films in the case of a 77 nm thick active layer with AgNPs positioned 15.4 nm away from the PEDOT layer and a particle density of ~$5x10^{10}$ cm^{-2}. In order to understand whether this maximum was caused by the particular randomization of positions that we chose initially, we tried 10 additional randomizations of the particle positions and orientations. We found an average J_{sc} of 14.06±0.06 mA/cm^2 (Figure C.7)[25] suggesting that our results are general and independent of the random seeding of the spatial distribution of our nanoprisms. We also simulated the same device using similar size Ag nanospheres (Figure C.6)[25] and AgNPs that are fully coated with a 1 nm thick SiO_2 charge barrier. In the former case, J_{sc} is reduced to 12.22 mA/cm^2 while in the latter case J_{sc} is reduced to 12.63 mA/cm^2. These values represent enhancements of ~14% and ~18%, respectively, compared to a corresponding reference device with the same thickness without plasmonic particles. Assuming that V_{oc} = 0.87 V and Fill Factor = 0.64[24] are not changing with the incorporation of nanoparticles,[15] the power conversion efficiency increases to 7.83% from 5.95% for a 77 nm thick device under optimum conditions.

4.4 Conclusions

Precise control of the position of a film of silver nanoprisms within the active layer can significantly improve plasmonic device performance of OPVs. When placed at a distance of ~15 nm from the PEDOT anode with a density of ~3% (v/v) the short-circuit current density of a low band-gap material with properties typical of today's OPV materials can be enhanced by over 30% compared to the reference device with the same active layer thickness and, perhaps surprisingly, by 13% even when compared to the best device thickness (225 nm). These simulated enhancements are consistent with, if somewhat larger than, those that have been achieved experimentally to date.[17,37–40] These results suggest that while current experiments are realizing a large fraction of the performance gains that are theoretically achievable, there is still some room for improvement using plasmonic enhancement schemes with the current generation of OPV materials.

4.5 References

[1] E. Stratakis and E. Kymakis, Mater. Today **16**, 133 (2013).
[2] Q. Gan, F.J. Bartoli, and Z.H. Kafafi, Adv. Mater. **25**, 2385 (2013).
[3] H.A. Atwater and A. Polman, Nat. Mater. **9**, 205 (2010).
[4] X. Li, W.C.H. Choy, L. Huo, F. Xie, W.E.I. Sha, B. Ding, X. Guo, Y. Li, J. Hou, J. You, and Y. Yang, Adv. Mater. **24**, 3046 (2012).
[5] J.-L. Wu, F.-C. Chen, Y.-S. Hsiao, F.-C. Chien, P. Chen, C.-H. Kuo, M.H. Huang, and C.-S. Hsu, ACS Nano **5**, 959 (2011).
[6] C.-H. Kim, S.-H. Cha, S.C. Kim, M. Song, J. Lee, W.S. Shin, S.-J. Moon, J.H. Bahng, N.A. Kotov, and S.-H. Jin, ACS Nano **5**, 3319 (2011).
[7] X. Yang, C.-C. Chueh, C.-Z. Li, H.-L. Yip, P. Yin, H. Chen, W.-C. Chen, and A.K.-Y. Jen, Adv. Energy Mater. **3**, 666 (2013).
[8] A.J. Morfa, K.L. Rowlen, T.H. Reilly, M.J. Romero, and J. van de Lagemaat, Appl. Phys. Lett. **92**, 013504 (2008).
[9] B.P. Rand, P. Peumans, and S.R. Forrest, J. Appl. Phys. **96**, 7519 (2004).
[10] H. Choi, J.-P. Lee, S.-J. Ko, J.-W. Jung, H. Park, S. Yoo, O. Park, J.-R. Jeong, S. Park, and J.Y. Kim, Nano Lett. **13**, 2204 (2013).
[11] R.B. Dunbar, T. Pfadler, and L. Schmidt-Mende, Opt. Express **20**, A177 (2012).
[12] K. Yao, M. Salvador, C.-C. Chueh, X.-K. Xin, Y.-X. Xu, D.W. DeQuilettes, T. Hu, Y. Chen, D.S. Ginger, and A.K.-Y. Jen, Adv. Energy Mater. DOI:10.1002/aenm.201400206 (2014).
[13] M. Salvador, B.A. MacLeod, A. Hess, A.P. Kulkarni, K. Munechika, J.I.L. Chen, and D.S. Ginger, ACS Nano **6**, 10024 (2012).
[14] M. Xue, L. Li, B.J. Tremolet de Villers, H. Shen, J. Zhu, Z. Yu, A.Z. Stieg, Q. Pei, B.J. Schwartz, and K.L. Wang, Appl. Phys. Lett. **98**, 253302 (2011).
[15] S.-W. Baek, J. Noh, C.-H. Lee, B. Kim, M.-K. Seo, and J.-Y. Lee, Sci. Rep. **3**, (2013).
[16] S.D. Standridge, G.C. Schatz, and J.T. Hupp, J. Am. Chem. Soc. **131**, 8407 (2009).
[17] V. Janković, Y.M. Yang, J. You, L. Dou, Y. Liu, P. Cheung, and J.P. Chang, ACS Nano **7**, 3815 (2013).

[18] J.-Y. Lee and P. Peumans, Opt. Express **18**, 10078 (2010).
[19] E. Hao and G.C. Schatz, J. Chem. Phys. **120**, 357 (2004).
[20] K.L. Kelly, E. Coronado, L.L. Zhao, and G.C. Schatz, J. Phys. Chem. B **107**, 668 (2003).
[21] A.P. Kulkarni, K.M. Noone, K. Munechika, S.R. Guyer, and D.S. Ginger, Nano Lett. **10**, 1501 (2010).
[22] W. Jiang, M. Salvador, and S.T. Dunham, Appl. Phys. Lett. **103**, 183303 (2013).
[23] M.M. Shahjamali, M. Salvador, M. Bosman, D.S. Ginger, and C. Xue, J. Phys. Chem. C **118**, 12459 (2014).
[24] Y. Zhang, J. Zou, H.-L. Yip, K.-S. Chen, D.F. Zeigler, Y. Sun, and A.K.-Y. Jen, Chem. Mater. **23**, 2289 (2011).
[25] See Appendix C.
[26] S. Albrecht, S. Schäfer, I. Lange, S. Yilmaz, I. Dumsch, S. Allard, U. Scherf, A. Hertwig, and D. Neher, Org. Electron. **13**, 615 (2012).
[27] G.F. Burkhard, E.T. Hoke, and M.D. McGehee, Adv. Mater. **22**, 3293 (2010).
[28] C. Xue and C.A. Mirkin, Angew. Chem. Int. Ed. Engl. **46**, 2036 (2007).
[29] Lumerical Solutions, Inc.
[30] P. Peumans, V. Bulović, and S.R. Forrest, Appl. Phys. Lett. **76**, 2650 (2000).
[31] S.H. Park, A. Roy, S. Beaupré, S. Cho, N. Coates, J.S. Moon, D. Moses, M. Leclerc, K. Lee, and A.J. Heeger, Nat. Photonics **3**, 297 (2009).
[32] C.W. Schlenker, K.-S. Chen, H.-L. Yip, C.-Z. Li, L.R. Bradshaw, S.T. Ochsenbein, F. Ding, X.S. Li, D.R. Gamelin, A.K.-Y. Jen, and D.S. Ginger, J. Am. Chem. Soc. **134**, 19661 (2012).
[33] K. Vandewal, S. Albrecht, E.T. Hoke, K.R. Graham, J. Widmer, J.D. Douglas, M. Schubert, W.R. Mateker, J.T. Bloking, G.F. Burkhard, A. Sellinger, J.M.J. Fréchet, A. Amassian, M.K. Riede, M.D. McGehee, D. Neher, and A. Salleo, Nat. Mater. **13**, 63 (2014).
[34] T. Stübinger and W. Brütting, J. Appl. Phys. **90**, 3632 (2001).
[35] L.A.A. Pettersson, L.S. Roman, and O. Inganäs, J. Appl. Phys. **86**, 487 (1999).
[36] F. Monestier, J.-J. Simon, P. Torchio, L. Escoubas, F. Flory, S. Bailly, R. de Bettignies, S. Guillerez, and C. Defranoux, Sol. Energy Mater. Sol. Cells **91**, 405 (2007).
[37] S.-W. Baek, G. Park, J. Noh, C. Cho, C.-H. Lee, M.-K. Seo, H. Song, and J.-Y. Lee, ACS Nano **8**, 3302 (2014).
[38] D.H. Wang, J.K. Kim, G.-H. Lim, K.H. Park, O.O. Park, B. Lim, and J.H. Park, RSC Adv. **2**, 7268 (2012).
[39] G.D. Spyropoulos, M.M. Stylianakis, E. Stratakis, and E. Kymakis, Appl. Phys. Lett. **100**, 213904 (2012).
[40] D.H. Wang, K.H. Park, J.H. Seo, J. Seifter, J.H. Jeon, J.K. Kim, J.H. Park, O.O. Park, and A.J. Heeger, Adv. Energy Mater. **1**, 766 (2011).

Chapter 5. Conclusions and Future Outlook

5.1 Conclusions

In this dissertation, we investigated several different computational approaches and their applications on experiments and experimental data. We showed that computationally modeling of the system under investigation coupled with experimentation leads to a greater understanding of the system and yields better results more quickly.

First, we looked into fast trEFM and the limiting factors of its time resolution. We examined how trEFM detects fast time transients in cantilever motion and the effect of the electrostatic force in detection. We demonstrated that the electrostatic force is at least as important as the electrostatic force gradient in the detection of fast local dynamics. Then we analyzed how the alignment of the electrostatic force with respect to the cantilever phase at the perturbation time affects the performance of distinguishing fast time transients. We found that the alignment of the electrostatic force with the cantilever motion is crucial for extracting information about fast rise times. Moreover, we investigated how noise affects our instrument and recommended solutions for alleviating it. After mitigating the noise, we were able to distinguish fast time transients with a rise time as short as 10 ns. We also implemented a new generation of acquisition-analysis software, in order to make imaging faster, i.e. concurrent with acquisition. We anticipate that the methods we used and proposed in Chapter 2 will find use in the development of many other scanning probe instruments and techniques.

Next, we applied machine learning methods to develop a model to label DNA pulling measurements according to their success and five different classes that are defined by other experimental features in the previous literature. We created a feature set to describe every force curve that leads to clustering of successful and unsuccessful pulls. We used random forest, an ensemble machine learning algorithm, along with an unsupervised method. Using these methods, we were able to reach accuracies of 94.4% and 80% for binary classification of force curves, using supervised and unsupervised methods respectively. This is a significant result, because human experimenters can achieve an accuracy of 94.8% on average. Additionally, we investigated our feature set to gain scientific insight to what separates a successful pull from an unsuccessful one. We believe that the methods we developed here will be used to accelerate the understanding of DNA kinetics.

Finally, we modeled OPVs with silver nanoprisms to understand how they influence device performance, incorporating experimental data. We looked into the effects of position and density of these nanoparticles inside the active layer, in addition to the thickness of the active layer. We found that the position and density of the nanoparticles affects the performance significantly. For different types of active layer materials, a specific combination of position, density and thickness can be found to enhance the performance of the device. We laid down a guideline for optimizing these parameters. Using the proposed guideline, we showed that for a modern low-bandgap material the device performance can be increased by 30% as a result of incorporating silver nanoprisms. This guideline for designing solar cells with plasmonic nanoparticles has already found use in the literature.[1,2]

5.2 Future Outlook

5.2.1 *Fast trEFM*

Since we demonstrated that the minimum distinguishable time is strongly related to the cantilever speed, it would be interesting to employ high-speed cantilevers ($f_0 > 1$ MHz) in trEFM experiments. Using high-speed cantilevers potentially could push the 10 ns limit down by two orders of magnitude, where many inorganic materials, such as perovskites, have their electronic processes happening.

A difficult but rewarding direction would be increasing the signal-to-noise ratio further to investigate biological processes, which are of interest to many researchers. The studies described in this dissertation suggest that this could be achieved by using a significantly stiffer cantilever and possibly by using a photodiode with less noise.

Another interesting direction is implementing a band-excitation method[3,4] for trEFM, where a frequency band is supplied to the resting cantilever at the same time as the external perturbation to the sample. The resulting cantilever motion can be Fourier-analyzed in order to gain insight to the material. This could open the door to the analysis of systems with strongly non-linear responses.

Lastly, implementing compressive sensing for faster imaging could be extremely useful to everyday users of the instrument.

5.2.2 *Classifying Force Spectroscopy of DNA Pulling Measurements*

As we showed with supervised methods, it is possible to reach accuracy rates close to human experimenters. It would be exciting to implement an online machine learning algorithm, such as EXP3[5] or UCB1,[6] that keeps learning over time as experimenters continue to acquire more pulling curves, thus pushing accuracies higher. Another useful aspect of this would be using it while doing an experiment and being able to save only successful curves, allowing experimenters to use the minimum number of runs required to obtain a desired number of curves.

Additionally, with more insight to the mathematical properties of force curves, it would be interesting to see what types of curves cluster together using an unsupervised technique. This may lead to a better understanding of DNA kinetics.

5.2.3 *Performance Limits of Plasmon-Enhanced OPVs*

It would be interesting to explore different particle structures, such as shell-core particles, coupled particles, and anisotropic particles, and different noble metals and their effect on the device performance.

Another interesting follow-up study would be looking at plasmon resonances with respect to the band-gap of the active layer material, exploring the optimum relationship between the plasmon resonance and the band-gap.

5.3 References

[1] W.E.I. Sha, H.L. Zhu, L. Chen, W.C. Chew, and W.C.H. Choy, Sci. Rep. **5**, 8525 (2015).
[2] W.C.H. Choy and X. Ren, IEEE J. Sel. Top. Quantum Electron. **22**, 1 (2016).
[3] S. Jesse, R.K. Vasudevan, L. Collins, E. Strelcov, M.B. Okatan, A. Belianinov, A.P. Baddorf, R. Proksch, and S.V. Kalinin, Annu. Rev. Phys. Chem. **65**, 519 (2014).
[4] L. Collins, S. Jesse, N. Balke, B.J. Rodriguez, S. Kalinin, Q. Li, L. Collins, S. Jesse, N. Balke, B.J. Rodriguez, and S. Kalinin, **104102**, (2015).
[5] P. Auer, N. Cesa-Bianchi, Y. Freund, and R.E. Schapire, SIAM J. Comput. **32**, 48 (2002).
[6] P. Auer, N. Cesa-Bianchi, and P. Fischer, Mach. Learn. **47**, 235 (2002).

Appendix A. Fast Time-Resolved EFM

Trigger Circuitry. The function of trigger circuitry is to produce signals to control perturbation and trigger a digitizer, in a manner that is phase synchronous with the deflection signal coming from the AFM cantilever. The controller accepts as inputs the deflection signal (DEF) and a trigger request signal (REQ). Once the trigger request is asserted, the controller delays asserting the output signals until the deflection signal reaches a specified phase position. The controller's phase resolution is 8 bits, 128 values in [0°, 360°).

Trigger circuitry is composed of two separate hardware modules: the optical isolator that receives the reference and trigger request signals from the AFM chassis, and the phase shift controller that generates a signal (OUT) to trigger the digitizer and activate the perturbation. The two modules are connected by a pair of optical fibers, in order to minimize feedbacks in circuitry. The phase shift controller is implemented using a phase locked loop (PLL) as illustrated in Figure A.1.

Finding Minimum. In order to find minimum of a curve, one can use many different methods. Here, due to the noisy nature of signal, we prefer to fit the signal with an analytical approximation of the curve and use the fit parameters to calculate the minimum. The analytical approximation is composed of two parts: decay and relaxation. These are defined as follows:

$$\omega_D(t) = Ae^{-\frac{t}{\tau_1}},$$

$$\omega_R(t) = B\left(1 - e^{-\frac{t}{\tau_2}}\right),$$

where A and B are normalization constants; τ_1 and τ_2 are time constants for decay and relaxation respectively. We fit the signal with:

$$\omega(t) = Ce^{-\frac{t}{\tau_1}}\left(1 - e^{-\frac{t}{\tau_2}}\right), \text{where } t > 0.$$

The minimum of this equation is t_{FP} and it is:

$$t_{FP} = \tau_2 \ln\left(\frac{\tau_1 + \tau_2}{\tau_2}\right).$$

Gold Electrode. In the experiments, we have used a silicon wafer sputtered with a thin gold film that is attached to the waveform generator using conductive Silver paint (Leitsilber 200 Silver Paint). The surface roughness of the gold electrode is measured to be 2.29 nm.

Spectrum Analysis. We analyzed the power spectrum of different cantilevers by measuring their thermal spectra and tuning them using their thermally measured properties. After tuning, we drove tips as we collected data. For BlueDrive measurements, we measured properties of tips while the laser was on, but not pulsing.

For different cantilevers, we found that their resonance frequency gets slightly smaller (~10 Hz) when we use BlueDrive. Also, BlueDrive has better signal-to-noise ratio compared to piezoacoustic drive (bandwidth of 5 kHz around the resonant frequency).

Table A.1. The signal-to-noise ratio for different cantilevers used in the experiments when they are driven by BlueDrive and piezoacoustic drive. The calculation was done around the cantilever's resonant frequency with 5 kHz bandwidth.

	BlueDrive	**Piezoacoustic Drive**
ElectriMulti75-G (75 kHz)	61.12 dB	61.05 dB
ElectriTap190-G (190 kHz)	64.38 dB	62.48 dB
ElectriTap300-G (300 kHz)	63.38 dB	54.76 dB
DDESP-V2 (450 kHz)	64.20 dB	58.81 dB

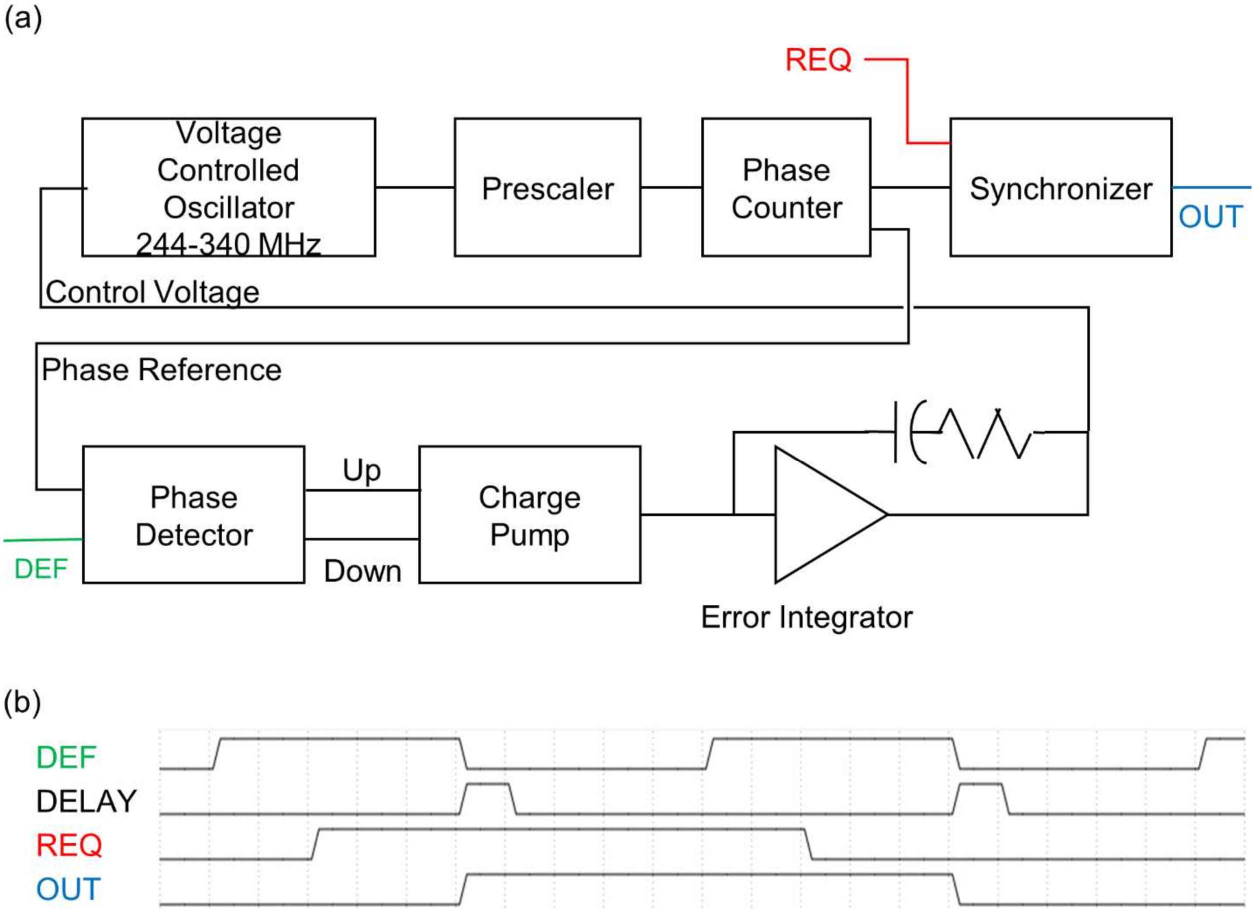

Figure A.1. Flow diagram for trigger circuitry. (a) PLL circuit for phase shift controller. DEF, REQ, and OUT are the deflection signal from cantilever, the trigger request and the signal to trigger digitizer and the perturbation, respectively. (b) The timing diagram illustrates a case where the output is asserted 180° after the rising edge of the deflection signal.

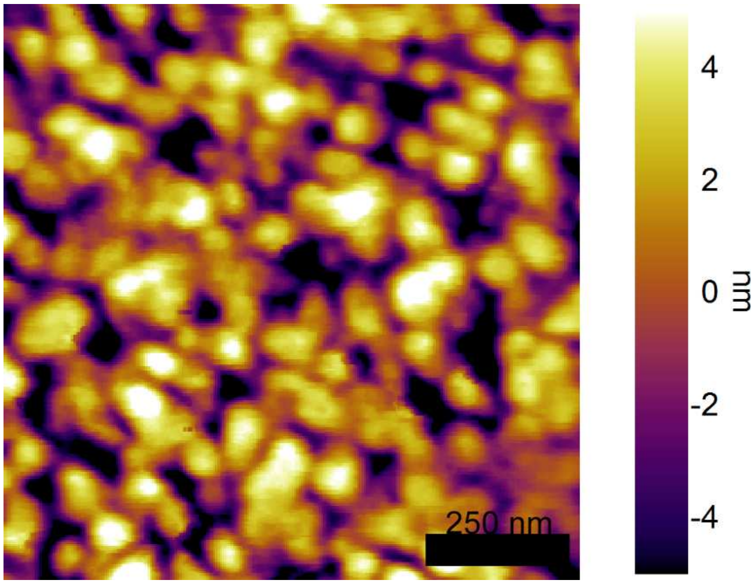

Figure A.2. Topography image of the gold electrode surface.

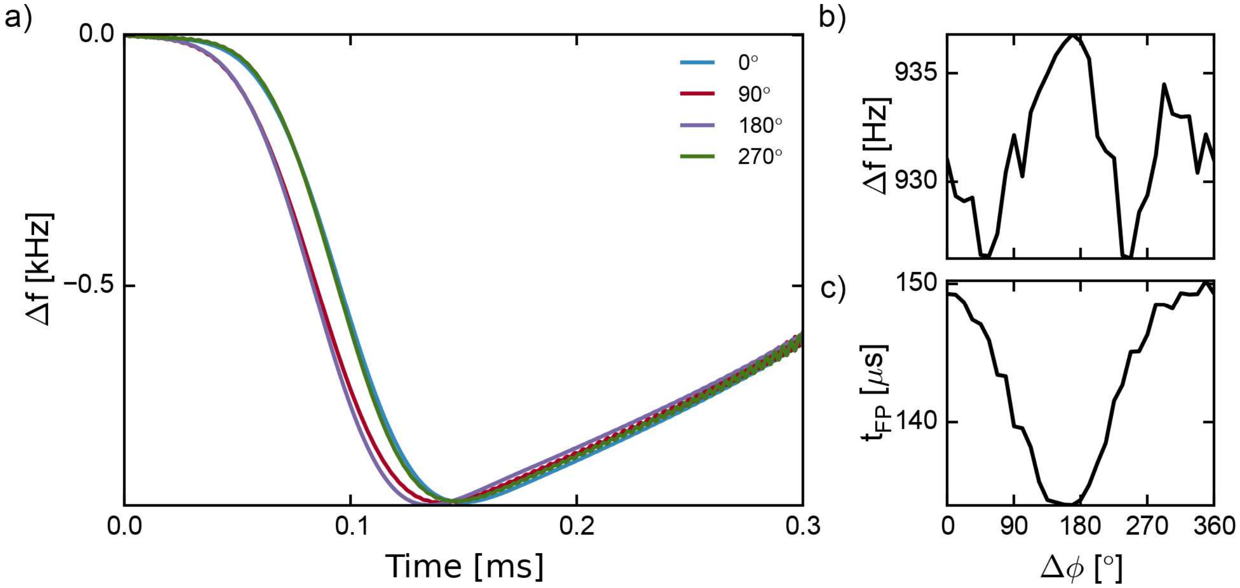

Figure A.3. Experimental instantaneous frequency curves. Excitation has a rise time of 100 ns and the V_{bias} = 10 V at 50 nm lift height. (a) Instantaneous frequency after trigger for excitation at different phases, (b) frequency shifts and (c) t_{FP}'s at different phases. (f_0 = 272.218 kHz, k = 26.2 N/m and Q = 432)

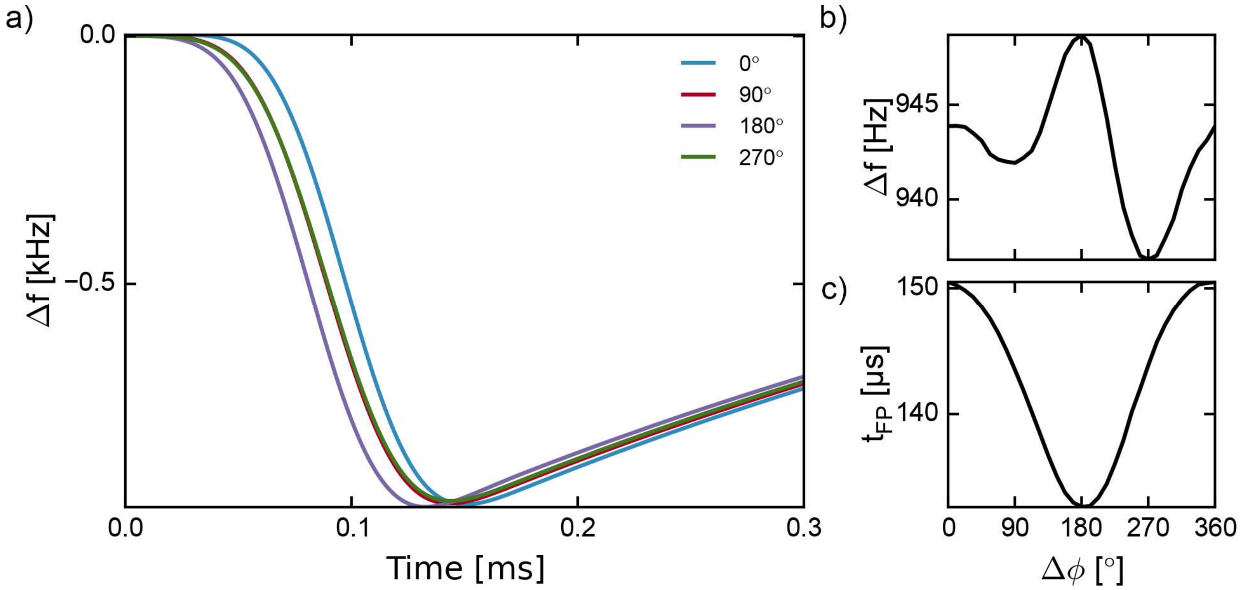

Figure A.4. Simulated instantaneous frequency curves. Excitation has a rise time of 100 ns and the V_{bias} = 10 V at 50 nm lift height. (a) Instantaneous frequency after trigger for excitation at different phases, (b) frequency shifts and (c) t_{FP}'s at different phases. (f_0 = 272.218 kHz, k = 26.2 N/m and Q = 432)

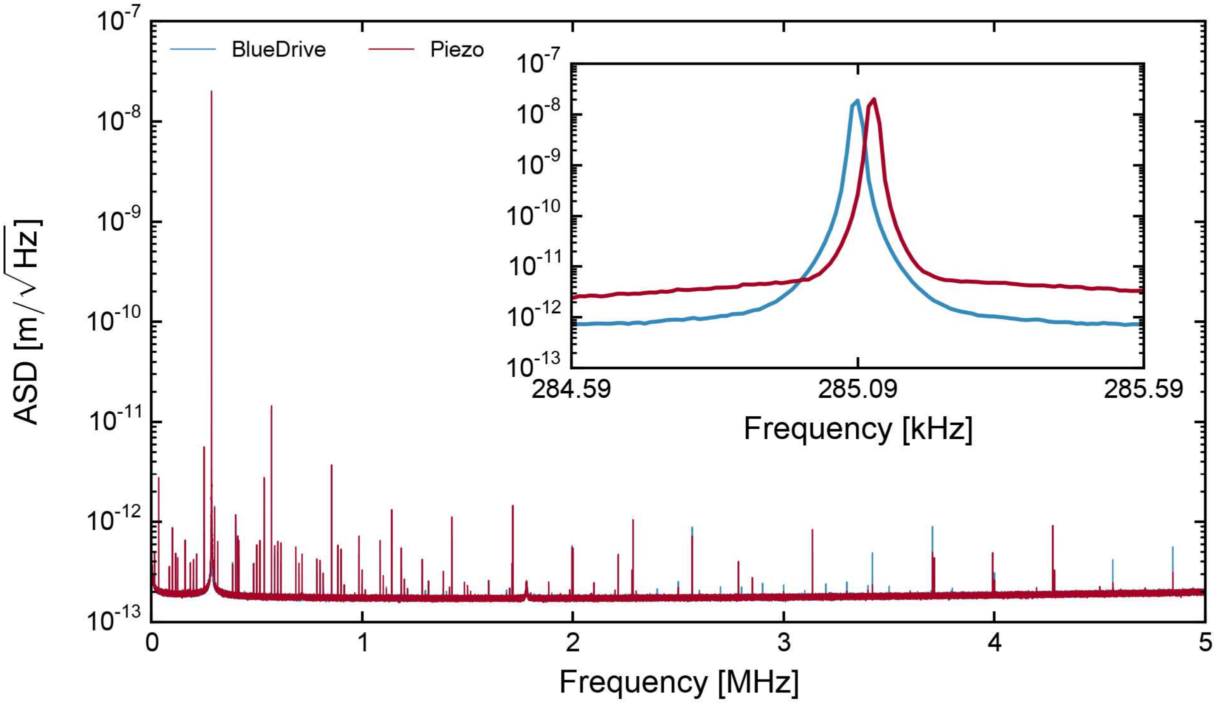

Figure A.5. Amplitude spectral density measurements. Series of peaks are the response of instrument's electronics. Inset shows a zoom-in around the resonant frequency. Note the difference between baselines. (f_0 = 285.090 kHz, k = 25.2 N/m and Q = 451)

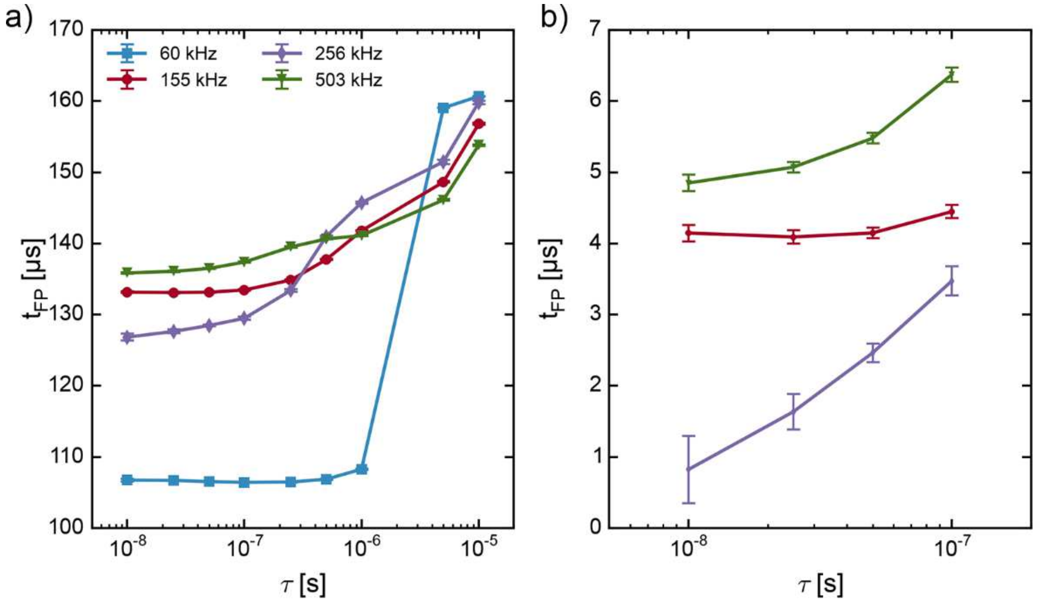

Figure A.6. Effect of different resonance frequencies on t_{FP} measurements. (b) Zoom-in of Fig. 10(c) showing that the 256 kHz cantilever's standard deviations are much larger causing minimum distinguishable rise time to be bigger than the 503 kHz tip. The scale is shifted to make error bars visible. The cantilever parameters are $f_0 = 60.219$ kHz, $k = 1.37$ N/m, $Q = 150$; $f_0 = 154.806$ kHz, $k = 15.8$ N/m and $Q = 352$; $f_0 = 255.920$ kHz, $k = 17.9$ N/m and $Q = 428$; and $f_0 = 503.327$ kHz, k = 72.7 N/m and Q = 499. AFM cantilevers were excited at 180° using BlueDrive. The μ_{tFP} and σ_{tFP} values are compiled from 30 different runs of the same experiment. Every run consists of 2000 averages of raw cantilever deflection signal.

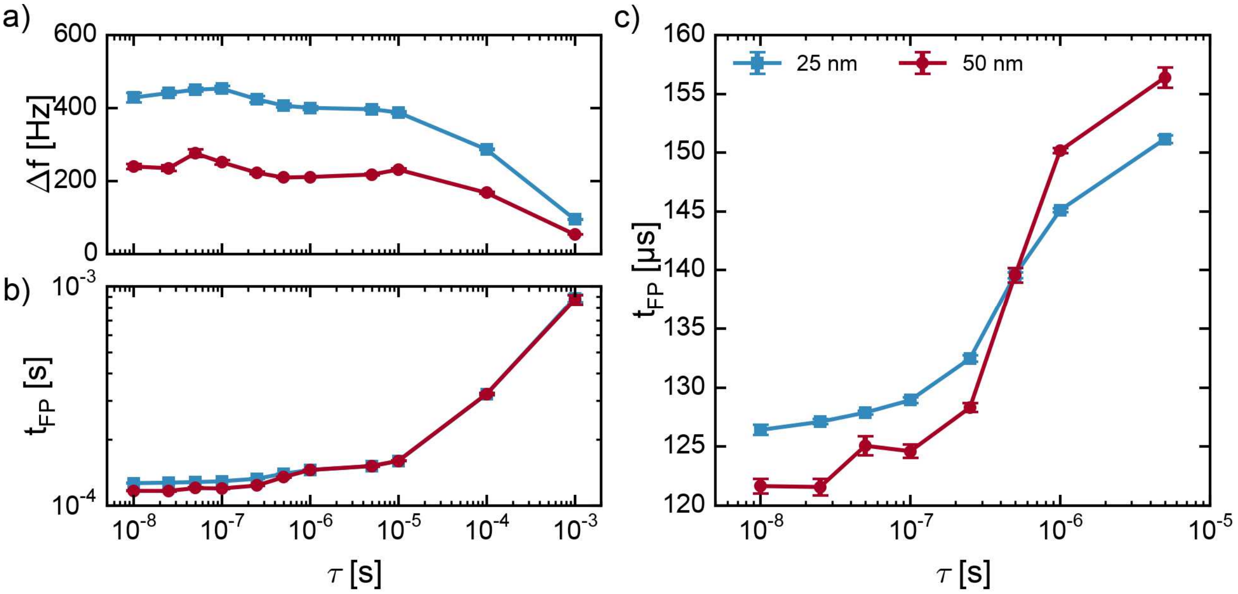

Figure A.7. Comparison of different lift heights. Experimental (a) frequency shifts and (b) t_{FP}'s for an AFM cantilever excited at 180°. The cantilever parameters are $f_0 = 255.920$ kHz, k = 17.9 N/m and Q = 428. (c) Zoom in for faster decays. The μ_{tFP} and σ_{tFP} are compiled from 30 different runs of the same experiment. Every run consists of 2000 averages of raw cantilever deflection signal.

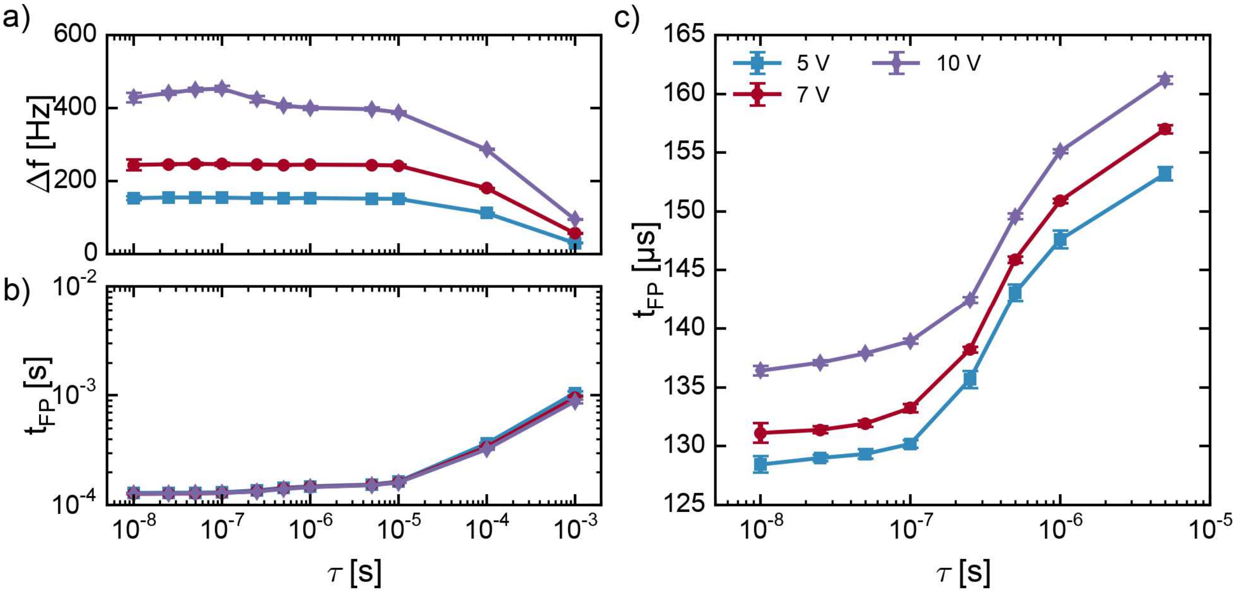

Figure A.8. Comparison of different biases. Experimental (a) frequency shifts and (b) t_{FP}'s for an AFM cantilever excited at 180°. The cantilever parameters are $f_0 = 255.920$ kHz, k = 17.9 N/m and Q = 428. (c) Zoom in for faster decays. The μ_{tFP} and σ_{tFP} are compiled from 30 different runs of the same experiment. Every run consists of 2000 averages of raw cantilever deflection signal.

Appendix B. Classifying Force Spectroscopy of DNA Pulling Measurements

Table B.1. Class ratios before UV illumination per loading rate.

	20 nm/s	50 nm/s	200 nm/s	500 nm/s	1000 nm/s	2000 nm/s
Class 0	1.50%	0%	0%	0%	10.50%	0%
Class 1	6%	1.50%	3%	0.50%	0%	0%
Class 2	2%	0%	7%	8.50%	5%	7.54%
Class 3	7.50%	0%	0%	0%	1%	0%
Class 4	83%	98.50%	90%	91%	83.50%	92.46%

Table B.2. Class ratios after UV illumination per loading rate.

	20 nm/s	50 nm/s	200 nm/s	500 nm/s	1000 nm/s	2000 nm/s
Class 0	27.50%	26.50%	27.50%	1%	27.50%	16.50%
Class 1	13.50%	12.50%	5%	8%	4%	7%
Class 2	0.50%	1.50%	3.50%	4%	9%	13.50%
Class 3	26.50%	50%	51%	37%	47.50%	39%
Class 4	32%	9.50%	13%	50%	12%	24%

Table B.3. Comparison of different classification algorithms without optimization.

	Binary			**Multiclass**		
	Accuracy	F_1-score	Log-loss	Accuracy	$F_{1,M}$-score	Log-loss
Human	0.966±0.015	0.979±0.009	-	0.941±0.026	0.853±0.076	-
3NN	0.910±0.026	0.945±0.016	0.991±0.397	0.823±0.012	0.632±0.057	2.710±0.503
SVM (RBF)	0.850±0.019	0.912±0.010	0.385±0.044	0.634±0.017	0.302±0.030	1.017±0.048
Decision Tree	0.931±0.023	0.956±0.014	2.386±0.805	0.864±0.043	0.748±0.088	4.711±1.491
Random Forest	0.939±0.017	0.961±0.011	0.481±0.359	0.906±0.020	0.794±0.052	1.095±0.511
AdaBoost	0.930±0.016	0.961±0.011	0.637±0.003	0.511±0.043	0.499±0.041	1.373±0.119
Naïve Bayes	0.909±0.033	0.943±0.020	0.316±0.101	0.835±0.028	0.692±0.050	1.049±0.299

Table B.4. Comparison of the best DT and RF models for 10-fold cross-validation.

	Binary			**Multiclass**		
	Accuracy	F_1-score	Log-loss	Accuracy	$F_{1,M}$-score	Log-loss
Human	0.966±0.015	0.979±0.009	-	0.941±0.026	0.853±0.076	-
Decision Tree	0.929±0.020	0.955±0.013	2.446±0.693	0.885±0.031	0.784±0.057	3.963±1.086
Random Forest	0.939±0.013	0.962±0.008	0.167±0.100	0.913±0.029	0.811±0.067	0.391±0.172

Table B.5. Accuracy rates before UV illumination per loading rate.

	20 nm/s	**50 nm/s**	**200 nm/s**	**500 nm/s**	**1000 nm/s**	**2000 nm/s**
Human (Test)	0.963±0.026	0.957±0.012	0.990±0.000	0.950±0.016	0.970±0.008	0.967±0.005
Supervised - RF (Test)	0.926±0.005	0.936±0.005	0.990±0.000	0.970±0.000	0.970±0.000	0.960±0.000
Human (All)	0.960±0.029	0.963±0.015	0.988±0.002	0.950±0.011	0.958±0.002	0.962±0.002
Unsupervised (All)	0.813±0.112	0.847±0.099	0.697±0.060	0.645±0.039	0.844±0.077	0.690±0.018

Table B.6. Accuracy rates after UV illumination per loading rate.

	20 nm/s	**50 nm/s**	**200 nm/s**	**500 nm/s**	**1000 nm/s**	**2000 nm/s**
Human (Test)	0.970±0.022	0.913±0.074	0.930±0.045	0.927±0.054	0.950±0.037	0.887±0.070
Supervised - RF (Test)	0.950±0.000	0.949±0.003	0.914±0.006	0.931±0.005	0.944±0.005	0.884±0.006
Human (All)	0.972±0.021	0.908±0.078	0.933±0.057	0.940±0.049	0.932±0.049	0.893±0.070
Unsupervised (All)	0.719±0.035	0.859±0.086	0.897±0.072	0.874±0.072	0.898±0.015	0.810±0.011

Feature Importances. In order to understand how the features affect the metrics, we replaced the features with each other and trained and tested the dataset with the same parameters. We replace force-σ_F, force-energy and energy-σ_F; and train our Random Forest model again.

Table B.7. Classification metrics for RF models with replaced features.

	Binary			**Multiclass**		
	Accuracy	F_1-score	Log-loss	Accuracy	F_1-score	Log-loss
RF	0.944±0.001	0.964±0.001	0.167±0.006	0.905±0.001	0.785±0.003	0.336±0.008
F to STD	0.940±0.001	0.962±0.001	0.173±0.007	0.894±0.006	0.765±0.003	0.463±0.017
F to E	0.935±0.001	0.958±0.001	0.181±0.010	0.900±0.001	0.783±0.003	0.355±0.012
STD to E	0.941±0.001	0.963±0.001	0.178±0.010	0.901±0.001	0.784±0.003	0.338±0.005

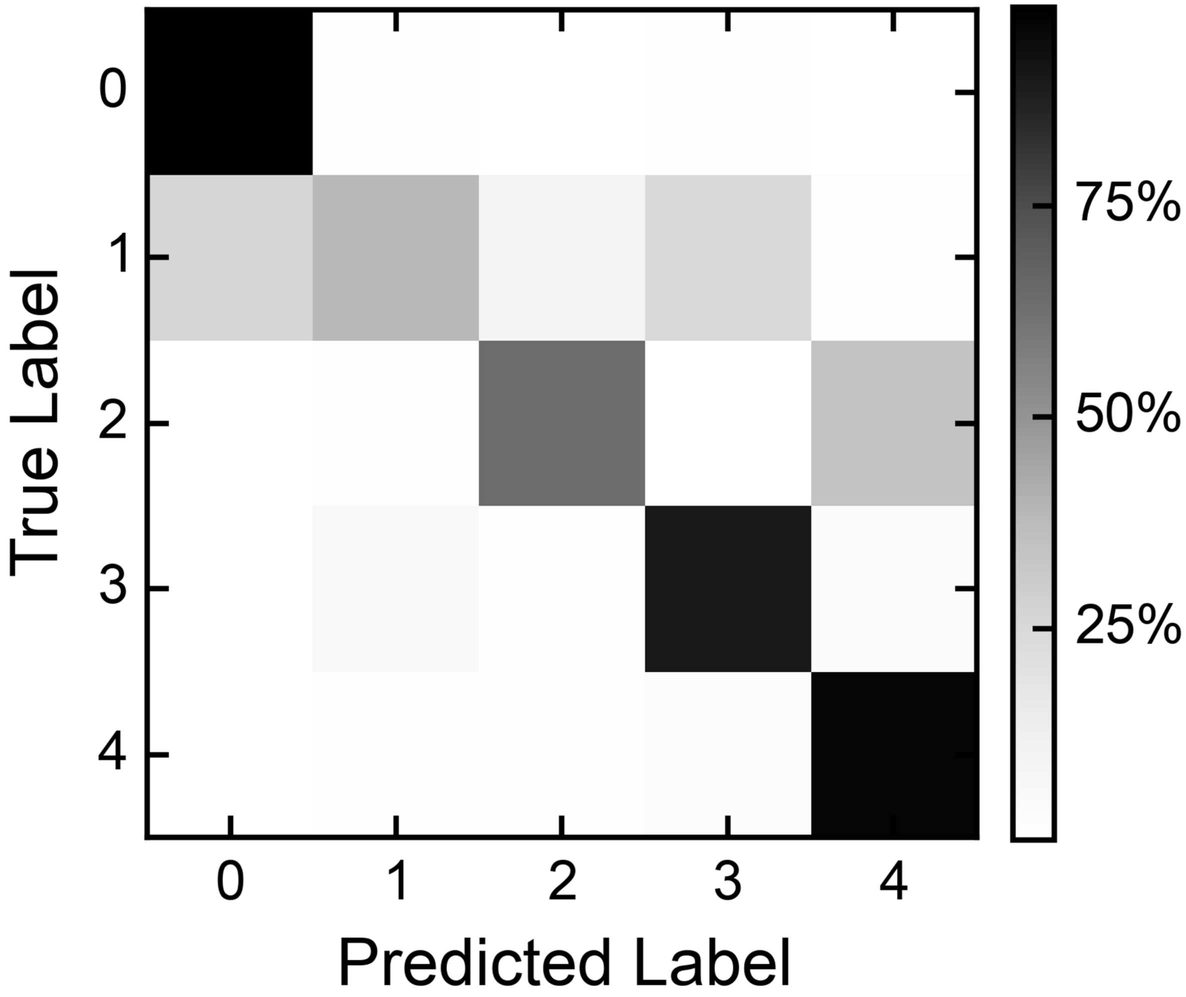

Figure B.1. Normalized confusion matrix for the best multiclass RF model. Rows denote true labels, and columns denote predicted labels. Diagonal elements are percentages of correct predictions for a given class, and off-diagonal elements are percentages of confused elements for a given class.

Appendix C. Performance Limits of Plasmon Enhanced OPVs

Simulation Details. We used a commercial grade electrodynamics simulator package, Lumerical FDTD Solutions 8.7.4, for running finite-difference time-domain calculations. We meshed the simulation region (500 nm x 500 nm) using staircase meshing in order to exclude the absorption originating from the metal nanoparticles. The absorption of the nanoparticles was excluded using a refractive index filter. The mesh was set to 2 nm in z-direction to correctly mesh planar structures. We positioned particles in the simulation region and varied their orientation using random numbers from a uniform distribution. Beyond this randomization region the boundary conditions were chosen to be periodic.

The refractive index filter for absorption works by zeroing the absorption at points where the index of refraction is equal to Ag at that wavelength. We used the method described by Lumerical (http://docs.lumerical.com/en/fdtd/solar_plasmonic_definitions.html) to calculate J_{sc} from absorption.

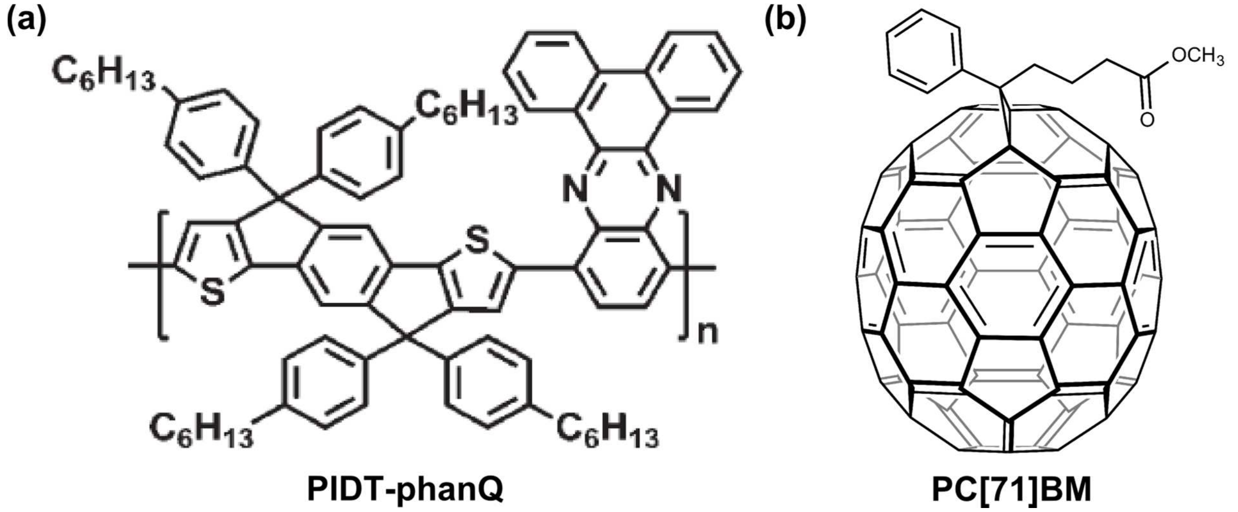

Figure C.1. Chemical structures of the active layer OPV materials. (a) PIDT-PhanQ and (b) PC[71]BM.

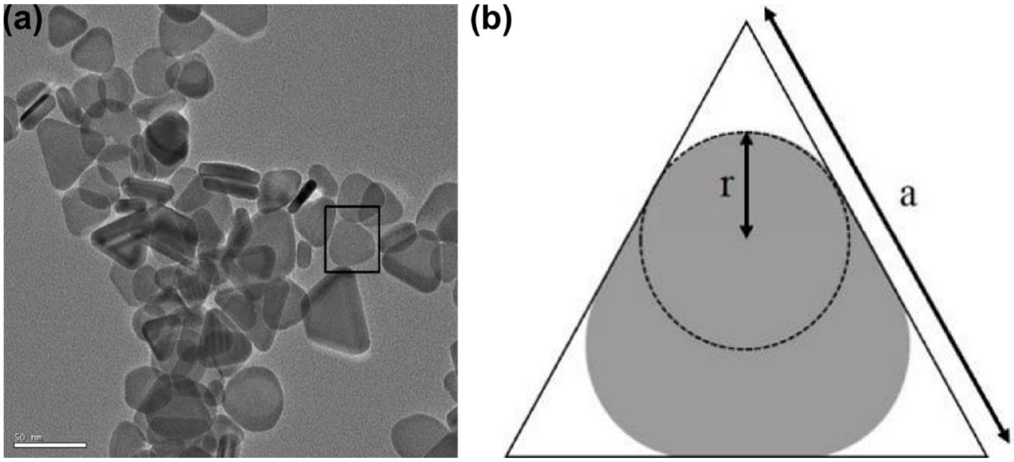

Figure C.2. TEM micrograph and schematic of silver nanoprisms. (a) Representative TEM micrograph of colloidal silver nanoprisms. The black box shows the particle we chose for calculating the surface plasmon enhancement in low-bandgap OPVs. (b) Schematic representation of the silver nanoprism used for our simulations. The geometry of the particle is given by r = 7.5 nm, a = 20.78 nm and a thickness of 12 nm.

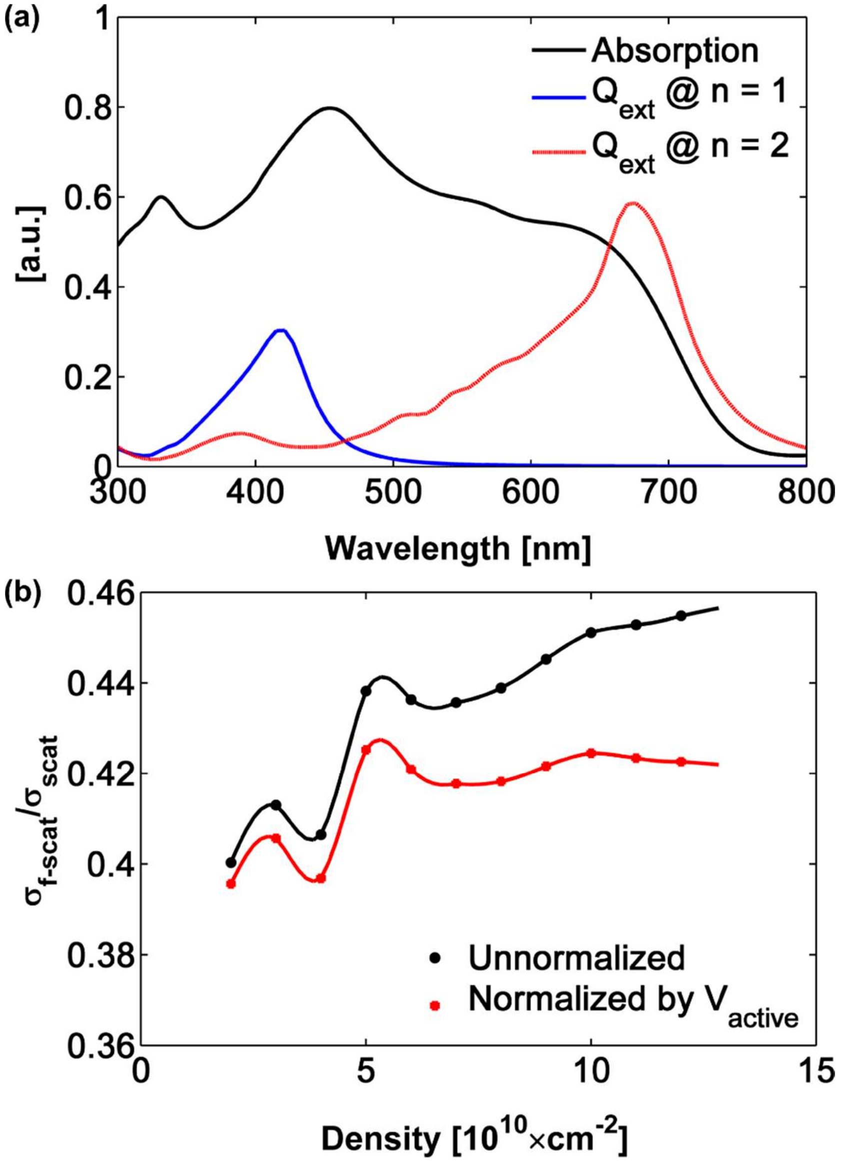

Figure C.3. Simulated absorption, Q_{ext}, and scattering ratios. (a) Calculated absorption of a 77 nm thick PIDT-PhanQ:PC[71]BM film and extinction spectra for a single nanoprism assuming refractive indices of 1 and 2 for the surrounding medium (the average refractive index of PhanQ:PC[71]BM is ~2 for wavelengths between 300 – 800 nm). (b) Black circles denote the ratio of integrated forward scattering to total scattering for a layer of randomly distributed AgNPs; in the case of the red circles the same ratio is normalized by the effective volume of active material, i.e., active volume minus volume of AgNPs. The smoothed lines are a guide to the eye.

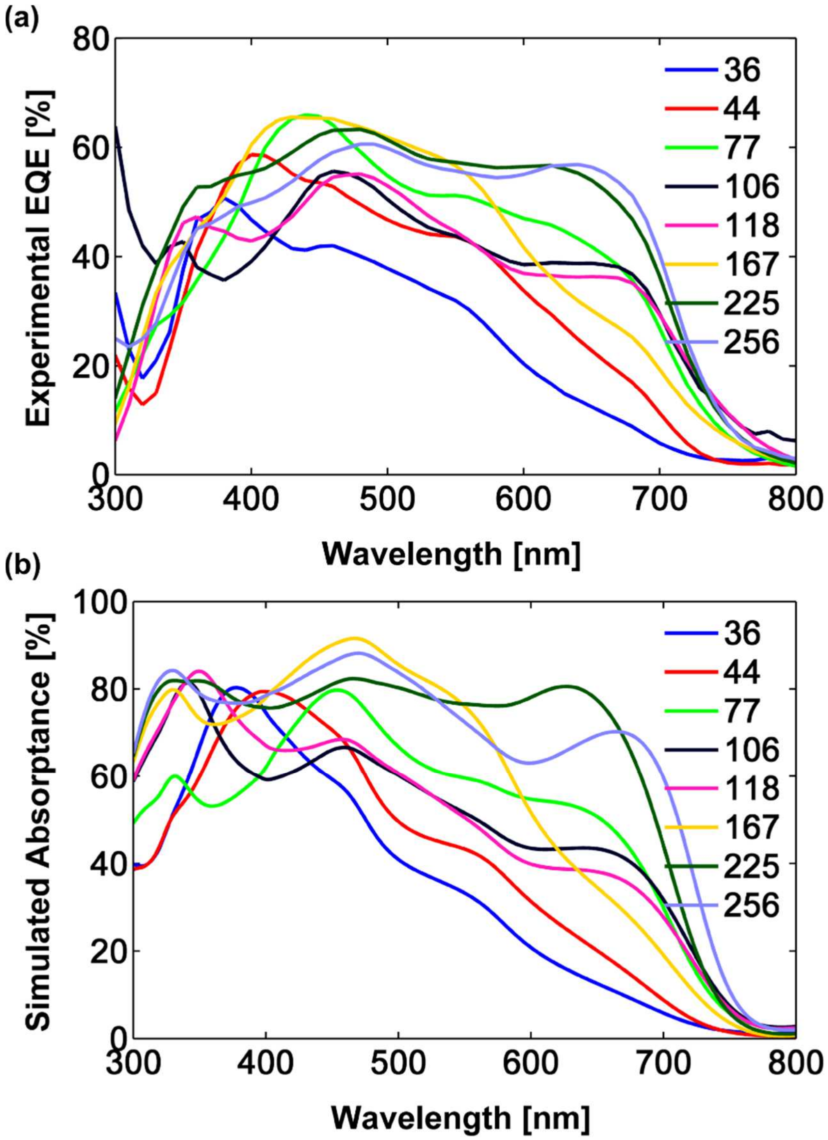

Figure C.4. Experimental EQE and simulated absorption spectra. (a) Experimental EQE spectra for different active layer thicknesses. (b) Simulated absorption spectra for the same active layer thicknesses as in (a).

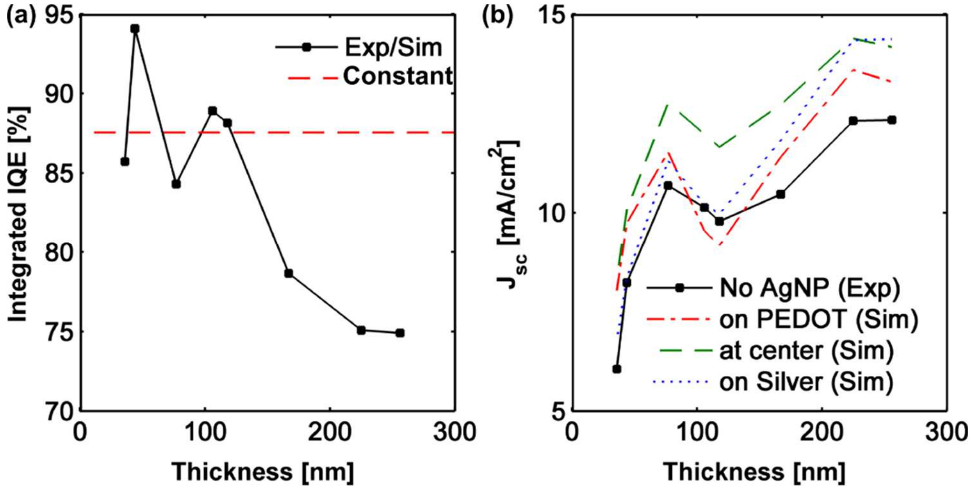

Figure C.5. J_{sc} for a constant integrated IQE.(a) Integrated IQE vs film thickness; the black line represents the experimental/modeled data, while the red line represents the thickness independent IQE that was used for calculating Jsc in (b). For ease of comparison, the IQE was chosen to be the same as for a 77 nm thick film using the linear fit in Figure 4.2(b) (0.88). (b) Corrected Jsc for different positions of an AgNP film embedded in the active layer using a thickness independent IQE (red line in (a)).

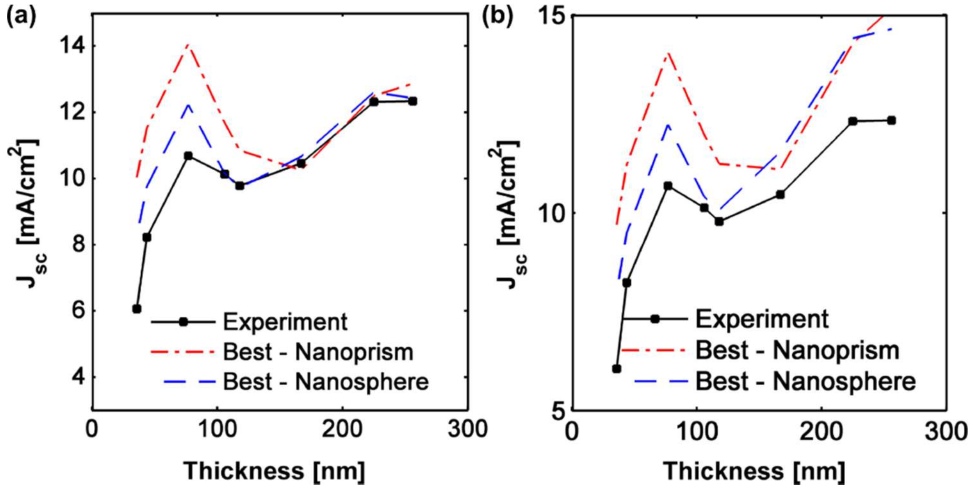

Figure C.6. Comparison of best results for different particle types. (a) Comparison of Jsc for devices without nanoparticles (experiment), silver nanoprisms and spherical silver nanoparticles (diameter = 12 nm). IQEs are taken from the linear fit in Figure 4.2(b). (b) Same comparison as in (a) using a thickness independent IQE (0.88). In both cases the active layer thickness is 77 nm.

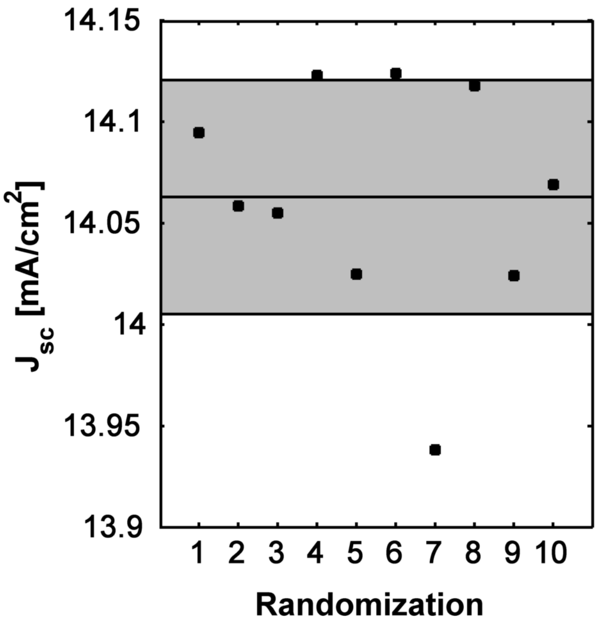

Figure C.7. J_{sc} for different randomizations. Short circuit current for different randomizations of position and orientation of nanoparticles in the active layer. The average Jsc value (center line) is 14.06 mA/cm2 with a standard deviation (gray area) of 0.06 mA/cm2, which corresponds to a variation of 0.43%.

VITA

Education

2015 Ph.D., Department of Physics, University of Washington
Advisor: David S. Ginger

2011 B.Sc., Department of Physics, Bilkent University
Advisor: Hilmi Volkan Demir

Publications

Classifying DNA Pulling Measurements Using Supervised and Unsupervised Machine Learning Methods. *Submitted to Journal of Chemical Information and Modeling.*

Fast Time-Resolved Electrostatic Force Microscopy: Achieving Sub-Cycle Time Resolution. *Submitted to Review of Scientific Instruments.*

Nanoscale Surface Potential Variation Correlates with Local S/Se Ratio in Solution-Processed CZTSSe Solar Cells. *Nano Lett. 14, 6926–30 (2014).*

Performance limits of plasmon-enhanced organic photovoltaics. *Appl. Phys. Lett. 105, 033304 (2014).*

Excitonic enhancement of nonradiative energy transfer from a quantum well in the optical near field of energy gradient quantum dots. *Appl. Phys. Lett. 100, 241109 (2012).*

Structural tuning of color chromaticity through nonradiative energy transfer by interspacing CdTe nanocrystal monolayers. *Appl. Phys. Lett. 94, 061105 (2009).*

Awards and Honors

2013 Clean Energy Institute Graduate Fellowship, University of Washington
2010 Summer Undergraduate Research Fellowship, California Institute of Technology
2009 Summer School Scholarship, Utrecht University
2006 Prime Minister’s Fellowship, Republic of Turkey
2006 Undergraduate Scholarship, Bilkent University